

¹ **Searches for Supersymmetry using the α_T
² variable with the CMS detector at the LHC**

³ Darren Burton

⁴ Imperial College London
⁵ Department of Physics

⁶ A thesis submitted to Imperial College London
⁷ for the degree of Doctor of Philosophy

9 Abstract

10 A search for supersymmetric particles is presented, using the Compact
11 Muon Solenoid detector at the Large Hadron Collider, with a signature
12 of missing energy in events with high p_T jets is presented. The analysis is
13 performed with 11.7 fb^{-1} of data, collected at a center-of-mass energy of
14 8 TeV during the 2012 run period. The dimensionless kinematic variable
15 α_T is used to select events with genuine missing energy signatures, while
16 Standard Model backgrounds in the signal region estimated using data
17 driven control samples. A complementary method to search for natural
18 SUSY signatures with a high number of b-flavoured jets, through the use
19 of a simple template fit is presented. The α_T search is used as a vehicle to
20 demonstrate proof of principle and as a search region for this technique.
21 Additionally the efficiency of the hadronic Level-1 single jet triggers are
22 measured throughout the 2012 run period. Results are presented with
23 a view to comparing L1 jet performance, before and after, a change
24 to the jet seed algorithm implemented during data taking. No excess
25 of events is found over Standard Model expectations in the α_T search.
26 Exclusion limits are set at the 95% confidence level in the parameter
27 space of simplified models, with special emphasis on compressed spectra
28 and natural SUSY scenarios.

29

Declaration

30

I, the author of this thesis, declare that the work presented within this document to be my own. The work presented in Chapters 4, 6, 5 and Section 3.4.1, is a result of the author's own work or that of which I have been a major contributor unless explicitly stated otherwise, and is carried out within the context of the Imperial College London and CERN SUSY groups, itself a subsection of the greater CMS collaboration. All figures and studies taken from external sources are referenced appropriately throughout this document.

36

Darren Burton

37

38

Acknowledgements

39 Of the many people who deserve thanks, some are particularly prominent.... Thank Rob
40 Thank Jad

41 Contents

42	List of Figures	viii
43	List of Tables	xiii
44	1. Introduction	2
45	2. A Theoretical Overview	5
46	2.1. The Standard Model	5
47	2.1.1. Gauge Symmetries of the SM	7
48	2.1.2. The Electroweak Sector and Electroweak Symmetry Breaking	9
49	2.2. Motivation for Physics Beyond the Standard Model	13
50	2.3. Supersymmetry Overview	14
51	2.3.1. R-Parity	16
52	2.4. Experimental Signatures of SUSY at the LHC	16
53	2.4.1. Simplified models	18
54	3. The LHC And The CMS Detector	20
55	3.1. The LHC	20
56	3.2. The CMS Detector	23
57	3.2.1. Detector subsystems	23
58	3.2.2. Tracker	24
59	3.2.3. Electromagnetic calorimeter	25
60	3.2.4. Hadronic calorimeter	26
61	3.2.5. Muon systems	28
62	3.3. Event Reconstruction and Object Definition	28
63	3.3.1. Jets	28
64	3.3.2. B-tagging	30
65	3.4. Triggering System	33
66	3.4.1. The level-1 trigger	34

67	3.4.2. The L1 trigger jet algorithm	35
68	3.4.3. Measuring L1 jet trigger efficiencies	37
69	3.4.4. Effects of the L1 jet seed	38
70	3.4.5. Robustness of L1 jet performance against pile-up	40
71	3.4.6. Summary	43
72	4. SUSY Searches In Hadronic Final States	45
73	4.1. An Introduction to the α_T Search	46
74	4.1.1. The α_T variable	48
75	4.2. Search Strategy	50
76	4.2.1. Physics objects	53
77	4.2.2. Event selection	55
78	4.2.3. Control sample definition and background estimation	57
79	4.2.4. Estimating the QCD multi-jet background	64
80	4.3. Trigger Strategy	66
81	4.4. Measuring MC Normalisation Factors via H_T Sidebands	67
82	4.5. Determining MC Simulation Yields with Higher Statistical Precision	68
83	4.5.1. The formula method	69
84	4.5.2. Establishing proof of principle	70
85	4.5.3. Correcting measured efficiencies in simulation to data	70
86	4.6. Systematic Uncertainties on Transfer Factors	73
87	4.6.1. Determining systematic uncertainties from closure tests	77
88	4.7. Simplified Models, Efficiencies and Systematic Uncertainties	79
89	4.7.1. Signal efficiency	80
90	4.7.2. Applying b-tag scale factor corrections in signal samples	81
91	4.7.3. Experimental uncertainties	82
92	4.8. Statistical Framework	85
93	4.8.1. Hadronic sample	85
94	4.8.2. H_T evolution model	86
95	4.8.3. Electroweak Sector (EWK) control samples	86
96	4.8.4. Contributions from signal	89
97	4.8.5. Total likelihood	90
98	5. Results and Interpretation	91
99	5.1. Standard Model	91
100	5.2. SUSY	100
101	5.2.1. The CL_s method	100

102	5.2.2. Interpretation in simplified signal models	101
103	6. Searches For Natural SUSY With B-tag Templates.	105
104	6.1. Concept	105
105	6.2. Application to the α_T Search	107
106	6.2.1. Proof of principle in simulation	108
107	6.2.2. Results in a data control sample	111
108	6.2.3. Application to the α_T hadronic search region	113
109	6.3. Summary	113
110	7. Conclusions	114
111	A. Miscellaneous	116
112	A.1. Noise Filters	116
113	A.2. Primary Vertices	118
114	B. L1 Jets	120
115	B.1. Jet matching efficiencies	120
116	B.2. Leading Jet Energy Resolution	121
117	B.3. Resolution for Energy Sum Quantities	124
118	C. Additional material on background estimation methods	129
119	C.1. Determination of k_{QCD}	129
120	C.2. Effect of varying background cross sections on closure tests	130
121	D. Additional Material For B-tag Template Method	131
122	D.1. Templates Fits in Simulation	131
123	D.2. Pull Distributions for Template Fits	134
124	D.3. Templates Fits in Data	134
125	Bibliography	137

¹²⁶ List of Figures

¹²⁷ 2.1.	One loop quantum corrections to the Higgs squared mass parameter m_h^2 due to a fermion.	14
¹²⁹ 2.2.	Two example simplified model decay chains.	19
¹³⁰ 3.1.	A top down layout of the LHC, with the position of the four main detectors labelled.	21
¹³² 3.2.	The total integrated luminosity delivered to and collected by Compact Muon Solenoid (CMS) during the 2012 8 TeV pp runs	22
¹³⁴ 3.3.	A pictorial depiction of the CMS detector.	24
¹³⁵ 3.4.	Illustration of the CMS Electromagnetic CALorimeter (ECAL).	26
¹³⁶ 3.5.	Schematic of the CMS Hadronic CALorimeter (HCAL).	27
¹³⁷ 3.6.	Combined Secondary Vertex (CSV) algorithm discriminator values in enriched ttbar and inclusive multi jet samples	31
¹³⁹ 3.7.	Data/MC b-tag scale factors derived using the Combined Secondary Vertex Medium Working Point (CSVM) tagger.	32
¹⁴¹ 3.8.	Data/MC mis-tag scale factors derived using the CSVM tagger.	33
¹⁴² 3.9.	The CMS Level 1 Trigger (L1) Trigger system.	34
¹⁴³ 3.10.	Illustration of the Level-1 jet finding algorithm.	36
¹⁴⁴ 3.11.	L1 jet efficiency turn-on curves as a function of the offline CaloJet and PFJet E_T	38
¹⁴⁶ 3.12.	L1 jet efficiency turn-on curves as a function of the offline CaloJet E_T for the 2012 run period B and C.	39

148	3.13. Trigger cross section for the L1HTT150 trigger path.	40
149	3.14. L1 H_T efficiency turn-on curves as a function of the offline CaloJet H_T	41
150	3.15. L1 jet efficiency turn-on curves as a function of the leading offline E_T Calo	
151	(left) and PF (right) jet, for low, medium and high pile-up conditions.	42
152	3.16. Fit values from an Exponentially Modified Gaussian (EMG) function fitted	
153	to the resolution plots of leading Calo jet E_T measured as a function of	
154	$\frac{(L1\ E_T - \text{Offline}\ E_T)}{\text{Offline}\ E_T}$ for low, medium and high pile-up conditions.	43
155	3.17. Fit values from an EMG function fitted to the resolution plots of leading	
156	PF jet E_T measured as a function of $\frac{(L1\ E_T - \text{Offline}\ E_T)}{\text{Offline}\ E_T}$ for low, medium and	
157	high pile-up conditions.	44
158	4.1. Reconstructed offline H_T for 11.7fb^{-1} of data after a basic pre-selection.	47
159	4.2. The event topologies of background QCD dijet events (right) and a generic	
160	SUSY signature with genuine Z_T (left).	48
161	4.3. The α_T distributions for the low 2-3 (left) and high ≥ 4 (right) jet	
162	multiplicities after a full analysis selection and shown for $H_T > 375$	50
163	4.4. Pictorial depiction of the analysis strategy employed by the α_T search to	
164	increase sensitivity to a wide spectra of SUSY models.	52
165	4.5. Data/MC comparisons of key variables for the hadronic signal region.	57
166	4.6. Data/MC comparisons of key variables for the $\mu + \text{jets}$ selection.	60
167	4.7. Data/MC comparisons of key variables for the $\mu\mu + \text{jets}$ selection.	62
168	4.8. Data/MC comparisons of key variables for the $\gamma + \text{jets}$ selection.	63
169	4.9. QCD sideband regions, used for determination of k_{QCD}	65
170	4.10. placeholder.	72
171	4.11. Sets of closure tests overlaid on top of the systematic uncertainty used for	
172	each of the five H_T regions.	78
173	4.12. Signal efficiencies for the Simplified Model Spectra (SMS) models (a) T1	
174	and (b) T2.	80

175	5.1. Comparison of the observed yields and Standard Model (SM) expectations given by the simultaneous fit in bins of H_T for the (a) hadronic, (b) $\mu +$ jets, (c) $\mu\mu +$ jets and (d) $\gamma +$ jets samples when requiring $n_b^{reco} = 0$ and $n_{jet} \leq 3$	93
179	5.2. Comparison of the observed yields and SM expectations given by the simultaneous fit in bins of H_T for the (a) hadronic, (b) $\mu +$ jets, (c) $\mu\mu +$ jets and (d) $\gamma +$ jets samples when requiring $n_b^{reco} = 1$ and $n_{jet} \leq 3$	94
182	5.3. Comparison of the observed yields and SM expectations given by the simultaneous fit in bins of H_T for the (a) hadronic, (b) $\mu +$ jets, (c) $\mu\mu +$ jets and (d) $\gamma +$ jets samples when requiring $n_b^{reco} = 2$ and $n_{jet} \leq 3$	95
185	5.4. Comparison of the observed yields and SM expectations given by the simultaneous fit in bins of H_T for the (a) hadronic, (b) $\mu +$ jets, (c) $\mu\mu +$ jets and (d) $\gamma +$ jets samples when requiring $n_b^{reco} = 0$ and $n_{jet} \geq 4$	96
188	5.5. Comparison of the observed yields and SM expectations given by the simultaneous fit in bins of H_T for the (a) hadronic, (b) $\mu +$ jets, (c) $\mu\mu +$ jets and (d) $\gamma +$ jets samples when requiring $n_b^{reco} = 1$ and $n_{jet} \geq 4$	97
191	5.6. Comparison of the observed yields and SM expectations given by the simultaneous fit in bins of H_T for the (a) hadronic, (b) $\mu +$ jets, (c) $\mu\mu +$ jets and (d) $\gamma +$ jets samples when requiring $n_b^{reco} = 2$ and $n_{jet} \geq 4$	98
194	5.7. Comparison of the observed yields and SM expectations given by the simultaneous fit in bins of H_T for the (a) hadronic, (b) $\mu +$ jets, (c) $\mu\mu +$ jets and (d) $\gamma +$ jets samples when requiring $n_b^{reco} = 3$ and $n_{jet} \geq 4$	98
197	5.8. Comparison of the observed yields and SM expectations given by the simultaneous fit in bins of H_T for the (a) hadronic, (b) $\mu +$ jets, (c) $\mu\mu +$ jets and (d) $\gamma +$ jets samples when requiring $n_b^{reco} \geq 4$ and $n_{jet} \geq 4$	99
200	5.9. Production and decay modes for the various SMS models interpreted within the analysis.	103
202	5.10. Upper limit of cross section at 95% CL as a function of $m_{\tilde{q}/\tilde{g}}$ and m_{LSP} for various SMS models.	104

204	6.1. The b-tagging (a), c-quark mis-tagging (b), and light-quark mis-tagging 205 rate (c) as measured in simulation after the α_T analysis, $\mu + \text{jets}$ control 206 sample selection in the region $H_T > 375$	107
207	6.2. The results of fitting the $Z = 0$ and $Z = 2$ templates to the $n_b^{reco} = 0, 1, 2$ 208 bins taken directly from simulation in the region $H_T > 375$ GeV, for the 209 $n_{jet} \geq 5$ category.	110
210	6.3. The results of fitting the $Z = 0$ and $Z = 2$ templates to the $n_b^{reco} = 0, 1, 2$ 211 bins taken from data, for the $n_{jet} \geq 5$ category and medium CSV working 212 point.	112
213	B.1. Leading jet matching efficiency as a function of the offline CaloJet E_T	120
214	B.2. Resolution plots of the leading offline Calo E_T measured as a function of 215 $\frac{(L1 E_T - \text{Offline } E_T)}{\text{Offline } E_T}$ for low (a), medium (b) and high (c) pile-up conditions.	122
216	B.3. Resolution plots of the leading off-line PF E_T measured as a function of 217 $\frac{(L1 E_T - \text{Offline } E_T)}{\text{Offline } E_T}$ for low (a), medium (b) and high (c) pile-up conditions.	124
218	B.4. $\sum E_T$ resolution parameters in bins of Calo $\sum E_T$ measured for the 219 defined low, medium and high pile up conditions.	125
220	B.5. $\sum E_T$ resolution parameters in bins of PF $\sum E_T$ measured for the defined 221 low, medium and high pile up conditions.	125
222	B.6. \cancel{E}_T resolution parameters in bins of Calo \cancel{E}_T measured for the defined 223 low, medium and high pile up conditions.	126
224	B.7. \cancel{E}_T resolution parameters in bins of PF \cancel{E}_T measured for the defined low, 225 medium and high pile up conditions.	126
226	B.8. H_T resolution parameters in bins of Calo H_T measured for the defined 227 low, medium and high pile up conditions.	127
228	B.9. H_T resolution parameters in bins of PF H_T measured for the defined low, 229 medium and high pile up conditions.	127
230	B.10. \cancel{H}_T resolution parameters in bins of \cancel{H}_T measured for the defined low, 231 medium and high pile up conditions.	128

232	B.11. \mathcal{H}_T resolution parameters in bins of PF \mathcal{H}_T measured for the defined low,	
233	medium and high pile up conditions.	128
234	C.1. $R_{\alpha_T}(H_T)$ and exponential fits for each of the data sideband regions. Fit is	
235	conducted between the H_T region $275 < H_T < 575$	129
236	C.2. Sets of closure tests overlaid on top of the systematic uncertainty used for	
237	each of the five H_T regions.	130
238	C.3. Sets of closure tests overlaid on top of the systematic uncertainty used for	
239	each of the five H_T regions.	130
240	D.1. The results of fitting the $Z = 0$ and $Z = 2$ templates to the $n_b^{reco} = 0, 1, 2$	
241	bins taken directly from simulation in the region $H_T > 375$ GeV, for the	
242	$n_{jet} = 3$ category.	132
243	D.2. The results of fitting the $Z = 0$ and $Z = 2$ templates to the $n_b^{reco} = 0, 1, 2$	
244	bins taken directly from simulation in the region $H_T > 375$ GeV, for the	
245	$n_{jet} = 4$ category.	133
246	D.3. The results of fitting the $Z = 0$ and $Z = 2$ templates to the $n_b^{reco} = 0, 1,$	
247	2 bins taken directly from data, for the $n_{jet} \geq 5$ category and loose CSV	
248	working point.	134
249	D.4. The results of fitting the $Z = 0$ and $Z = 2$ templates to the $n_b^{reco} = 0, 1,$	
250	2 bins taken directly from data, for the $n_{jet} \geq 5$ category and tight CSV	
251	working point.	135

²⁵² List of Tables

²⁵³	2.1. The fundamental particles of the SM, with spin, charge and mass displayed.	6
²⁵⁴	3.1. Results of a cumulative EMG function fit to the turn-on curves for L1	
²⁵⁵	single jet triggers in 2012 Run Period C.	38
²⁵⁶	3.2. Results of a cumulative EMG function fit to the turn-on curves for L1	
²⁵⁷	single jet triggers in the 2012 run period B and C.	40
²⁵⁸	3.3. Results of a cumulative EMG function fit to the turn-on curves for H_T in	
²⁵⁹	2012 run period B and C.	41
²⁶⁰	3.4. Results of a cumulative EMG function fit to the efficiency turn-on curves	
²⁶¹	for L1 single jet triggers in the 2012 run period C, for low,medium and	
²⁶²	high pile-up conditions.	41
²⁶³	3.5. Results of a cumulative EMG function fit to the efficiency turn-on curves	
²⁶⁴	for Level-1 single jet triggers in the 2012 run period C, for low,medium	
²⁶⁵	and high pile-up conditions.	42
²⁶⁶	4.1. A summary of the SMS models interpreted in this analysis, involving both	
²⁶⁷	direct (D) and gluino-induced (G) production of squarks and their decays.	46
²⁶⁸	4.2. Muon Identification criteria used within the analysis for selection/veto	
²⁶⁹	purposes in the muon control/signal selections.	53
²⁷⁰	4.3. Photon Identification criteria used within the analysis for selection/veto	
²⁷¹	purposes in the $\gamma +$ jets control/signal selections.	54
²⁷²	4.4. Electron Identification criteria used within the analysis for veto purposes.	54
²⁷³	4.5. Jet thresholds used in the three H_T regions of the analysis.	55

274	4.6. Best fit values for the parameters k_{QCD} obtained from sideband regions B,C ₁ ,C ₂ ,C ₃	66
275		
276	4.7. Measured efficiencies of the H_T and α_T legs of the HT and HT_alphaT triggers in independent analysis bins.	67
277		
278	4.8. k-factors calculated for different EWK processes.	68
279		
280	4.9. Comparing yields in simulation within the $\mu +$ jets selection determined from the formula method described in Equation (4.11), and that taken directly from simulation	71
281		
282	4.10. The absolute change in the Transfer Factor (TF)'s used to predict the entire signal region SM background, using the $\mu +$ jets control sample when the systematic uncertainties of the data to simulation scale factors are varied by $\pm 1\sigma$	73
283		
284		
285		
286	4.11. A summary of the results obtained from fits of zeroeth order polynomials (i.e. a constant) to five sets of closure tests performed in the $2 \leq n_{jet} \leq 3$ bin	76
287		
288		
289	4.12. A summary of the results obtained from fits of zeroeth order polynomials (i.e. a constant) to five sets of closure tests performed in the $n_{jet} \geq 4$ bin	76
290		
291	4.13. A summary of the results obtained from fits of zeroeth order polynomials (i.e. a constant) to five sets of closure tests performed in the $2 \leq n_{jet} \leq 3$ bin	76
292		
293		
294	4.14. Calculated systematic uncertainties for the five H_T regions, determined from the closure tests.	77
295		
296	4.15. Estimates of systematic uncertainties on the signal efficiency (%) for various SMS models when considering points in the region near to the diagona	84
297		
298		
299	4.16. Estimates of systematic uncertainties on the signal efficiency (%) for various SMS models when considering points in the region near to the diagona	84
300		
301		
302	4.17. The systematic parameters used in H_T bins.	88

303	4.18. Nuisance parameters used within the different hadronic signal bins of the analysis	90
305	5.1. Summary of control samples used by each fit results, and the Figures in which they are displayed.	92
307	5.2. Comparison of the measured yields in the each H_T , n_{jet} and n_b^{reco} jet multiplicity bins for the hadronic sample with the SM expectations and combined statistical and systematic uncertainties given by the simultaneous fit.	92
311	5.3. A table representing the SMS models interpreted within the analysis.	101
312	6.1. Summary of the fit predictions in the n_b^{reco} signal region for $n_{jet} = 3, = 4, \geq 5$. The fit region is $n_b^{reco} = 0, 1, 2$ and simulation yields are normalised to an integrated luminosity of 10 fb^{-1}	109
315	6.2. Summary of the fit predictions in the n_b^{reco} signal region of the $\mu + \text{jets}$ control sample, for $n_{jet} = 3, = 4, \geq 5$. The fit region is $n_b^{reco} = 0, 1, 2$ using 11.5 fb^{-1} of data at $\sqrt{s} = 8\text{TeV}$	111
318	A.1. Criteria for a reconstructed jet to pass the loose calorimeter jet id.	116
319	A.2. Criteria for a reconstructed jet to pass the loose PF jet id.	117
320	A.3. Noise filters that are applied to remove spurious and non-physical E_T signatures within the CMS detector.	118
322	A.4. Criteria for a vertex in an event to be classified as a 'good' reconstructed primary vertex.	119
324	B.1. Results of a cumulative EMG function fit to the turn-on curves for the matching efficiency of the leading jet in an event to a Level-1 jet in run 2012C and 2012B data.	121
327	C.1.	130

328 Acronyms

329	ALICE	A Large Ion Collider Experiment
330	ATLAS	A Toroidal LHC ApparatuS
331	APD	Avalanche Photo-Diodes
332	BSM	Beyond Standard Model
333	CERN	European Organization for Nuclear Research
334	CMS	Compact Muon Solenoid
335	CMSSM	Compressed Minimal SuperSymmetric Model
336	CSC	Cathode Stripe Chamber
337	CSV	Combined Secondary Vertex
338	CSVM	Combined Secondary Vertex Medium Working Point
339	DT	Drift Tube
340	ECAL	Electromagnetic CALorimeter
341	EB	Electromagnetic CALorimeter Barrel
342	EE	Electromagnetic CALorimeter Endcap
343	ES	Electromagnetic CALorimeter pre-Shower
344	EMG	Exponentially Modified Gaussian
345	EPJC	European Physical Journal C
346	EWK	Electroweak Sector
347	GCT	Global Calorimeter Trigger
348	GMT	Global MuonTrigger
349	GT	Global Trigger
350	HB	Hadron Barrel
351	HCAL	Hadronic CALorimeter

352	HE	Hadron Endcaps
353	HF	Hadron Forward
354	HLT	Higher Level Trigger
355	HO	Hadron Outer
356	HPD	Hybrid Photo Diode
357	ISR	Initial State Radiation
358	LUT	Look Up Table
359	L1	Level 1 Trigger
360	LHC	Large Hadron Collider
361	LHCb	Large Hadron Collider Beauty
362	LSP	Lightest Supersymmetric Partner
363	NLL	Next to Leading Logarithmic Order
364	NLO	Next to Leading Order
365	NNLO	Next to Next Leading Order
366	POGs	Physics Object Groups
367	PS	Proton Synchrotron
368	QED	Quantum Electro-Dynamics
369	QCD	Quantum Chromo-Dynamics
370	QFT	Quantum Field Theory
371	RBXs	Readout Boxes
372	RPC	Resistive Plate Chamber
373	RCT	Regional Calorimeter Trigger
374	RMT	Regional Muon Trigger
375	SUSY	SUperSYmmetry
376	SM	Standard Model

³⁷⁷	SMS	Simplified Model Spectra
³⁷⁸	SPS	Super Proton Synchrotron
³⁷⁹	TF	Transfer Factor
³⁸⁰	TP	Trigger Primitive
³⁸¹	VEV	Vacuum Expectation Value
³⁸²	VPT	Vacuum Photo-Triodes
³⁸³	WIMP	Weakly Interacting Massive Particle

³⁸⁴

“The Universe is about 1,000,000 years old.”

— Matthew Kenzie, 1987-present : Discoverer of the Higgs Boson.

³⁸⁵

Chapter 1.

³⁸⁶ Introduction

³⁸⁷ During the 20th century great advances have been made in the human understanding
³⁸⁸ of the universe, it's origins, it's future and its composition. The Standard Model (**SM**)
³⁸⁹ first formulated in the 1960's is one of the crowning achievements in science's quest to
³⁹⁰ explain the most fundamental processes and interactions that make up our universe. It
³⁹¹ has provided a highly successful explanation of a wide range of phenomena in Particle
³⁹² Physics and has stood up to extensive experimental scrutiny [1].

³⁹³ Despite it's successes it is not a complete theory, with significant questions remaining
³⁹⁴ unanswered. It describes only three of the four known forces with gravity not incorpo-
³⁹⁵ rated within the framework of the **SM**. Cosmological experiments infer that just $\sim 4\%$
³⁹⁶ of the observable universe exists as matter, with elusive "Dark Matter" accounting for a
³⁹⁷ further $\sim 23\%$ [2]. However no particle predicted by the **SM** is able to account for it. At
³⁹⁸ higher energy scales and small distances the (non-)unification of the fundamental forces
³⁹⁹ point to problems with the **SM** at least at higher energies not yet probed experimentally.

⁴⁰⁰ Many theories exist as extensions to the **SM**, which predict a range of observables that
⁴⁰¹ can be detected at the Large Hadron Collider (**LHC**) of which SUperSYmmetry (**SUSY**)
⁴⁰² is one such example. It predicts a new symmetry of nature in which all current particles
⁴⁰³ in the **SM** would have a corresponding supersymmetric partner. Common to most
⁴⁰⁴ Supersymmetric theories is a stable, weakly interacting Lightest Supersymmetric Partner
⁴⁰⁵ (**LSP**), which has the properties of a possible dark matter candidate. The **SM** and the
⁴⁰⁶ main principles of Supersymmetric theories are outlined in Chapter 2, with emphasis
⁴⁰⁷ placed on how experimental signatures of **SUSY** may reveal themselves at the **LHC**.

⁴⁰⁸ The experimental goal of the **LHC** is to further test the framework of the **SM**, exploring the
⁴⁰⁹ TeV mass scale for the first time, and to seek a connection between the particles produced

410 in proton collisions and dark matter. The first new discovery by this extraordinary
411 machine was announced on the 4th of July 2012. The long-awaited discovery was the
412 culmination decades of experimental endeavours in the search for the Higgs boson,
413 providing an answer to the mechanism of electroweak symmetry breaking within the **SM**
414 [3][4].

415 This discovery was made possible through data taken by the two multi purpose detectors
416 (**CMS** and A Toroidal LHC ApparatuS (**ATLAS**)) located on the **LHC** ring. An experi-
417 mental description of the **CMS** detector and the **LHC** is described in Chapter 3, including
418 some of the object reconstruction used by **CMS** in searches for **SUSY** signatures. The
419 performance of the **CMS** Level-1 calorimeter trigger, benchmarked by the author is also
420 included within this chapter.

421 The analysis conducted by the author is detailed within Chapter 4. This chapter contains
422 a description of the search for evidence of the production of Supersymmetric particles
423 at the **LHC**. The main basis of the search centres around the kinematic dimensionless
424 α_T variable, which provides strong rejection of backgrounds with fake missing energy
425 signatures whilst maintaining good sensitivity to a variety of **SUSY** topologies. The
426 author's work (as an integral part of the analysis group) is documented in detail, which
427 has culminated in numerous publications over the past two years. The latest of which
428 was published in the European Physical Journal C (**EPJC**) [5] and contains the results
429 which are discussed within this and the sequential Chapters.

430 The author in particular has played a major role in the extension of the α_T analysis into
431 the additional b-tagged and jet multiplicity dimensions increasing the sensitivity of the
432 analysis to a range of **SUSY** topologies. Additionally the author has worked extensively
433 in both increasing the statistical precision of electroweak predictions measured from
434 simulation through analytical techniques, and the derivation of a data driven systematic
435 uncertainty through the establishment of closure tests within the control samples of the
436 analysis.

437 Additionally a method to search for **SUSY** signatures which are rich in top and bottom
438 flavoured jet final states is discussed in Chapter 6. A parametrisation of the b-tagging
439 distribution for different Electroweak processes is used to establish templates, which
440 are then used to estimate the expected number of 3 or 4 b-tagged jet events from **SM**
441 processes. The α_T search is used as a cross check for this template method to establish
442 it's functionality.

⁴⁴³ Finally the interpretation of such results within the framework of a variety of Simplified
⁴⁴⁴ Model Spectra (**SMS**), which describe an array of possible **SUSY** event topologies is
⁴⁴⁵ documented in Chapter 5. A description of the statistical model used to derive these
⁴⁴⁶ interpretations and the possible implications of the results presented in this thesis is
⁴⁴⁷ discussed within this Chapter. Natural units are used throughout this thesis in which \hbar
⁴⁴⁸ $= c = 1$.

Chapter 2.

⁴⁴⁹ A Theoretical Overview

⁴⁵⁰ Within this chapter, a brief introduction and background to the **SM** is given. Its success
⁴⁵¹ as a rigorously tested and widely accepted theory is discussed as are its deficiencies,
⁴⁵² leading to the argument that this theory is not a complete description of our universe.
⁴⁵³ The motivations for new physics at the TeV scale and in particular Supersymmetric
⁴⁵⁴ theories are outlined within Section (2.3), with the chapter concluding with how an
⁴⁵⁵ experimental signature of such theories can be produced and observed at the **LHC**,
⁴⁵⁶ Section (2.4).

⁴⁵⁷ 2.1. The Standard Model

⁴⁵⁸ The **SM** is the name given to the relativistic Quantum Field Theory (**QFT**), where
⁴⁵⁹ particles are represented as excitations of fields, which describe the interactions and
⁴⁶⁰ properties of all the known elementary particles [6][7][8][9]. It is a renormalisable field
⁴⁶¹ theory which contains three symmetries: $SU(3)$ for colour charge, $SU(2)$ for weak isospin
⁴⁶² and $U(1)$ relating to weak hyper charge, which require its Lagrangian \mathcal{L}_{SM} to be invariant
⁴⁶³ under local gauge transformation.

⁴⁶⁴ Within the **SM** theory, matter is composed of spin $\frac{1}{2}$ fermions, which interact with each
⁴⁶⁵ other via the exchange of spin-1 gauge bosons. A summary of the known fundamental
⁴⁶⁶ fermions and bosons is given in Table 2.1.

⁴⁶⁷ Fermions are separated into quarks and leptons of which only quarks interact with the
⁴⁶⁸ strong nuclear force. Quarks unlike leptons are not seen as free particles in nature, but
⁴⁶⁹ rather exist only within baryons, composed of three quarks with an overall integer charge,
⁴⁷⁰ and quark-anti-quark pairs called mesons. Both leptons and quarks are grouped into

Particle	Symbol	Spin	Charge	Mass (GeV)
First Generation Fermions				
Electron Neutrino	ν_e	$\frac{1}{2}$	0	$< 2.2 \times 10^{-6}$
Electron	e	$\frac{1}{2}$	-1	0.51×10^{-3}
Up Quark	u	$\frac{1}{2}$	$\frac{2}{3}$	$2.3^{+0.7}_{-0.5} \times 10^{-3}$
Down Quark	d	$\frac{1}{2}$	$-\frac{1}{3}$	$4.8^{+0.7}_{-0.3} \times 10^{-3}$
Second Generation Fermions				
Muon Neutrino	ν_μ	$\frac{1}{2}$	0	-
Muon	μ	$\frac{1}{2}$	-1	1.05×10^{-3}
Charm Quark	c	$\frac{1}{2}$	$\frac{2}{3}$	1.275 ± 0.025
Strange Quark	s	$\frac{1}{2}$	$-\frac{1}{3}$	$95 \pm 5 \times 10^{-3}$
Third Generation Fermions				
Tau Neutrino	ν_τ	$\frac{1}{2}$	0	-
Tau	τ	$\frac{1}{2}$	-1	1.77
Top Quark	t	$\frac{1}{2}$	$\frac{2}{3}$	173.5 ± 0.8
Bottom Quark	b	$\frac{1}{2}$	$-\frac{1}{3}$	4.65 ± 0.03
Gauge Bosons				
Photon	γ	1	0	0
W Boson	W^\pm	1	± 1	80.385 ± 0.015
Z Boson	Z	1	0	91.187 ± 0.002
Gluons	g	1	0	0
Higgs Boson	H	0	0	125.3 ± 0.5 [4]

Table 2.1.: The fundamental particles of the SM, with spin, charge and mass displayed. Latest mass measurements taken from [1].

⁴⁷¹ three generations which have the same properties, but with ascending mass in each
⁴⁷² subsequent generation.

⁴⁷³ The gauge bosons mediate the interactions between fermions. The field theories of
⁴⁷⁴ Quantum Electro-Dynamics (QED) and Quantum Chromo-Dynamics (QCD), yield
⁴⁷⁵ massless mediator bosons, the photon and eight coloured gluons which are consequences
⁴⁷⁶ of the gauge invariance of those theories, detailed in Section (2.1.1).

⁴⁷⁷ The unification of the electromagnetic and weak-nuclear forces into the current Elec-
⁴⁷⁸ troweak theory yield the weak gauge bosons, W^\pm and Z through the mixing of the
⁴⁷⁹ associated gauge fields. The force carriers of this theory were experimentally detected by
⁴⁸⁰ the observation of weak neutral current, discovered in 1973 in the Gargamelle bubble
⁴⁸¹ chamber located at European Organization for Nuclear Research (CERN) [10], with the
⁴⁸² masses of the weak gauge bosons measured by the UA1 and U2 experiments at the Super
⁴⁸³ Proton Synchrotron (SPS) collider in 1983 [11][12].

⁴⁸⁴ 2.1.1. Gauge Symmetries of the SM

⁴⁸⁵ Symmetries are of fundamental importance in the description of physical phenomena.
⁴⁸⁶ Noether's theorem states that for a dynamical system, the consequence of any symmetry
⁴⁸⁷ is an associated conserved quantity [13]. Invariance under translations, rotations, and
⁴⁸⁸ Lorentz transformations in physical systems lead to conservation of momentum, energy
⁴⁸⁹ and angular momentum.

⁴⁹⁰ In the **SM**, a quantum theory described by Lagrangian formalism, the weak, strong and
⁴⁹¹ electromagnetic interactions are described in terms of “gauge theories”. A gauge theory
⁴⁹² possesses invariance under a set of “local transformations”, which are transformations
⁴⁹³ whose parameters are space-time dependent. The requirement of gauge invariance within
⁴⁹⁴ the **SM** necessitates the introduction of force-mediating gauge bosons and interactions
⁴⁹⁵ between fermions and the bosons themselves. Given the nature of the topics covered by
⁴⁹⁶ this thesis, the formulation of **EWK** within the **SM** Lagrangian is reviewed within this
⁴⁹⁷ section.

⁴⁹⁸ The simplest example of the application of the principle of local gauge invariance within
⁴⁹⁹ the **SM** is in Quantum Electro-Dynamics (**QED**), the consequences of which require a
⁵⁰⁰ massless photon field [14][15].

⁵⁰¹ Starting from the free Dirac Lagrangian written as

$$\mathcal{L} = \bar{\psi}(i\gamma^\mu \partial_\mu - m)\psi, \quad (2.1)$$

⁵⁰² where ψ represents a free non interacting fermionic field, with the matrices $\gamma^\mu, \mu \in 0, 1, 2, 3$
⁵⁰³ defined by the anti commutator relationship $\gamma^\mu \gamma^\nu + \gamma^\nu \gamma^\mu = 2\eta^{\mu\nu} I_4$, with $\eta^{\mu\nu}$ being the
⁵⁰⁴ flat space-time metric $(+, -, -, -)$ and I_4 the 4×4 identity matrix.

⁵⁰⁵ Under a local U(1) abelian gauge transformation in which ψ transforms as:

$$\psi(x) \rightarrow \psi'(x) = e^{i\theta(x)}\psi(x) \quad \bar{\psi}(x) \rightarrow \bar{\psi}'(x) = e^{i\theta(x)}\bar{\psi}(x) \quad (2.2)$$

⁵⁰⁶ the kinetic term of the Lagrangian does not remain invariant, due to the partial derivative
⁵⁰⁷ interposed between the $\bar{\psi}$ and ψ yielding,

$$\partial_\mu \psi \rightarrow e^{i\theta(x)} \partial_\mu \psi + ie^{i\theta(x)} \psi \partial_\mu \theta. \quad (2.3)$$

To ensure that \mathcal{L} remains invariant, a modified derivative, D_μ , that transforms covariantly under phase transformations is introduced. In doing this a vector field A_μ with transformation properties that cancel out the unwanted term in (2.3) must also be included,

$$D_\mu \equiv \partial_\mu - ieA_\mu, \quad A_\mu \rightarrow A_\mu + \frac{1}{e} \partial_\mu \theta. \quad (2.4)$$

Invariance of the Lagrangian is then achieved by replacing ∂_μ by D_μ :

$$\begin{aligned} \mathcal{L} &= i\bar{\psi}\gamma^\mu D_\mu \psi - m\bar{\psi}\psi \\ &= \bar{\psi}(i\gamma^\mu \partial_\mu - m)\psi + e\bar{\psi}\gamma^\mu \psi A_\mu \end{aligned} \quad (2.5)$$

An additional interaction term is now present in the Lagrangian, coupling the Dirac particle to this vector field, which is interpreted as the photon in QED. To regard this new field as the physical photon field, a term corresponding to its kinetic energy must be added to the Lagrangian from Equation (2.5). Since this term must also be invariant under the conditions of Equation (2.4), it is defined in the form $F_{\mu\nu} = \partial^\mu A^\nu - \partial^\nu A^\mu$.

This then leads to the Lagrangian of QED:

$$\mathcal{L}_{QED} = \underbrace{i\bar{\psi}\gamma^\mu \partial_\mu \psi - \frac{1}{4}F_{\mu\nu}F^{\mu\nu}}_{\text{kinetic term}} + \underbrace{m\bar{\psi}\psi}_{\text{mass term}} + \underbrace{e\bar{\psi}\gamma^\mu \psi A_\mu}_{\text{interaction term}} \quad (2.6)$$

Within the Lagrangian there remains no mass term of the form $m^2 A_\mu A^\mu$, which is prohibited by gauge invariance. This implies that the gauge particle, the photon, must be massless.

522 2.1.2. The Electroweak Sector and Electroweak Symmetry 523 Breaking

- 524 The same application of gauge symmetry and the requirement of local gauge invariance
525 can be used to unify QED and the Weak force in the Electroweak Sector (EWK).
526 The nature of EWK interactions is encompassed within a Lagrangian invariant under
527 transformations of the group $SU(2)_L \times U(1)_Y$.
528 The weak interactions from experimental observation [16], are known to violate parity
529 and are therefore not symmetric under interchange of left and right helicity fermions.
530 Thus within the SM the left and right handed parts of these fermion fields are treated
531 separately. A fermion field is then split into two left and right handed chiral components,
532 $\psi = \psi_L + \psi_R$, where $\psi_{L/R} = (1 \pm \gamma^5)\psi$.
533 The $SU(2)_L$ group is the special unitary group of 2×2 matrices U satisfying $UU^\dagger = I$
534 and $\det(U) = 1$. It may be written in the form $U = e^{-i\omega_i T_i}$, with the generators of the
535 group $T_i = \frac{1}{2}\tau_i$ where τ_i , $i \in 1,2,3$ being the 2×2 Pauli matrices

$$\tau_1 = \begin{pmatrix} 0 & 1 \\ 1 & 0 \end{pmatrix} \quad \tau_2 = \begin{pmatrix} 0 & -i \\ i & 0 \end{pmatrix} \quad \tau_3 = \begin{pmatrix} 1 & 0 \\ 0 & -1 \end{pmatrix}, \quad (2.7)$$

- 536 which form a non Abelian group obeying the commutation relation $[T^a, T^b] \equiv if^{abc}T^c \neq 0$.
537 The gauge fields that accompany this group are represented by $\hat{W}_\mu = (\hat{W}_\mu^1, \hat{W}_\mu^2, \hat{W}_\mu^3)$
538 and act only on the left handed component of the fermion field ψ_L .
539 One additional generator Y which represents the hypercharge of the particle under
540 consideration is introduced through the $U(1)_Y$ group acting on both components of the
541 fermion field, with an associated vector boson field \hat{B}_μ .
542 The $SU(2)_L \times U(1)_Y$ transformations of the left and right handed components of ψ are
543 summarised by,

$$\begin{aligned} \chi_L &\rightarrow \chi'_L = e^{i\theta(x) \cdot T + i\theta(x)Y} \chi_L, \\ \psi_R &\rightarrow \psi'_R = e^{i\theta(x)Y} \psi_R, \end{aligned} \quad (2.8)$$

⁵⁴⁴ where the left handed fermions form isospin doubles χ_L and the right handed fermions
⁵⁴⁵ are isosinglets ψ_R . For the first generation of leptons and quarks this represents

$$\chi_L = \begin{pmatrix} \nu_e \\ e \end{pmatrix}_L, \quad \begin{pmatrix} u \\ d \end{pmatrix}_L$$

$$\psi_R = e_R, \quad u_R, d_R \quad (2.9)$$

⁵⁴⁶ Imposing local gauge invariance within \mathcal{L}_{EWK} is once again achieved by modifying the
⁵⁴⁷ covariant derivative

$$D_\mu = \partial_\mu - \frac{ig}{2}\tau^i W_\mu^i - \frac{ig'}{2}YB_\mu, \quad (2.10)$$

⁵⁴⁸ where g and g' are the coupling constant of the $SU(2)_L$ and $U(1)_Y$ groups respectively.
⁵⁴⁹ Taking the example of the first generation of fermions defined in Equation.(2.9), with input
⁵⁵⁰ hypercharge values of -1 and -2 for χ_L and e_R respectively, would lead to a Lagrangian
⁵⁵¹ \mathcal{L}_1 of the form,

$$\mathcal{L}_1 = \bar{\chi}_L \gamma^\mu [i\partial_\mu - g \frac{1}{2} \tau \cdot W_\mu - g' (-\frac{1}{2}) B_\mu] \chi_L$$

$$+ \bar{e}_R \gamma^\mu [i\partial_\mu - g' (-1) B_\mu] e_R - \frac{1}{4} W_{\mu\nu} \cdot W^{\mu\nu} - \frac{1}{4} B_{\mu\nu} B^{\mu\nu}. \quad (2.11)$$

⁵⁵² As in QED, these additional gauge fields introduce field strength tensors $B_{\mu\nu}$ and $W_{\mu\nu}$,

$$\hat{B}_{\mu\nu} = \partial_\mu \hat{B}_\nu - \partial_\nu \hat{B}_\mu \quad (2.12)$$

$$\hat{W}_{\mu\nu} = \partial_\mu \hat{W}_\nu - \partial_\nu \hat{W}_\mu - g \hat{W}_\mu \times \hat{W}_\mu \quad (2.13)$$

⁵⁵³ corresponding to the kinetic energy and self coupling of the W_μ fields and the kinetic
⁵⁵⁴ energy term of the B_μ field.

- 555 None of these gauge bosons are physical particles, and instead linear combinations of
 556 these gauge bosons make up γ and the W and Z bosons, defined as

$$W^\pm = \frac{1}{\sqrt{2}} (W_\mu^1 \mp iW_\mu^2) \quad \begin{pmatrix} Z_\mu \\ A_\mu \end{pmatrix} = \begin{pmatrix} \cos\theta_W & -\sin\theta_W \\ \sin\theta_W & \cos\theta_W \end{pmatrix} \begin{pmatrix} W_\mu^3 \\ B_\mu \end{pmatrix} \quad (2.14)$$

- 557 where the mixing angle, $\theta_w = \tan^{-1} \frac{g'}{g}$, relates the coupling of the neutral weak and
 558 electromagnetic interactions.

559 As in the case of the formulation of the QED Lagrangian there remains no mass term for
 560 the photon. However this is also the case for the W, Z and fermions in the Lagrangian,
 561 contrary to experimental measurement. Any explicit introduction of mass terms would
 562 break the symmetry of the Lagrangian and instead mass terms can be introduced through
 563 spontaneous breaking of the EWK symmetry via the Higgs mechanism.

564 The Higgs mechanism induces spontaneous symmetry breaking through the introduction
 565 of a complex scalar SU(2) doublet field ϕ which attains a non-zero Vacuum Expectation
 566 Value (VEV) [17][18][19][20].

$$\phi = \begin{pmatrix} \phi^+ \\ \phi^0 \end{pmatrix} \quad \text{with} \quad \begin{aligned} \phi^+ &\equiv (\phi_1 + i\phi_2)/\sqrt{2} \\ \phi^0 &\equiv (\phi_3 + i\phi_4)/\sqrt{2} \end{aligned} \quad (2.15)$$

- 567 The Lagrangian defined in Equation (2.11) attains an additional term \mathcal{L}_{Higgs} of the form

$$\mathcal{L}_{Higgs} = \overbrace{(D_\mu\phi)^\dagger(D^\mu\phi)}^{\text{kinetic}} - \overbrace{\mu^2\phi^\dagger\phi - \lambda(\phi^\dagger\phi)^2}^{\text{potential } V(\phi)} \quad (\mu^2, \lambda) > 0 \in \mathbb{R},$$

$$\mathcal{L}_{SM} = \mathcal{L}_{EWK} + \mathcal{L}_{Higgs}, \quad (2.16)$$

- 568 where the covariant derivative D_μ is that defined in Equation (2.10). The last two terms
 569 of \mathcal{L}_{Higgs} correspond to the Higgs potential, in which real positive values of μ^2 and λ are
 570 required to ensure the generation of masses for the bosons and leptons. The minimum of

571 this potential is found at $\phi^\dagger \phi = \frac{1}{2}(\phi_1^2 + \phi_2^2 + \phi_3^2 + \phi_4^2) = \mu^2/\lambda = v^2$, where v represents
572 the **VEV**.

573 Defining the ground state of the ϕ field to be consistent with the $V(\phi)$ minimum, and
574 then expanding around a ground state chosen to maintain an unbroken electromagnetic
575 symmetry thus preserving a zero photon mass [21] leads to

$$\phi_0 = \sqrt{\frac{1}{2}} \begin{pmatrix} 0 \\ v \end{pmatrix}, \quad \phi(x) = e^{i\tau \cdot \theta(x)/v} \sqrt{\frac{1}{2}} \begin{pmatrix} 0 \\ v + h(x) \end{pmatrix}, \quad (2.17)$$

576 where the fluctuations from the vacuum ϕ_0 are parametrized in terms of four real fields,
577 $\theta_1, \theta_2, \theta_3$ and $h(x)$.

578 Choosing to gauge away the three massless Goldstone boson fields by setting $\theta(x)$ to zero
579 and substituting $\phi(x)$ back into kinetic term of \mathcal{L}_{Higgs} from Equation (2.16) leads to mass
580 terms for the W^\pm and Z bosons

$$(D_\mu \phi)^\dagger (D^\mu \phi) = \frac{1}{2} (\partial_\mu h)^2 + \frac{g^2 v^2}{2} W_\mu^+ W^{-\mu} + \frac{v^2 g^2}{8 \cos^2 \theta_w} Z_\mu Z^\mu + 0 A_\mu A^\mu, \quad (2.18)$$

581 where the relations between the physical and electroweak gauge fields from Equation
582 (2.14) are used. The W^\pm and Z bosons can then be determined to be

$$M_W = \frac{1}{2} g v \quad M_Z = \frac{1}{2} \frac{g v}{\cos \theta_w}. \quad (2.19)$$

583 This mechanism is also used to generate fermion masses by introducing a Yukawa coupling
584 between the fermions and the ϕ field [22], with the coupling strength of a particle to
585 the ϕ field governing its mass. Additionally a scalar boson h with mass $m_h = v \sqrt{\frac{\lambda}{2}}$, is
586 also predicted as a result of this spontaneous symmetry breaking and became known as
587 the Higgs boson. Its discovery by the **CMS** and **ATLAS** experiments in 2012 is the first
588 direct evidence to support this method of mass generation within the **SM**.

589 **2.2. Motivation for Physics Beyond the Standard
590 Model**

591 As has been described, the **SM** has proved to be a very successful theory, predicting the
592 existence of the W^\pm and Z bosons and the top quark long before they were experimentally
593 observed. However the theory does not accurately describe all observed phenomena and
594 has some fundamental theoretical flaws that hint at the need for additional extensions to
595 the current theory.

596 On a theoretical level, the **SM** is unable to incorporate the gravitational interactions of
597 fundamental particles within the theory. Whilst at the electroweak energy scales the
598 relative strength of gravity is negligible compared to the other three fundamental forces,
599 at much higher energy scales, $M_{\text{planck}} \sim 10^{18} \text{GeV}$, quantum gravitational effects become
600 increasingly dominant. The failure to reconcile gravity within the **SM**, demonstrates that
601 the **SM** must become invalid at some higher energy scale.

602 Some other deficiencies with the **SM** include the fact that the predicted rate of Charge-
603 Parity violation does not account for the matter dominated universe which we inhabit,
604 and the **SM** prediction of zero neutrino mass conflicts with the observation of neutrino
605 flavour mixing, attributed to mixing between neutrino mass eigenstates [23][24].

606 Perhaps one of the most glaring gaps in the predictive power of the **SM** is that there
607 exists no candidate to explain the cosmic dark matter observed in galactic structures
608 through indirect techniques including gravitational lensing and measurement of the
609 orbital velocity of stars at galactic edges. Any such candidate must be very weakly
610 interacting but must also be stable, owing to the lack of direct detection of the decay
611 products of such a process. Therefore a stable dark matter candidate, is one of the
612 main obstacles to address for any Beyond Standard Model (**BSM**) physics model.

613 The recent discovery of the Higgs boson whilst a significant victory for the predictive
614 power of the **SM**, brings with it still unresolved questions. This issue is commonly
615 described as the “hierarchy problem”.

616 In the absence of new physics between the TeV and Planck scale, calculating beyond
617 tree-level contributions to the Higgs mass term given by its self interaction, result in
618 divergent terms that push the Higgs mass up to the planck mass M_{planck} .

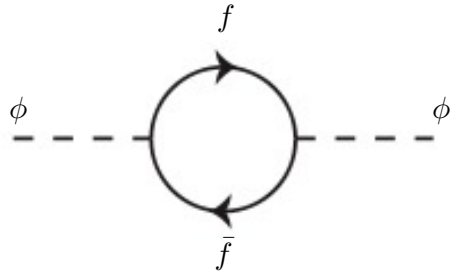


Figure 2.1.: One loop quantum corrections to the Higgs squared mass parameter m_h^2 due to a fermion.

619 This can be demonstrated by considering the one loop quantum correction to the Higgs
 620 mass with a fermion f , shown in Figure 2.1 with mass m_f . The Higgs field couples to f
 621 with a term in the Lagrangian $-\lambda_f h \bar{f} f$, yielding a correction of the form [25],

$$\delta m_h^2 = -\frac{|\lambda_f|^2}{8\pi^2} \Lambda^2 + \dots, \quad (2.20)$$

622 where λ_f represents the coupling strength for each type of fermion $\propto m_f$, and Λ the
 623 cutoff energy scale at which the **SM** ceases to be a valid theory.

624 To recover the mass of the now discovered Higgs boson would require a fine-tuning of
 625 the parameters to cancel out these mass corrections of the Higgs mass to the scale of
 626 30 orders of magnitude. This appears as an unnatural solution to physicists and it is
 627 this hierarchy problem that provides one of the strongest motivations for the theory of
 628 SUperSYmmetry (**SUSY**).

629 2.3. Supersymmetry Overview

630 Supersymmetry provides potential solutions to many of the issues raised in the previous
 631 section. It provides a dark matter candidate, can explain baryogenesis in the early
 632 universe and also provides an elegant solution to the hierarchy problem [26][27][28][29].
 633 At its heart it represents a new space-time symmetry that relates fermions and bosons.
 634 This symmetry converts bosonic states into fermionic states, and vice versa, see Equation
 635 (2.21) ,

$$Q|Boson\rangle = |Fermion\rangle \quad Q|Fermion\rangle = |Boson\rangle, \quad (2.21)$$

636 where the operator Q is the generator of these transformations. Quantum field theories
 637 which are invariant under such transformations are called supersymmetric.

638 This symmetry operator therefore acts upon a particles spin altering it by a half integer
 639 value. The consequences of the introduction of this additional space-time symmetry
 640 introduce a new rich phenomenology. For example in supersymmetric theories, both
 641 the left handed $SU(2)$ doublet and right handed singlet of fermions will have a spin-0
 642 superpartner, containing the same electric charge, weak isospin, and colour as its **SM**
 643 partner. In the case of the leptons $(\nu_l, l)_L$, they will have two superpartners, a sneutrino
 644 $\tilde{\nu}_l{}_L$ and a slepton \tilde{l}_L , whilst the singlet l_R also has a superpartner slepton \tilde{l}_R .

645 Each particle in a supersymmetric theory is paired together with their superpartners as
 646 a result of these supersymmetric transformations in a so called supermultiplet. These
 647 superpartners will then consequently also contribute to the corrections to the Higgs mass.
 648 Bosonic and fermionic loops contributing to the correction appear with opposite signs,
 649 and therefore cancellation of these divergent terms will stabilise the Higgs mass, solving
 650 the hierarchy problem [30][31].

651 One of the simplest forms of **SUSY**, is to simply have a set of **SM** supersymmetric partners
 652 with the same mass and interactions as their counterparts. However the currently lack
 653 of any experimental evidence for the predicted sparticle spectrum implies **SUSY** must
 654 be a broken symmetry in which any sparticle masses must be greater than their SM
 655 counterparts.

656 There exist many techniques which can induce supersymmetric breaking [32][33][34]. Of
 657 particular interest to experimental physicists are those at which the breaking scale is
 658 of an order that is experimentally accessible to the **LHC** i.e. \sim TeV scale. Whilst
 659 there is no requirement for supersymmetric breaking to occur at this energy scale, for
 660 supersymmetry to provide a solution to the hierarchy problem, it is necessary for this
 661 scale to not differ too drastically from the **EWK** scale [35][36].

662 2.3.1. R-Parity

663 Some supersymmetric theories also present a solution to the dark matter problem. These
 664 theories contain a Lightest Supersymmetric Partner (**LSP**), which matches the criteria of
 665 a Weakly Interacting Massive Particle (**WIMP**) required by cosmological observation if
 666 R-parity is conserved.

667 Baryon (B) and Lepton (L) number conservation is forbidden in the **SM** by renormal-
 668 isability requirements. The violation of Baryon or Lepton number results in a proton
 669 lifetime much shorter than those set by experimental limits [37]. Another symmetry
 670 called R-parity is then often introduced to **SUSY** theories to maintain baryon and lepton
 671 conservation.

672 R-parity is described by the equation

$$R_P = (-1)^{3(B-L)+2s}, \quad (2.22)$$

673 where s represents the spin of the particles. $B = \pm \frac{1}{3}$ for quarks/antiquarks and $B = 0$
 674 for all others, $L = \pm 1$ for leptons/antileptons, $L = 0$ for all others.

675 R-parity ensures the stability of the proton in **SUSY** models, and also has other conse-
 676 quences for the production and decay of supersymmetric particles. In particle colliders
 677 supersymmetric particles can only be pair produced, and similarly the decay of any pro-
 678 duced supersymmetric particle is restricted to a **SM** particle and a lighter supersymmetric
 679 particle as allowed by conservation laws. A further implication of R-parity is that once a
 680 supersymmetric particle has decayed to the **LSP** it remains stable, unable to decay into
 681 a **SM** particle.

682 A **LSP** will not interact in a detector at a particle collider, leaving behind a missing
 683 energy \cancel{E}_T signature. The assumption of R-parity and its consequences are used to
 684 determine the physical motivation and search strategies for **SUSY** models at the **LHC**.

685 2.4. Experimental Signatures of **SUSY** at the **LHC**

686 Should strongly interacting sparticles be within the experimental reach of the **LHC**, then
 687 it is expected that they can be produced in a variety of ways :

- 688 • squark/anti-squark and gluino pairs can be produced via both gluon fusion and
- 689 quark/anti-quark scattering.
- 690 • a gluino and squark produced together via quark-gluon scattering
- 691 • squark pairs produced via quark-quark scattering

692 Whilst most **SUSY** searches invoke the requirement of R-parity to explore parameter
693 phase space, there still exist a whole plethora of possible **SUSY** model topologies which
694 are still to be discovered at the **LHC**.

695 During the 2011 run period at a $\sqrt{s} = 7$ TeV, particular models were used to benchmark
696 performance and experimental reach of both **CMS** searches and previous experiments.
697 The Compressed Minimal SuperSymmetric Model (**CMSSM**) was initially chosen for a
698 number of reasons [38], one of the most compelling being the reduction from up to 105
699 new parameters that can be introduced by **SUSY** in addition to the existing 19 of the
700 **SM**, to just 5 free extra free parameters. It was this simplicity, combined with the theory
701 not requiring any fine tuning of particle masses to produce the experimentally verified
702 **SM** that made it an attractive model to interpret physics results.

703 However recent results from the **LHC** now strongly disfavour large swathes of **CMSSM**
704 parameter space [39][40][41]. In the face of such results a more pragmatic model indepen-
705 dent search strategy is now applied across most **SUSY** searches at the **LHC**, see Section
706 (2.4.1).

707 As previously stated, a stable **LSP** that exhibits the properties of a dark matter candidate
708 would be weakly interacting and therefore will not be directly detected in a detector envi-
709 ronment. Additionally the cascade decays of supersymmetric particles to the **LSP** would
710 also result in significant hadronic activity. These signatures can then be characterised
711 through large amounts of hadronic jets (see Section (3.3.1)), leptons and a significant
712 amount of missing energy dependent upon the size of the mass splitting between the
713 **LSP** and the supersymmetric particle it has decayed from.

714 The **SM** contains processes which can exhibit a similar event topology to that described
715 above. The largest contribution coming from the general QCD environment of a hadron
716 collider. A multitude of different analytical techniques are used by experimental physicists
717 to reduce or estimate any reducible or irreducible backgrounds, allowing a possible **SUSY**
718 signature to be extracted. The techniques employed within this thesis are described in
719 great detail within Section (4.1).

720 2.4.1. Simplified models

721 With such a variety of different ways for a **SUSY** signal to manifest itself, it is necessary
 722 to be able to interpret experimental reach through the masses of gluinos and squarks
 723 which can be excluded by experimental searches rather than on a model specific basis.

724 This is accomplished through **SMS** models, which are defined by a set of hypothetical
 725 particles and a sequence of their production and decay [42][43]. In the **SMS** models
 726 considered within this thesis, only the production process for the two primary particles
 727 are considered. Each primary particle can undergo a direct or a cascade decay through
 728 an intermediate new particle. At the end of each decay chain there remains a neutral,
 729 undetected **LSP** particle, denoted $\tilde{\chi}_{LSP}$ which can represent a neutralino or gravitino.
 730 Essentially it is easier to consider each **SMS** with branching ratios set to 100% The
 731 masses of the primary particle and the **LSP** remain as free parameters, in which the
 732 absolute value and relative difference between the primary and **LSP** particle alter the
 733 kinematics of the event.

734 Different **SMS** models are denoted with a T-prefix, with a summary of the types interpreted
 735 within this thesis listed below [44].

- 736 • **T1,T1xxxx**, models represent a simplified version of gluino pair production with
 737 each gluino (superpartner to the gluon) undergoing a three-body decay to a quark-
 738 antiquark pair and the **LSP** (i.e. $\tilde{g} \rightarrow q\bar{q}\tilde{\chi}_{LSP}$). The resultant final state from this
 739 decay is typically 4 jets + \cancel{E}_T in the absence of initial/final state radiation and
 740 detector effects. xxxx denotes models in which the quarks are of a specific flavour,
 741 typically t or b quark-antiquarks.

- 742 • **T2,T2xx**, models represent a simplified version of squark anti-squark production
 743 with each squark undergoing a two-body decay into a light-flavour quark and **LSP**
 744 (i.e. $\tilde{q} \rightarrow q\tilde{\chi}_{LSP}$). This results in final states with less jets than gluino mediated
 745 production, typically 2 jets + \cancel{E}_T when again ignoring the effect of initial/final state
 746 radiation and detector effects. xx models again represent decays in which both the
 747 quark and the squark within the decay is of a specific flavour, typically \tilde{t}/t or \tilde{b}/b .

748 Models rich in b and t quarks are interpreted within this thesis as they remain of
 749 particular interest within “Natural **SUSY**” scenarios [45][46]. The largest contribution
 750 to the quadratic divergence in the Higgs mass parameter comes from a loop of top
 751 quarks via the Yukawa coupling. Cancellation of these divergences can be achieved in

⁷⁵² supersymmetric theories by requiring a light right handed top squark, \tilde{t}_R , and left-handed
⁷⁵³ double $SU(2)_L$ doublet containing top and bottom squarks, $(\tilde{t}, \tilde{b})_L$ [47].

⁷⁵⁴ These theories therefore solve the hierarchy problem by predicting light \sim EWK scale
⁷⁵⁵ third generation sleptons, to be accessible at the LHC. Search strategies involving the
⁷⁵⁶ requirement of b-tagging (see Section (3.3.2)) are used to give sensitivity to these type of
⁷⁵⁷ SUSY scenarios and are discussed in greater detail within Chapter 4.

⁷⁵⁸ Two example decay chains are shown in Figure 2.2; the pair production of gluinos (T1)
⁷⁵⁹ and the pair production of squarks (T2) decaying into SM particles and LSP's.

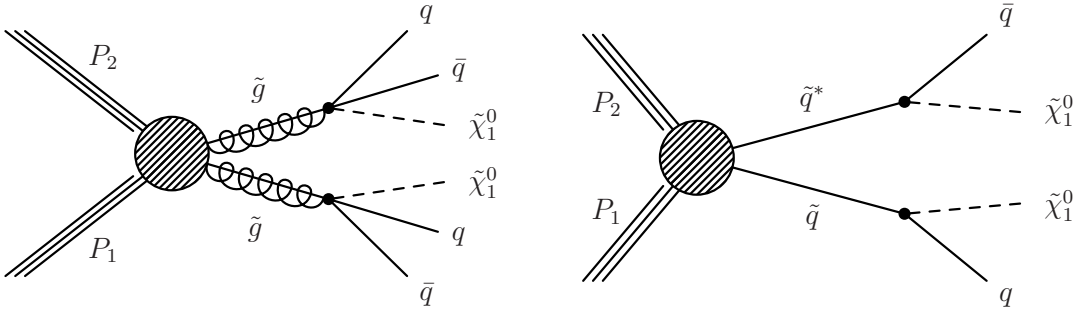


Figure 2.2.: Two example SMS model decays (T1 (left), T2 (right)), which are used in interpretations of physics reach by CMS.

Chapter 3.

⁷⁶⁰ The LHC And The CMS Detector

⁷⁶¹ Probing the SM for signs of new physics would not be possible without the immensely
⁷⁶² complex electronics and machinery that makes the TeV energy scale accessible for the
⁷⁶³ first time. This chapter will describe both the LHC based at European Organization
⁷⁶⁴ for Nuclear Research (CERN) and the Compact Muon Solenoid (CMS) detector, being
⁷⁶⁵ the experiment the author is a member of. Section (3.2) serves to introduce an overview
⁷⁶⁶ of the different components of the CMS detector, with specific components relevant to
⁷⁶⁷ the search for supersymmetric particles described in greater detail. Section (3.3) will
⁷⁶⁸ focus on event and object reconstruction again with more emphasis on jet level quantities
⁷⁶⁹ which are most relevant to the author's analysis research. Finally Section (3.4) will
⁷⁷⁰ cover work performed by the author, as service to the CMS Collaboration, in measuring
⁷⁷¹ the performance of the Global Calorimeter Trigger (GCT) component of the L1 trigger
⁷⁷² during the 2012-2013 run period.

⁷⁷³ 3.1. The LHC

⁷⁷⁴ The LHC is a storage ring, accelerator, and collider of circulating beams of protons or
⁷⁷⁵ ions. Housed in the tunnel dug for the Large Electron-Positron collider (LEP), it is
⁷⁷⁶ approximately 27 km in circumference, 100 m underground, and straddles the border
⁷⁷⁷ between France and Switzerland outside of Geneva. It is currently the only collider
⁷⁷⁸ in operation that is able to study physics at the TeV scale. A double-ring circular
⁷⁷⁹ synchrotron, it was designed to collide both proton-proton (pp) and heavy ion (PbPb)
⁷⁸⁰ with a centre of mass energy $\sqrt{s} = 14$ TeV at a final design luminosity of $10^{34}\text{cm}^{-2}\text{s}^{-1}$.

These counter-circulating beams of protons/Pb ions are merged in four sections around the ring to enable collisions of the beams, with each interaction point being home to one of the four major experiments; A Large Ion Collider Experiment (**ALICE**) [48] , A Toroidal LHC ApparatuS (**ATLAS**) [49], Compact Muon Solenoid (**CMS**) [50] and Large Hadron Collider Beauty (**LHCb**) [51] which record the resultant collisions. The layout of the **LHC** ring is shown in Figure 3.1. The remaining four sections contain acceleration,collimation and beam dump systems. In the eight arc sections, the beams are steered by magnetic fields of up to 8 T provided by super conduction dipole magnets, which are maintained at temperatures of 2 K using superfluid helium. Additional magnets for focusing and corrections are also present in straight sections within the arcs and near the interaction regions where the detectors are situated.

793

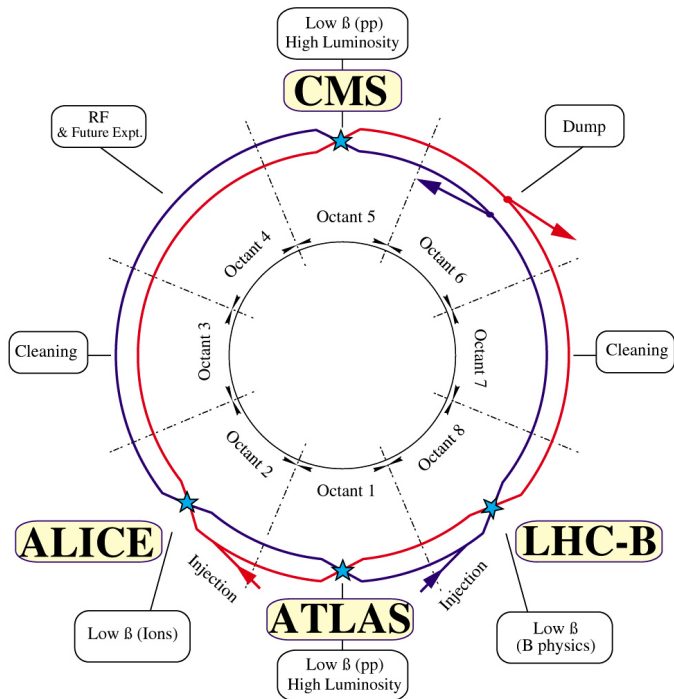


Figure 3.1.: A top down layout of the LHC. [52], with the position of the four main detectors labelled.

Proton beams are formed inside the Proton Synchrotron (**PS**) from bunches of protons 50 ns apart with an energy of 26 GeV. The protons are then accelerated in the Super Proton Synchrotron (**SPS**) to 450 GeV before being injected into the **LHC**. These **LHC** proton beams consists of many “bunches” i.e. approximately 1.1×10^{11} protons localized into less than 1 ns in the direction of motion. Before collision the beams are ramped to 4

799 TeV (2012) per beam in a process involving increasing the current passing through the
 800 dipole magnets. Once the desired \sqrt{s} energy is reached then the beams are allowed to
 801 collide at the interaction points. The luminosity falls regularly as the run progresses as
 802 protons are lost in collisions, and eventually the beam is dumped before repeating the
 803 process again.

804

805 Colliding the beams produced an instantaneous luminosity of approximately 5×10^{33}
 806 $\text{cm}^{-2}\text{s}^{-1}$ during the 2012 run. The high number of protons in each bunch increases
 807 the likelihood of multiple interactions with each crossing of the counter-circulating
 808 beams. This leads to isotropic energy depositions within the detectors positioned at these
 809 interaction points, increasing the energy scale of the underlying event. This is known as
 810 pile-up and the counteracting of it's effects are important to the many measurements
 811 performed at the **LHC**.

812 In the early phase of prolonged operation after the initial shutdown the machine operated
 813 in 2010-2011 at 3.5 TeV per beam, $\sqrt{s} = 7$ TeV, delivering 6.13 fb^{-1} of data [53]. During
 814 the 2012-2013 run period, data was collected at an increased $\sqrt{s} = 8$ TeV improving the
 815 sensitivity of searches for new physics. Over the whole run period 23.3 fb^{-1} of data was
 816 delivered of which 21.8 fb^{-1} was recorded by the **CMS** detector as shown in Figure 3.2
 817 [53]. A total of 12 fb^{-1} of 8 TeV certified data was collected by October 2012, and it is
 818 this data which forms the basis of the results discussed within this thesis.

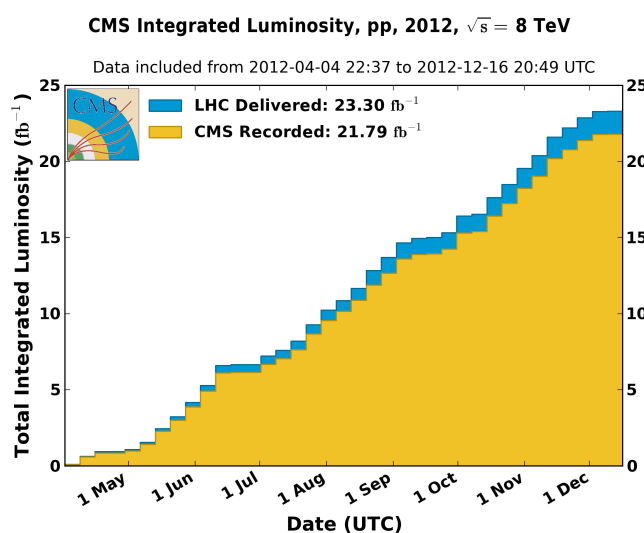


Figure 3.2.: The total integrated luminosity delivered to and collected by **CMS** during the 2012 8 TeV pp runs.

⁸¹⁹ 3.2. The CMS Detector

⁸²⁰ The Compact Muon Solenoid (**CMS**) detector is one of two general purpose detectors
⁸²¹ at the **LHC** designed to search for new physics. The detector is designed to provide
⁸²² efficient identification and measurement of many physics objects including photons,
⁸²³ electrons, muons, taus, and hadronic showers over wide ranges of transverse momentum
⁸²⁴ and direction. Its nearly 4π coverage in solid angle allows for accurate measurement of
⁸²⁵ global transverse momentum imbalance. These design factors give **CMS** the ability to
⁸²⁶ search for direct production of **SUSY** particles at the TeV scale, making the search for
⁸²⁷ Supersymmetric particles one of the highest priorities among the wide range of physics
⁸²⁸ programmes at **CMS**.

⁸²⁹

⁸³⁰ **CMS** uses a right-handed Cartesian coordinate system with the origin at the interaction
⁸³¹ point and the z-axis pointing along the beam axis, the x-axis points radially inwards to
⁸³² the centre of the collider ring, with the y-axis points vertically upward. The azimuthal
⁸³³ angle, ϕ ranging between $[-\pi, \pi]$ is defined in the x-y plane starting from the x-axis. The
⁸³⁴ polar angle θ is measured from the z axis. The common convention in particle physics is
⁸³⁵ to express an out going particle in terms of ϕ and its pseudorapidity defined as

$$\eta = -\log \tan \left(\frac{\theta}{2} \right). \quad (3.1)$$

⁸³⁶ The variable $\Delta R = \sqrt{\Delta\phi^2 + \Delta\eta^2}$ is commonly used to define angular distance between
⁸³⁷ objects within the detector and additionally energy and momentum is typically measured
⁸³⁸ in the transverse plane perpendicular to the beam line. These values are calculated
⁸³⁹ from the x and y components of the object and are denoted as $E_T = E \sin \theta$ and
⁸⁴⁰ $p_T = \sqrt{p_x^2 + p_y^2}$.

⁸⁴¹ 3.2.1. Detector subsystems

⁸⁴² As the range of particles produced in pp collisions interact in different ways with mat-
⁸⁴³ ter, **CMS** is divided into subdetector systems, which perform complementary roles to
⁸⁴⁴ identify the identity, mass and momentum of the different physics objects present in
⁸⁴⁵ each event. These detector sub-systems contained within **CMS** are wrapped in layers

846 around a central 13 m long 4 T super conducting solenoid as shown in Figure 3.3. With
 847 the endcaps closed , CMS is a cylinder of length 22 m, diameter 15 m, and mass 12.5
 848 kilotons. A more detailed complete description of the detector can be found elsewhere [50].
 849

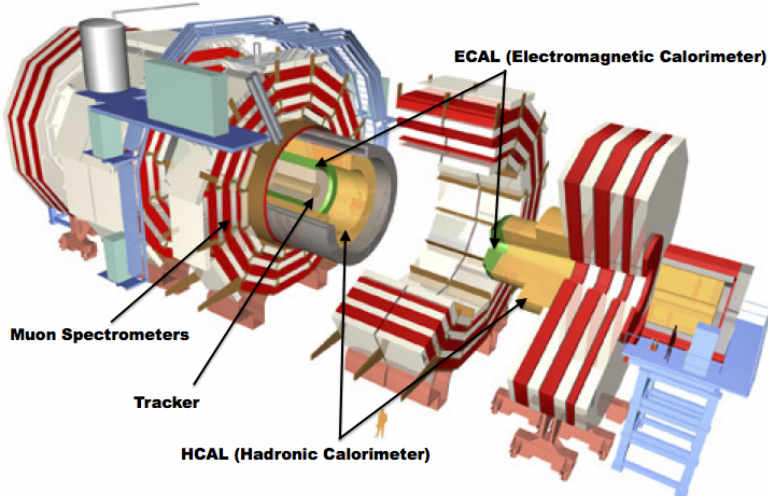


Figure 3.3.: A pictorial depiction of the CMS detector with the main detector subsystems labelled. [54]

850 3.2.2. Tracker

851 The inner-most subdetector of the barrel is the multi-layer silicon tracker, formed of a
 852 pixel detector component encased by layers of silicon strip detectors. The pixel detector
 853 consists of three layers of silicon pixel sensors providing measurements of the momentum,
 854 position coordinates of the charged particles as they pass, and the location of primary
 855 and secondary vertices between 4cm and 10cm transverse to the beam. Outside the pixel
 856 detector, ten cylindrical layers of silicon strip detectors extend the tracking system out to
 857 a radius of 1.20m from the beam line. The tracking system provides efficient and precise
 858 determination of the charges, momenta, and impact parameters of charged particles with
 859 the geometry of the tracker extending to cover a rapidity range up to $|\eta| < 2.5$.
 860

861 The tracking system also plays a crucial part in the identification of jets originating
 862 from b-quarks through measurement of displaced secondary vertices, which is covered in
 863 more detail in Section (3.3.2). The identification of b-jets is important in many searches

864 for natural SUSY models and forms an important part of the inclusive search strategy
865 described within Section (4.2).

866 **3.2.3. Electromagnetic calorimeter**

867 Immediately outside of the tracker, but still within the magnet core, sits the Electromag-
868 netic CALorimeter (**ECAL**). Covering a pseudorapidity up to $|\eta| < 3$ and comprising
869 of over 75,000 PbWO₄ (lead tungstate) crystals that scintillate as particles deposit energy,
870 the **ECAL** provides high resolution measurements of the electromagnetic showers from
871 photons, electrons in the detector.

872

873 Lead tungstate is used because of its short radiation length ($X_0 \sim 0.9\text{cm}$) and small
874 Molieré radius ($\sim 2.1\text{cm}$) leading to high granularity and resolution. It's fast scintillation
875 time ($\sim 25\text{ns}$) reduces the effects of pile-up due to energy from previous collisions still
876 being read out, and its radiation hardness gives it longevity. The crystals are arranged
877 in modules which surround the beam line in a non-projective geometry, angled at 3°
878 with respect to the interaction point to minimise the risk of particles escaping down the
879 cracks between the crystals.

880

881 The **ECAL** is primarily composed of two sections, the Electromagnetic CALorime-
882 ter Barrel (**EB**) which extends in pseudo-rapidity to $|\eta| < 1.479$ with a crystal front
883 cross section of $22 \times 22\text{ mm}$ and a length of 230 mm corresponding to 25.8 radiation
884 lengths, and the Electromagnetic CALorimeter Endcap (**EE**) covering a rapidity range
885 of $1.479 < |\eta| < 3.0$, which consists of two identical detectors on either side of the
886 **EB**. A lead-silicon sampling ‘pre-shower’ detector Electromagnetic CALorimeter pre-
887 Shower (**ES**) is placed before the endcaps to aid in the identification of neutral pions.
888 Their arrangement are shown in Figure 3.4.

889

890 Scintillation photons from the lead tungstate crystals are instrumented with Avalanche
891 Photo-Diodes (**APD**) and Vacuum Photo-Triodes (**VPT**) located in the **EB** and **EE**
892 respectively, converting the scintillating light into an electric signal which is consequently
893 used to determine the amount of energy deposited within the crystal . These instruments
894 are chosen for their resistance under operation to the strong magnetic field of **CMS**. The
895 scintillation of the **ECAL** crystals as well as the response of the **APDs** varies as a function

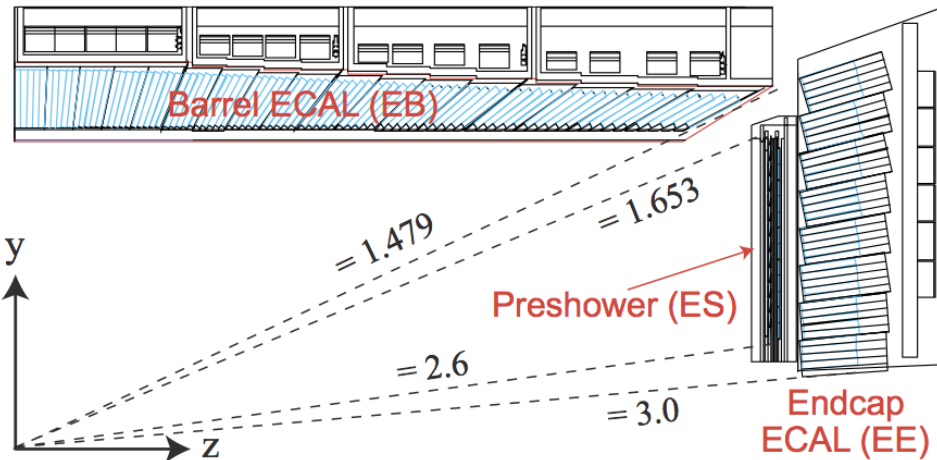


Figure 3.4.: Illustration of the **ECAL** showing the arrangement of the lead tungstate crystals in the **EB** and **EE**. The **ES** is also shown and is located in front of the **EE** [55].

896 of temperature and so cooling systems continually maintain an overall constant **ECAL**
 897 temperature $\pm 0.05^\circ\text{C}$.

898 3.2.4. Hadronic calorimeter

899 Beyond the **ECAL** lies the Hadronic CALorimeter (**HCAL**) which is responsible for
 900 the accurate measurement of hadronic showers, crucial for analyses involving jets or
 901 missing energy signatures. The **HCAL** is a sampling calorimeter which consists of al-
 902 ternating layers of brass absorber and plastic scintillator, except in the hadron forward
 903 ($3.0 < |\eta| < 5.0$) region in which steel absorbers and quartz fibre scintillators are used
 904 because of their increased radiation tolerance. Hadron showers are initiated in the
 905 absorber layers inducing scintillation in the plastic scintillator tiles. These scintillation
 906 photons are converted by wavelength shifting fibres for read-out by hybrid photodiodes.
 907

908 The **HCAL**'s size is constrained to a compact size by the presence of the solenoid, re-
 909 quiring the placement of an additional outer calorimeter on the outside of the solenoid
 910 to increase the sampling depth of the **HCAL**. A schematic of the **HCAL** can be seen in
 911 Figure 3.5.

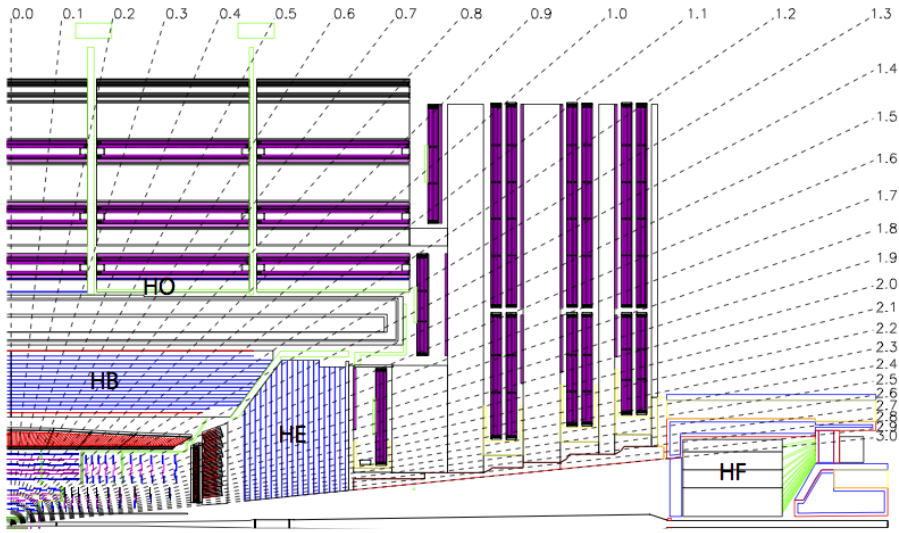


Figure 3.5.: Schematic of the hadron calorimeters in the r-z plane, showing the locations of the **HCAL** components and the **HF**. [50].

913 The **HCAL** covers the range $|\eta| < 5$ and consists of four subdetectors: the Hadron
 914 Barrel (**HB**) $|\eta| < 1.3$, the Hadron Outer (**HO**), the Hadron Endcaps (**HE**) $1.3 < |\eta| < 3.0$
 915 and the Hadron Forward (**HF**). The **HB**, contained between the outer edge of the **ECAL**
 916 and the inner edge of the solenoid is formed of 36 azimuthal wedges which are split
 917 between two half-barrel segments. Each wedge is segmented into four azimuthal angle
 918 (ϕ) sectors, and each half-barrel is further segmented into 16 η towers. The electronic
 919 readout chain, channels the light from the active scintillator layers from one ϕ -segment
 920 and all η -towers of a half-barrel to a Hybrid Photo Diode (**HPD**).

921 The relatively short number of interaction lengths (λ_l , the distance a hadron will travel
 922 through the absorber material before it has lost $\frac{1}{e}$ of its energy) within the **HB**, the lowest
 923 being $\lambda_l = 5.82$ for $|\eta| = 0$, facilitates the need for the ‘tail catching’ **HO** to increase the
 924 sampling depth in the central barrel rapidity region $|\eta| < 1.3$ to 11 interaction lengths .
 925 Significant fractions of the hadrons energy will be deposited in the **ECAL** as it passed
 926 through the detector. Therefore measurements of hadron energies in the central regions
 927 $|\eta| < 3.0$ use both the **ECAL** and **HCAL** to reconstruct the true energy from showering
 928 hadrons.

929 **3.2.5. Muon systems**

930 Muons being too massive to radiate away energy via Bremsstrahlung, interact little in
931 the calorimeters and mostly pass through the detector until they reach the system of
932 muon detectors which forms the outer most part of the CMS detector.

933 Outside of the superconducting solenoid are four muon detection layers interleaved with
934 the iron return yokes which measure the muons energy via ionisation of gas within
935 detector elements. Three types of gaseous chamber are used. The Drift Tube (DT),
936 Cathode Stripe Chamber (CSC), and Resistive Plate Chamber (RPC) systems provide
937 efficient detection of muons with pseudo-rapidity $|\eta| < 2.4$. The best reconstruction
938 performance is obtained when the muon chamber is combined with the inner tracking
939 information to determine muon trajectories and their momenta [56].

940

941 **3.3. Event Reconstruction and Object Definition**

942 The goal of event reconstruction is to take the raw information recorded by the detector
943 and to compute from it higher-level quantities which can be used at an analysis level.
944 These typically correspond to an individual particle’s energy and momenta, or groups of
945 particles which shower in a narrow cone and the overall global energy and momentum
946 balance of the event. The reconstruction of these objects are described in great detail in
947 [57], however covered below are brief descriptions of those which are most relevant to the
948 analysis detailed in Chapter 4.

949 **3.3.1. Jets**

950 Quarks and gluons are produced copiously at the LHC in the hard scattering of partons.
951 As these quarks and gluons fragment, they hadronise and decay into a group of strongly
952 interactive particles and their decay products. These streams of particles travel in the
953 same direction, as they have been “boosted” by the momentum of the primary hadron.
954 These collections of decay products are reconstructed and identified together as a “jet”.

955 At CMS jets are reconstructed from energy deposits in the detector using the anti-kt
956 algorithm [58] with size parameter $\Delta R = 0.5$. The anti-kt jet algorithm clusters jets by
957 defining a distance between hard (high p_T) and soft (low p_T) particles such that soft

958 particles are preferentially clustered with hard particles before being clustered between
959 themselves. This produces jets which are robust to soft particle radiation from the pile-up
960 conditions produced by the **LHC**.

961

962 There are two main type of jet reconstruction used at **CMS**, Calorimeter (Calo) and
963 Particle Flow (PF) jets [59]. Calorimeter jets are reconstructed using both the **ECAL**
964 and **HCAL** cells, combined into calorimeter towers . These calorimeter towers consist of
965 geometrically matched **HCAL** cells and **ECAL** crystals. Electronics noise is suppressed by
966 applying a threshold to the calorimeter cells, with pile-up effects reduced by a requirement
967 placed on the tower energy [60]. Calorimter jets are the jets used within the analyses
968 described in this thesis.

969 PF jets are formed from combining information from all of the **CMS** subdetectors systems
970 to determine which final state particles are present in the event. Generally, any particle
971 is expected to produce some combination of a track in the silicon tracker, a deposit in
972 the calorimeters, or a track in the muon system. The PF jet momentum and spatial
973 resolutions are greatly improved with respect to calorimeter jets, as the use of the tracking
974 detectors and of the high granularity of **ECAL** allows resolution and measurement of
975 charged hadrons and photons inside a jet, which together constitute $\sim 85\%$ of the jet
976 energy [61].

977 The jets reconstructed by the clustering algorithm in **CMS** typically have an energy
978 that differs to the ‘true’ energy measured by a perfect detector. This stems from the
979 non-linear and nonuniform response of the calorimeters as well as other residual effects
980 including pile-up and underlying events, and therefore additional corrections are applied
981 to recover a uniform relative response as a function of pseudo-rapidity. These are applied
982 as separate sub corrections [62].

- 983 • A PU correction is first applied to the jet. It subtracts the average extra energy
984 deposited in the jet that comes from other vertices present in the event and is
985 therefore not part of the hard jet itself.
- 986 • p_T and η dependant corrections derived from Monte Carlo simulations are used to
987 account for the non-uniform response of the detector.
- 988 • p_T and η residual corrections are applied to data only to correct for difference
989 between data and Monte Carlo. The residual is derived from QCD dijet samples
990 and the p_T residual from $\gamma+$ jet and $Z+$ jets samples in data.

⁹⁹¹ 3.3.2. B-tagging

⁹⁹² The decays of b quarks are suppressed by small CKM matrix elements. As a result, the
⁹⁹³ lifetimes of b-flavoured hadrons, produced in the fragmentation of b quarks, are relatively
⁹⁹⁴ long; \mathcal{O} 1ps. The identification of jets originating from b quarks is very important for
⁹⁹⁵ searches for new physics and for measurements of standard model processes.

⁹⁹⁶

⁹⁹⁷ Many different algorithms developed by CMS select b-quark jets based on variables such
⁹⁹⁸ as the impact parameters of the charged-particle tracks, the properties of reconstructed
⁹⁹⁹ decay vertices, and the presence or absence of a lepton, or combinations thereof [63]. One
¹⁰⁰⁰ of the most efficient of which is the Combined Secondary Vertex (CSV) which operates
¹⁰⁰¹ based on secondary vertex and track-based lifetime information, benchmarked in ‘Loose’,
¹⁰⁰² ‘Medium’ and ‘Tight’ working points, of which the medium point is the tagger used
¹⁰⁰³ within the α_T search detailed in Section (4.1).

¹⁰⁰⁴ Using the CSV tagger, a likelihood-based discriminator distinguishes between jets from
¹⁰⁰⁵ b-quarks, and those from charm or light quarks and gluons, which is shown in Figure 3.6.
¹⁰⁰⁶ The minimum thresholds on the discriminator for each working point correspond to the
¹⁰⁰⁷ misidentification probability for light-parton jets of 10%, 1%, and 0.1%, respectively, in
¹⁰⁰⁸ jets with an average p_T of about 80 GeV.

¹⁰⁰⁹ The b-tagging performance is evaluated to measure the b-jet tagging efficiency ϵ_b , and the
¹⁰¹⁰ misidentification probability of charm ϵ_c and light-parton jets ϵ_s . The tagging efficiencies
¹⁰¹¹ for each of these three jet flavours are compared between data and MC simulation, from
¹⁰¹² which a series of p_T and $|\eta|$ binned jet corrections are determined,

$$SF_{b,c,s} = \frac{\epsilon_{b,c,s}^{data}}{\epsilon_{b,c,s}^{MC}}. \quad (3.2)$$

¹⁰¹³ These are collectively named ‘Btag Scale Factors’ and allow MC simulation to accu-
¹⁰¹⁴ rately reflect the running conditions and performance of the tagging algorithm in data.
¹⁰¹⁵ Understanding of the b-tagging efficiency is essential in order to minimise systematic
¹⁰¹⁶ uncertainties in physics analyses that employ b-tagging.

¹⁰¹⁷

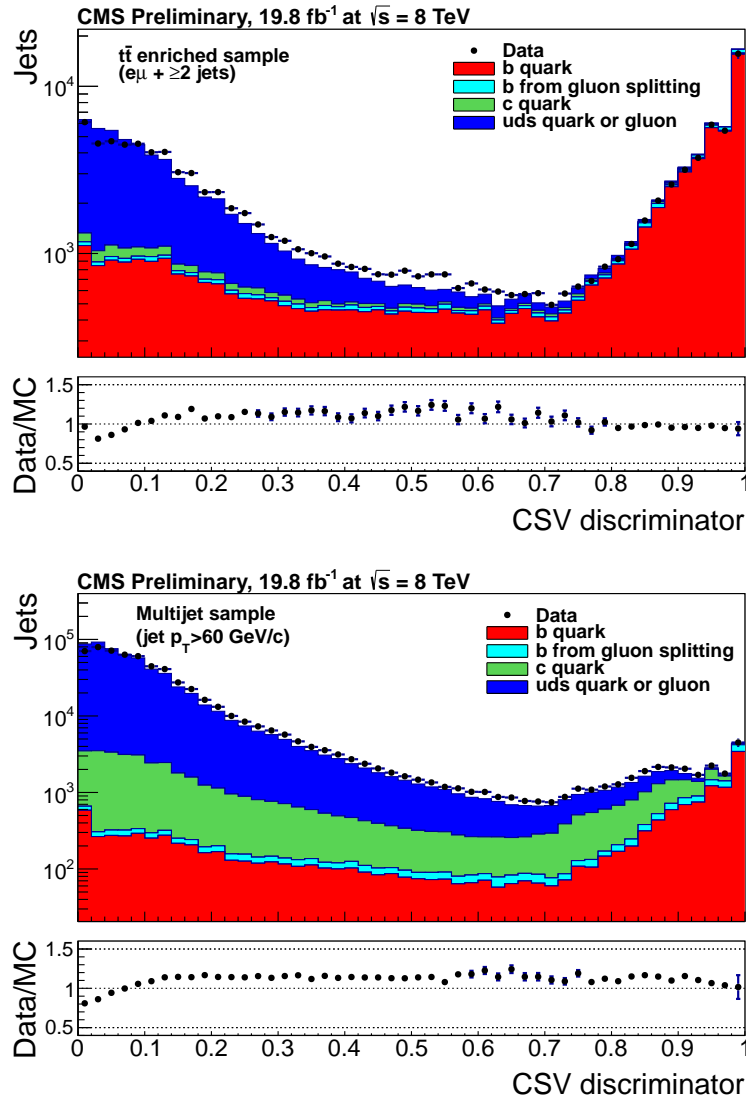


Figure 3.6.: CSV algorithm discriminator values in enriched $t\bar{t}$ bar (top) and inclusive multi jet samples (bottom) for b,c and light flavoured jets [64]. Working points are determined from the misidentification probability for light-parton jets to be tagged as a b-jet and are given as 0.244, 0.679 and 0.898 for L,M and T working points respectively.

1018 The b-tagging efficiency is measured in data using several methods applied to multi
 1019 jet events, primarily based on a sample of jets enriched in heavy flavour content. One
 1020 method requires the collection of events with a soft muon within a cone $\Delta R < 0.4$ around
 1021 the jet axis. Because the semileptonic branching fraction of b hadrons is significantly
 1022 larger than that for other hadrons, these jets are more likely to arise from b quarks than
 1023 from another flavour, with the resultant momentum component of the muon transverse
 1024 to the jet axis larger for muons from b-hadron decays than from light or charm jets.

1025 Additionally the performance of the tagger can also be benchmarked in $t\bar{t}$ events where
 1026 in the SM, the top quark is expected to decay to a W boson and a b quark about 99.8%
 1027 of the time [1]. Further selection criteria is applied to these events to further enrich the
 1028 b quark content of these events. The methods to identify b-jets in data are discussed
 1029 in great detail at [65]. The jet flavours are determined in simulation using truth level
 1030 information and are compared to data to determine the correction scale factors (SF_b),
 1031 which are displayed for the CSVM tagger in Figure 3.7.

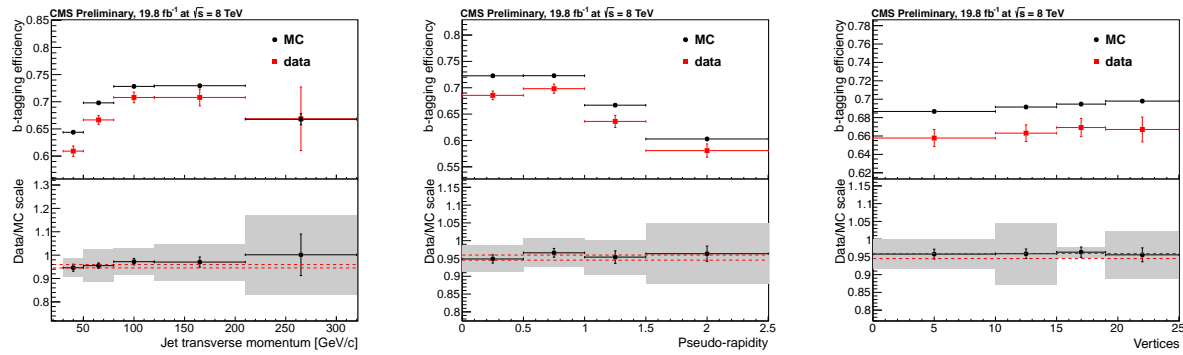


Figure 3.7.: Measured in $t\bar{t} \rightarrow$ di-lepton events using the CSVM tagger: (upper panels) b-tagging efficiencies and (lower panels) data/MC scale factor SF_b as a function of (left) jet p_T , (middle) jet $|\eta|$ and (right) number of primary vertices. In the lower panels, the grey filled areas represent the total statistical and systematic uncertainties, whereas the dotted lines are the average SF_b values within statistical uncertainties.

1032 The measurement of the misidentification probability for light-parton jets relies on the
 1033 inversion of tagging algorithms, selecting non-b jets using the same variables and tech-
 1034 niques used in benchmarking the b-tagging efficiency. The scale factors (SF_s) to be
 1035 applied to MC are shown in Figure 3.8 for the CSVM tagger.

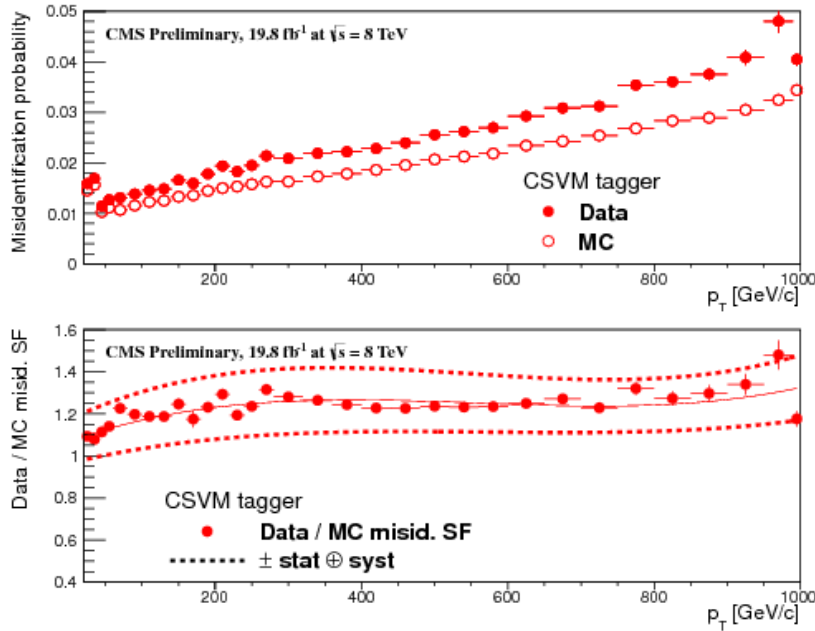


Figure 3.8.: For the **CSVM** tagging criterion: (top) misidentification probability in data (filled circles) and simulation (open circles); (bottom) scale factor for the misidentification probability. The last p_T bin in each plot includes all jets with $p_T > 1000$ GeV. The solid curve is the result of a polynomial fit to the data points. The dashed curves represent the overall statistical and systematic uncertainties on the measurements.

1036 3.4. Triggering System

1037 With bunch crossings separated by just 25 ns, the rate at which data from all collisions
 1038 would have to be written out and processed would be unfeasible. A two-tiered triggering
 1039 system is applied at **CMS** in order to cope with the high collision rate of protons. The
 1040 **CMS** trigger is designed to use limited information from each event to determine whether
 1041 to record the event, reducing the rate of data taking to manageable levels whilst ensuring
 1042 a high efficiency of interesting physics object events are selected.

1043 The **L1** is a pipelined, dead-timeless system based on custom-built electronics [66], and is
 1044 a combination of several sub systems which is shown pictorially in Figure 3.9. The L1
 1045 system is covered in more detail within the following section along with a description
 1046 of the service work undertaken by the author to benchmark the performance of the L1
 1047 calorimeter trigger during the 2012 8 TeV run period.

1048 The Higher Level Trigger (**HLT**) is a large farm of commercial computers [67]. The **HLT**
 1049 processes events with software reconstruction algorithms that are more detailed, giving
 1050 performance more similar to the reconstruction used offline. The **HLT** reduces the event

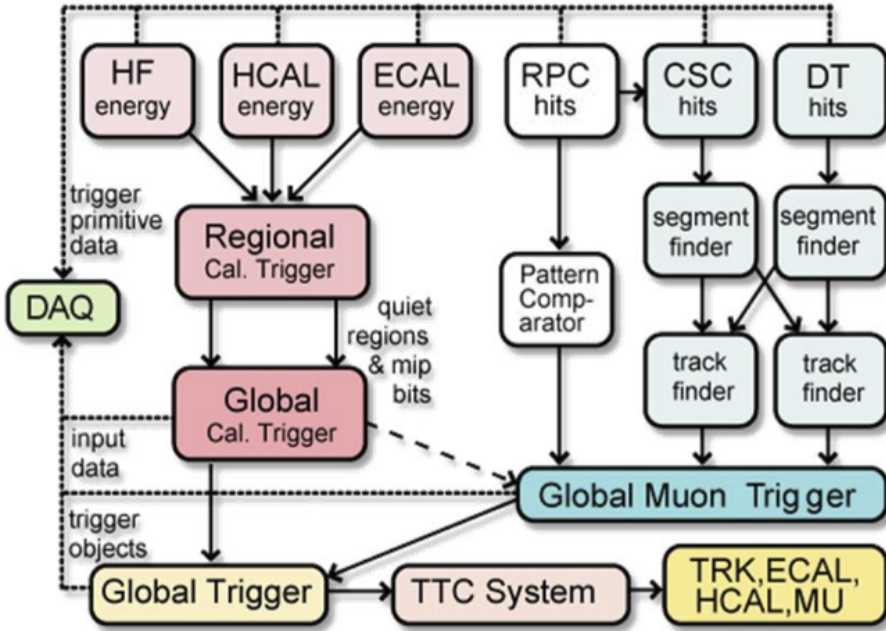


Figure 3.9.: The CMS L1 Trigger system.

1051 rate written to disk by a factor of ~ 500 ($\sim 200\text{Hz}$). The recorded events are transferred
 1052 from CMS to the CERN computing centre, where event reconstruction is performed, and
 1053 then distributed to CMS computing sites around the globe for storage and analysis.

1054 3.4.1. The level-1 trigger

1055 The L1 trigger reduces the rate of events collected from 40 MHz to $\sim 100\text{ kHz}$ using
 1056 information from the calorimeters and muon chambers, but not the tracker. A tree
 1057 system of triggers is used to decide whether to pass on an event to the HLT for further
 1058 reconstruction. Firstly the calorimeter and muon event information is kept separate,
 1059 with local reconstruction of objects ($\mu, e, \gamma, \text{jets}$) performed by the Regional Calorimeter
 1060 Trigger (RCT) and Regional Muon Trigger (RMT) respectively. The RCT generates up to
 1061 72 isolated and non-isolated electromagnetic objects. These are sorted by rank, which is
 1062 equivalent to transverse energy E_T , with the four highest ranked electromagnetic objects
 1063 being passed via the Global Calorimeter Trigger (GCT) and Global MuonTrigger (GMT)
 1064 to the Global Trigger (GT).

1065 In the L1 **GCT**, coarse measurements of the energy deposited in the electromagnetic and
1066 hadronic calorimeters are combined and by using sophisticated algorithms the following
1067 physics objects are formed:

- 1068 • isolated and non-isolated electromagnetic objects (e and γ);
- 1069 • hadronic jets in the central and forward sections of the hadronic calorimeters;
- 1070 • hadronically decaying tau leptons;
- 1071 • total transverse energy (E_T), the scalar sum of the energy measured at L1, and
1072 missing transverse energy (\cancel{E}_T), defined as the vector sum of the energy of L1
1073 objects;
- 1074 • total transverse jet energy (H_T), the scalar sum of the energy of all L1 jet objects,
1075 and missing transverse jet energy (\cancel{H}_T), defined as the vector sum of the energy of
1076 L1 jets, are calculated from uncorrected L1 jets.

1077 In addition quantities suitable for triggering minimum bias events, forward physics and
1078 beam background events are calculated. Additionally relevant muon isolation information
1079 is also passed on to the **GMT** for decisions involving the muon triggers where it is
1080 combined with information from across the three muon sub-systems. The resultant final
1081 accept/reject decision at **L1** is then performed by the **GT** based on the objects received
1082 from the **GCT** and **GMT** (e/γ , μ , jets, E_T , \cancel{E}_T , H_T).

1083 The L1 trigger is therefore of upmost importance to the functioning of the detector.
1084 Without a high-performing trigger and a good understanding of its performance, there
1085 would be no data to analyse. Observations of how the L1 trigger performance is affected
1086 by changing **LHC** running conditions over the 2012 run period and also the introduction
1087 of a jet seed threshold to the L1 jet trigger algorithm is presented in the following Sections
1088 (3.4.2 - 3.4.6).

1089 3.4.2. The L1 trigger jet algorithm

1090 The L1 jet trigger uses the transverse energy sums computed in the calorimeter (both
1091 hadronic and electromagnetic) trigger regions. Each region consists of 4×4 trigger tower
1092 windows, spanning a region of $\Delta\eta \times \Delta\phi = 0.087 \times 0.087$ in pseudorapidity-azimuth. The
1093 jet trigger uses a 3×3 calorimeter region (112 trigger towers) sliding window technique
1094 which spans the full (η, ϕ) coverage of the **CMS** calorimeter as shown in Figure 3.10.

1095 In forming a L1 jet is it required that the central region to be higher than the eight
1096 neighbouring regions $E_{T\text{central}} > E_{T\text{surround}}$. Additionally a minimum threshold of 5 GeV
1097 on $E_{T\text{central}}$ was introduced during the 2012 run period to suppress noise from pile-up,
1098 the effects of which are shown in Section (3.4.4).

1099 The L1 jets are characterised by the E_T , summed over the 3×3 calorimeter regions,
1100 which corresponds to 12×12 trigger towers in barrel and endcap or 3×3 larger **HF**
1101 towers in the **HF**. The ϕ size of the jet window is the same everywhere, whilst the η
1102 binning gets somewhat larger at high η due to calorimeter and trigger tower segmentation.
1103 The jets are labelled by (η, ϕ) indexes of the central calorimeter region.

1104 Jets with $|\eta| > 3.0$ are classified as forward jets, whereas those with $|\eta| < 3.0$ are classified
1105 as central. The four highest energy central, forward and τ jets in the calorimeter are
1106 passed through Look Up Table (**LUT**)’s, which apply a programmable η –dependent jet
1107 energy scale correction. These are then used to make L1 trigger decisions.

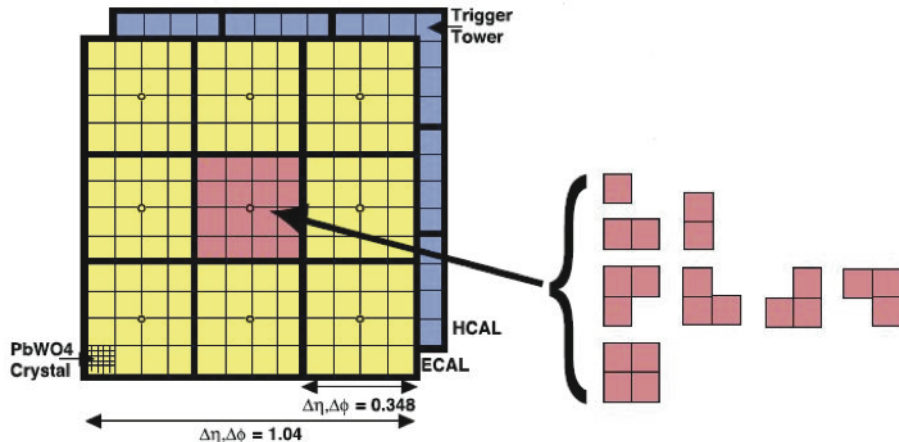


Figure 3.10.: Illustration of the Level-1 jet finding algorithm.

1108 The performance of the L1 jets is evaluated with respect to offline jets, which are taken
1109 from the standard Calo jet and the PF jet reconstruction algorithms of **CMS**. Jets are
1110 corrected for pile-up and detector effects as described in 3.3.1. A moderate level of noise
1111 rejection is applied to the offline jets by selecting jets passing the “loose identification
1112 criteria for both Calo and PF. These criteria are summarised in Appendix (A).

¹¹¹³ 3.4.3. Measuring L1 jet trigger efficiencies

¹¹¹⁴ The L1 jet efficiency is defined as the fraction of leading offline jets which were matched
¹¹¹⁵ with a L1 tau or central jet above a certain trigger threshold, divided by all the leading
¹¹¹⁶ offline jets in the event. This quantity is then plotted as a function of the offline jet E_T ,
¹¹¹⁷ η and ϕ .

¹¹¹⁸ The efficiency is determined by matching the L1 and reconstructed offline jets spatially
¹¹¹⁹ in $\eta - \phi$ space. This is done by calculating the minimum separation in ΔR between the
¹¹²⁰ highest offline reconstructed jet in E_T ($E_T > 10$ GeV, $|\eta| < 3$) and any L1 jet. A jet will
¹¹²¹ be matched if this value is found to be < 0.5 . Should more than one jet satisfy this, the
¹¹²² jet closest in ΔR is taken as the matched jet. The matching efficiency is close to 100%,
¹¹²³ above 30(45) GeV for run 2012B(C) data (see Appendix B.1).

¹¹²⁴ Each efficiency curve is fitted with a function which is the cumulative distribution function
¹¹²⁵ of an Exponentially Modified Gaussian (EMG) distribution:

$$\text{f}(x; \mu, \sigma, \lambda) = \frac{\lambda}{2} \cdot e^{\frac{\lambda}{2}(2\mu + \lambda\sigma^2 - 2x)} \cdot \text{erfc}\left(\frac{\mu + \lambda\sigma^2 - x}{\sqrt{2}\sigma}\right) \quad (3.3)$$

where erfc is the complementary error function defined as:

$$\text{erfc}(x) = 1 - \text{erf}(x) = \frac{2}{\sqrt{\pi}} \int_x^\infty e^{-t^2} dt.$$

¹¹²⁷ In this functional form, the parameter μ determines the point of 50% of the plateau
¹¹²⁸ efficiency and the σ gives the resolution. This parametrisation is used to benchmark
¹¹²⁹ the efficiency at the plateau, the turn-on points and resolution for each L1 Jet trigger.
¹¹³⁰ The choice of function is purely empirical. Previous studies used the error function
¹¹³¹ alone, which described the data well at high threshold values but could not describe the
¹¹³² efficiencies well at lower thresholds [68].

¹¹³³ The efficiency turn-on curves for various L1 jet thresholds are evaluated as a function of
¹¹³⁴ the offline reconstructed jet E_T for central jets with $|\eta| < 3$. These are measured using
¹¹³⁵ single isolated μ triggers which have high statistics, and are orthogonal and therefore
¹¹³⁶ unbiased to the hadronic triggers under study. The efficiency is calculated with respect to
¹¹³⁷ offline Calo and PF Jets in Figure 3.11. Table 3.1 shows the values of these parameters,
¹¹³⁸ calculated for three example L1 single jet triggers taken from 2012 8 TeV data.

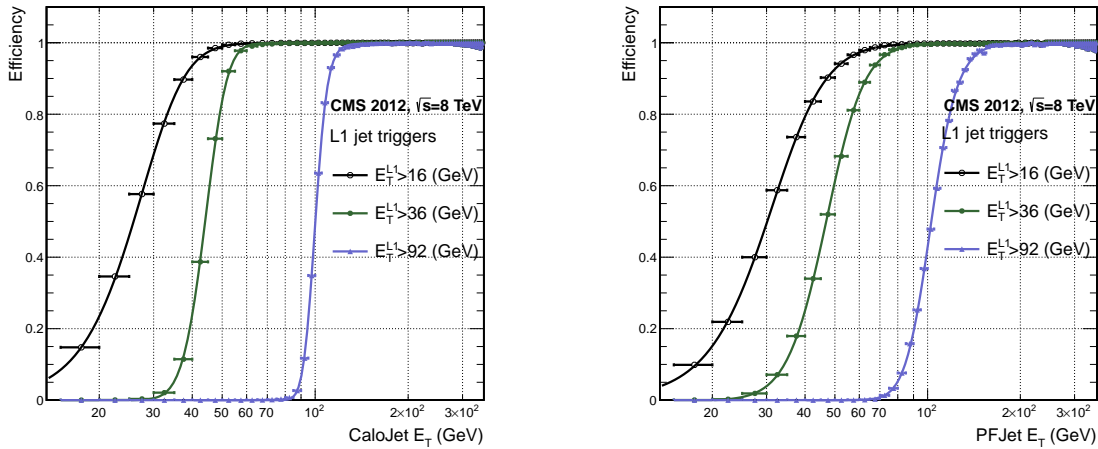


Figure 3.11.: L1 jet efficiency turn-on curves as a function of the offline CaloJet E_T (left) and PFJet E_T (right), measured in 2012 Run Period C data and collected with an isolated single μ data sample.

Trigger	Calo		PF	
	μ	σ	μ	σ
L1_SingleJet16	21.09 ± 0.03	7.01 ± 0.02	22.17 ± 0.04	7.83 ± 0.03
L1_SingleJet36	41.15 ± 0.05	5.11 ± 0.02	39.16 ± 0.06	8.04 ± 0.03
L1_SingleJet92	95.36 ± 0.13	5.62 ± 0.03	90.85 ± 0.19	11.30 ± 0.10

Table 3.1.: Results of a cumulative [EMG](#) function fit to the turn-on curves for L1 single jet triggers in run 2012 Run Period C, measured in an isolated μ data sample. The turn-on point, μ , and resolution, σ , of the L1 jet triggers are measured with respect to offline Calo Jets (left) and PF Jets (right).

The results from the L1 single jet triggers shows good performance for both Calo and PF jets. A better resolution for Calo jets with respect to L1 jets quantities is observed. This effect is due to Calo jet reconstruction using the same detector systems as in L1 jets, whereas with PF jet construction using tracker and muon information, a more smeared resolution when compared to L1 is expected.

3.4.4. Effects of the L1 jet seed

Between run period B and C of the 2012 data taking period, a jet seed threshold was introduced into the L1 trigger jet algorithm. There was previously no direct requirement made on the energy deposited in the central region. The introduction of a jet seed threshold required that the central region have $E_T \geq 5\text{GeV}$, and was introduced to

1149 counteract the effects of high pile up running conditions which create a large number of
1150 soft non-collimated jets, that are then added to the jets from the primary interaction or
1151 other soft jets from other secondary interactions [69]. This in turn causes a large increase
1152 in trigger rate due to the increase in the likelihood that the event causes the L1 trigger to
1153 fire. This was implemented to maintain trigger thresholds by cutting the rate of events
1154 recorded without significant reduction in the efficiency of physics events of interest.

1155 The effect of the introduction of this jet seed threshold between these two run periods is
1156 benchmarked through a comparison of the efficiency of the L1 jet triggers with respect
1157 to offline Calo jets shown in Figure 3.12, and the L1 H_T trigger efficiency in Figure 3.14
1158 which is compared to offline H_T constructed from Calo jets with $E_T \geq 40\text{GeV}$.

1159 To negate any effects from different pile-up conditions in the run periods, the efficiencies
1160 are measured in events which contain between 15 and 20 primary vertices as defined in
1161 Appendix (A.2).

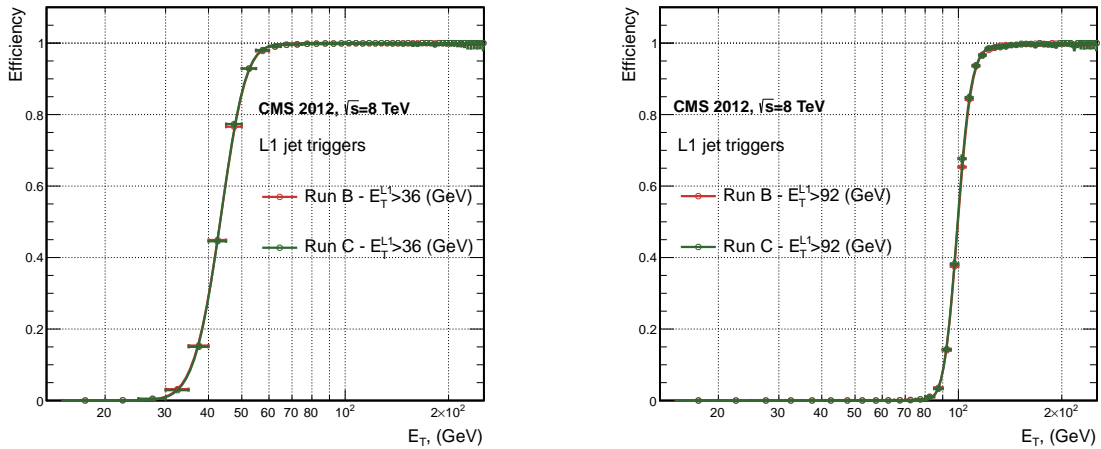


Figure 3.12.: L1 jet efficiency turn-on curves as a function of the offline CaloJet E_T , measured for the L1 SingleJet 36 and 92 trigger in 2012 run period B and C collected with an isolated single μ' sample.

1162 It can be seen that the performance of the $E_T > 36, 92$ single jet are almost identical,
1163 with the jet seed having no measurable effect on these triggers as shown in Table 3.2 .

1164 For the H_T triggers, a large increase in rate during high pile-up conditions is expected.
1165 This is due to the low energy threshold required for a jet to be added to the L1 H_T sum,
1166 which is compiled from all uncorrected L1 jets formed in the RCT. The introduction
1167 of the jet seed threshold removes the creation of many of these soft low E_T jets, thus

Trigger	2012B		2012C	
	μ	σ	μ	σ
L1_SingleJet36	40.29 ± 0.04	5.34 ± 0.02	40.29 ± 0.11	5.21 ± 0.05
L1_SingleJet92	94.99 ± 0.09	5.93 ± 0.06	94.82 ± 0.29	5.74 ± 0.18

Table 3.2.: Results of a cumulative EMG function fit to the turn-on curves for L1 single jet triggers in the 2012 run period B and C, preselected on an isolated muon trigger. The turn-on point μ and resolution σ of the L1 jet triggers are measured with respect to offline Calo Jets in run B (left) and run C (right).

lowering the H_T calculation at L1. The effect on the trigger cross section for L1 H_T 150 trigger can be seen in Figure 3.13.

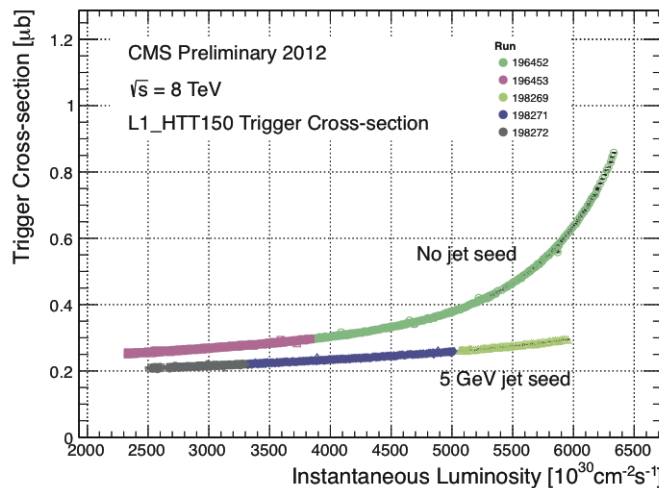


Figure 3.13.: Trigger cross section for the L1HTT150 trigger path. Showing that a 5 GeV jet seed threshold dramatically reduces the dependance of cross section on the instantaneous luminosity for L1 H_T triggers [70].

Different behaviours for the trigger turn ons between these run periods are therefore expected. The turn on point is observed to shift to higher H_T values after the introduction of the jet seed threshold, whilst having a sharper resolution due to less pile-up jets being included the H_T sum. This effect is demonstrated in Table 3.3.

3.4.5. Robustness of L1 jet performance against pile-up

The performance of the L1 single jet triggers is evaluated in different pile-up conditions to benchmark any dependence on pile-up. Three different pile-up bins of 0-10, 10-20 and >20 vertices are defined, reflecting the low, medium and high pile-up running conditions

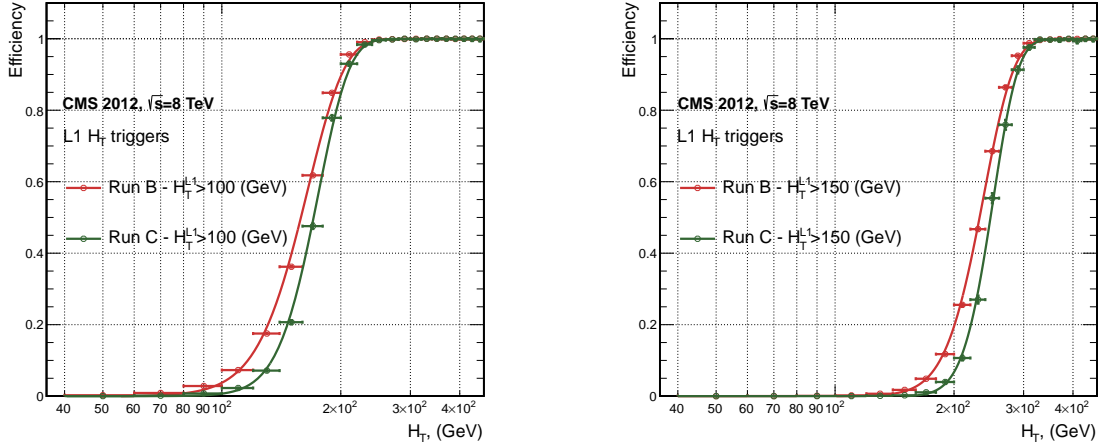


Figure 3.14.: L1 H_T efficiency turn-on curves as a function of the offline CaloJet H_T , measured for the L1 H_T 100 and 150 trigger during the run 2012 B and C collected using an isolated single μ triggered sample.

2012B			2012C		
Trigger	μ	σ	μ	σ	
L1 HT-100	157.5 ± 0.08	32.9 ± 0.08	169.8 ± 0.08	28.7 ± 0.03	
L1 H1-150	230.9 ± 0.02	37.3 ± 0.01	246.4 ± 0.16	31.8 ± 0.05	

Table 3.3.: Results of a cumulative EMG function fit to the turn-on curves for H_T in run 2012 B and C, preselected on an isolated single μ trigger. The turn-on point μ , resolution σ of the L1 H_T triggers are measured with respect to offline H_T formed from CaloJets with a $E_T \geq 40$ in run period B (left) and C (right).

at CMS in 2012. This is benchmarked relative to Calo and PF jets for the run 2012 C period where the jet seed threshold is applied, with L1 single jet thresholds of 16, 36 and 92 GeV, shown in Figure 3.15. The results of fits to these efficiency turn-on curves are given in Table 3.4 and Table 3.5 for Calo and PF jets respectively.

Vertices	0-10		11-20		> 20	
	μ	σ	μ	σ	μ	σ
L1_SingleJet16	19.9 ± 0.1	6.1 ± 0.3	20.8 ± 0.1	6.5 ± 0.1	22.3 ± 0.2	7.5 ± 0.1
L1_SingleJet36	41.8 ± 0.1	4.6 ± 0.1	40.9 ± 0.1	5.1 ± 0.1	40.6 ± 0.6	5.9 ± 0.2
L1_SingleJet92	95.9 ± 0.2	5.4 ± 0.1	95.2 ± 0.2	5.6 ± 0.1	94.5 ± 0.6	6.2 ± 0.3

Table 3.4.: Results of a cumulative EMG function fit to the efficiency turn-on curves for L1 single jet triggers in the 2012 run period C, measured from isolated μ triggered data. The turn-on point, μ , and resolution, σ , of the L1 jet triggers are measured with respect to offline Calo jets in low (left), medium (middle) and high (right) pile-up conditions.

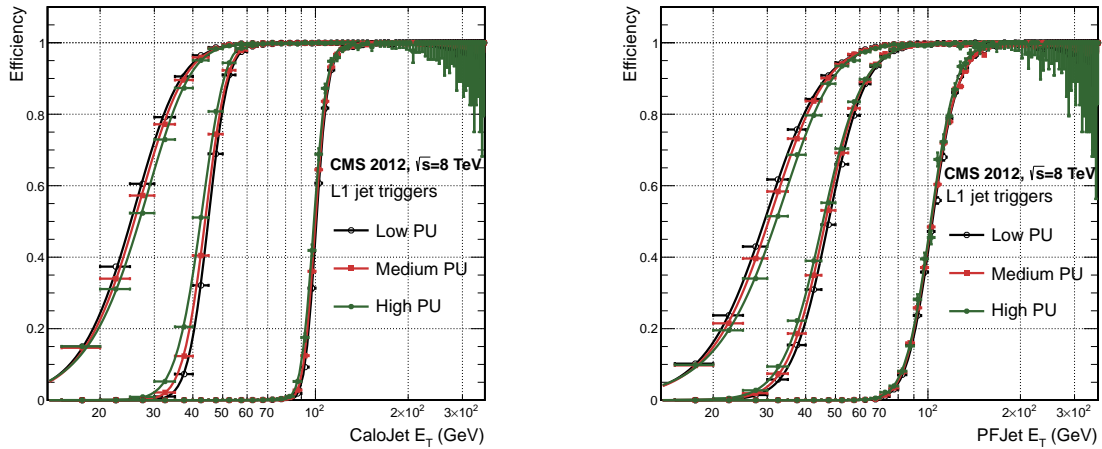


Figure 3.15.: L1 jet efficiency turn-on curves as a function of the leading offline E_T Calo (left) and PF (right) jet, for low, medium and high pile-up conditions.

Vertices	0-10		11-20		> 20	
	μ	σ	μ	σ	μ	σ
L1_SingleJet16	21.1 \pm 0.1	7.16 \pm 0.05	22.34 \pm 0.1	7.9 \pm 0.1	24.6 \pm 0.2	9.5 \pm 0.1
L1_SingleJet36	39.6 \pm 0.1	7.4 \pm 0.1	38.4 \pm 0.1	7.4 \pm 0.1	37.1 \pm 0.2	7.5 \pm 0.1
L1_SingleJet92	91.6 \pm 0.3	11.3 \pm 0.2	90.4 \pm 0.3	11.2 \pm 0.1	92.0 \pm 0.9	12.1 \pm 0.4

Table 3.5.: Results of a cumulative EMG function fit to the efficiency turn-on curves for Level-1 single jet triggers in the 2012 run period C, measured from isolated μ triggered data. The turn-on point, μ , and resolution, σ , of the L1 jet triggers are measured with respect to offline PF jets in low (left), medium (middle) and high (right) pile-up conditions.

1182 No significant drop in efficiency is observed in the presence of a high number of primary
 1183 vertices. The increase in hadronic activity in higher pile-up conditions, combined with
 1184 the absence of pile-up subtraction for L1 jets, results in the expected observation of
 1185 a decrease in the μ value of the efficiency turn-ons as a function of pile-up, while the
 1186 resolution, σ of the turn-ons are found to gradually worsen as expected with increasing
 1187 pile-up.

1188 These features are further emphasised when shown as a function of

$$\frac{(L1 E_T - \text{Offline } E_T)}{\text{Offline } E_T} \quad (3.4)$$

1189 in bins of matched leading offline jet E_T , of which the individual fits can be found in
1190 Appendix (B.2). Each of these distributions are fitted with an **EMG** function as defined
1191 in Equation (3.3).

1192 The μ , σ and λ values extracted for the low, medium and high pile-up conditions are
1193 shown for Calo and PF jets in Figure 3.16 and Figure 3.17 respectively. The central value
1194 of $\frac{(L1 E_T - \text{Offline } E_T)}{\text{Offline } E_T}$ is observed to increases as a function of jet E_T , whilst the resolution
1195 is also observed to improve at higher offline jet E_T .

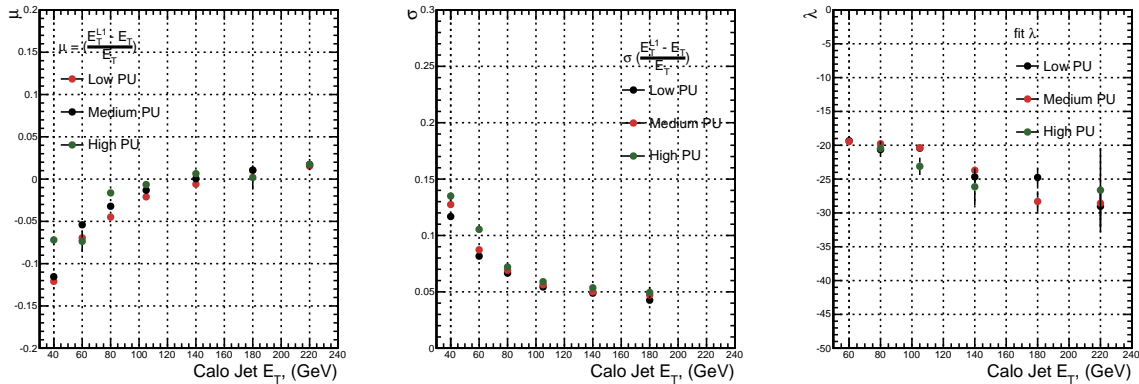


Figure 3.16.: Fit values from an **EMG** function fitted to the resolution plots of leading Calo jet E_T measured as a function of $\frac{(L1 E_T - \text{Offline } E_T)}{\text{Offline } E_T}$ for low, medium and high pile-up conditions. The plots show the mean μ (left), resolution σ (middle) of the Gaussian as well as the decay term λ (right) of the exponential.

1196 The resolution of other L1 energy sum quantities, H_T , \not{E}_T and $\sum E_T$ parameterised as
1197 in Equation (3.4), can be found in Appendix B.3. The same behaviour observed for
1198 the single jet triggers is also found for these quantities, where in the presence of higher
1199 pile-up the μ values are shifted to higher values, with a worsening resolution, σ again
1200 due to the increase in soft pile-up jets and the absence of pile-up subtraction at L1.

1201 3.4.6. Summary

1202 The performance of the CMS Level-1 Trigger has been studied and evaluated for jets and
1203 energy sum quantities using data collected during the 2012 LHC 8TeV run. These studies
1204 include the effect of introduction of a 5 GeV jet seed threshold into the jet algorithm
1205 configuration, the purpose of which is to mitigate the effects of pile-up on the rate of
1206 L1 triggers whilst not adversely affecting the efficiency of these triggers. No significant

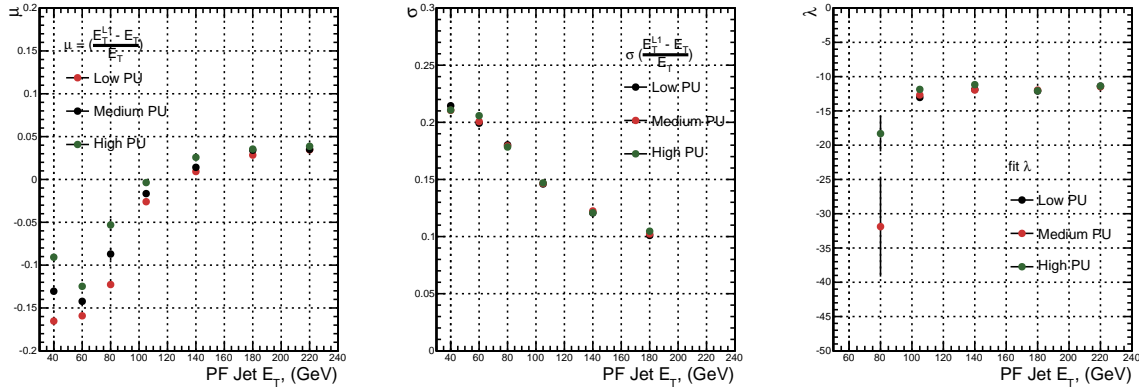


Figure 3.17.: Fit values from an **EMG** function fitted to the resolution plots of leading PF jet E_T measured as a function of $\frac{(L1 E_T - \text{Offline } E_T)}{\text{Offline } E_T}$ for low and medium pile-up conditions. The plots show the mean μ (left), resolution σ (middle) of the Gaussian as well as the decay term λ (right) of the exponential.

1207 change in performance is observed with this change and good performance is observed
 1208 for a range of L1 quantities.

Chapter 4.

1209 SUSY Searches In Hadronic Final 1210 States

1211 In this chapter a model independent search for **SUSY** in hadronic final states with \cancel{E}_T
1212 using the α_T variable and b-quark multiplicity is introduced and described in detail. The
1213 results presented are based on a data sample of pp collisions collected in 2012 at $\sqrt{s} = 8$
1214 TeV, corresponding to an integrate luminosity of $11.7 \pm 0.5 \text{ fb}^{-1}$.

1215 The kinematic variable α_T is motivated as a variable to provide strong rejections of QCD
1216 backgrounds, whilst maintaining sensitivity to a possible **SUSY** signal within Section
1217 (4.1). The search and trigger strategy in addition to the event reconstruction and selection
1218 are outlined within Sections (4.2-4.3).

1219 The method in which the **SM** background is estimated using an analytical technique to
1220 improve statistical precision at higher b-tag multiplicities is detailed within Section (4.5),
1221 with a discussion on the impact of b-tagging and mis-tagging scale factors between data
1222 and MC on any background predictions.

1223 A description of the formulation of appropriate systematic uncertainties applied to the
1224 background predictions to account for theoretical uncertainties and limitations in the
1225 simulation modelling of event kinematics and instrumental effects is covered in Section
1226 (4.6).

1227 Finally the statistical likelihood model to interpret the observations in the signal and
1228 control samples is described in Section (4.8). The experimental reach of the analysis
1229 discussed within this thesis is interpreted in two classes of **SMS** models, the topologies
1230 of which are detailed in Section (2.4.1). The **SMS** models considered in this analysis

1231 are summarised in Table 4.1. For each model, the **LSP** is assumed to be the lightest
1232 neutralino.

1233 Within the table are also defined reference points, parameterised in terms of parent
1234 gluino/squark and **LSP** sparticle masses, m_{parent} and m_{LSP} , respectively, which are used
1235 within the following two chapters to demonstrate potential yields within the signal region
1236 of the search. The masses are chosen to reflect parameter space which is within the
1237 expected sensitivity reach of the search.

Model	Production/decay mode	Reference model	
		m_{parent}	m_{LSP}
G1 (T1)	$pp \rightarrow \tilde{g}\tilde{g}^* \rightarrow q\bar{q}\tilde{\chi}_1^0 q\bar{q}\tilde{\chi}_1^0$	700	300
G2 (T1bbbb)	$pp \rightarrow \tilde{g}\tilde{g}^* \rightarrow b\bar{b}\tilde{\chi}_1^0 b\bar{b}\tilde{\chi}_1^0$	900	500
G3 (T1tttt)	$pp \rightarrow \tilde{g}\tilde{g}^* \rightarrow t\bar{t}\tilde{\chi}_1^0 t\bar{t}\tilde{\chi}_1^0$	850	250
D1 (T2)	$pp \rightarrow \tilde{q}\tilde{q}^* \rightarrow q\tilde{\chi}_1^0 \bar{q}\tilde{\chi}_1^0$	600	250
D2 (T2bb)	$pp \rightarrow \tilde{b}\tilde{b}^* \rightarrow b\tilde{\chi}_1^0 \bar{b}\tilde{\chi}_1^0$	500	150
D3 (T2tt)	$pp \rightarrow \tilde{t}\tilde{t}^* \rightarrow t\tilde{\chi}_1^0 \bar{t}\tilde{\chi}_1^0$	400	0

Table 4.1.: A summary of the **SMS** models interpreted in this analysis, involving both direct (D) and gluino-induced (G) production of squarks and their decays. Reference models are also defined in terms of parent and **LSP** sparticle mass

1238 4.1. An Introduction to the α_T Search

1239 The experimental signature of **SUSY** signal in the hadronic channel would manifest
1240 itself as a final state containing energetic jets and \cancel{E}_T . The search focuses on topologies
1241 where new heavy supersymmetric, R-parity conserving particles are pair-produced in pp
1242 collisions. These particles decaying to a **LSP** escape the detector undetected, leading to
1243 significant missing energy and missing hadronic transverse energy,

$$\mathcal{H}_T = \left| \sum_{i=1}^n p_T^{jet_i} \right|, \quad (4.1)$$

1244 defined as the vector sum of the transverse energies of jets selected in an event. Energetic
1245 jets produced in the decay of these supersymmetric particles also can produce significant
1246 visible transverse energy,

$$H_T = \sum_{i=1}^n E_T^{jet_i}, \quad (4.2)$$

1247 defined as the scalar sum of the transverse energies of jets selected in an event.

1248 A search within this channel is greatly complicated in a hadron collider environment,
1249 where the overwhelming background comes from inherently balanced multi-jet (“QCD”)
1250 events which are produced with an extremely large cross section as demonstrated within
1251 Figure 4.1. \cancel{E}_T can appear in such events with a substantial mis-measurement of jet
1252 energy or missed objects due to detector miscalibration or noise effects.

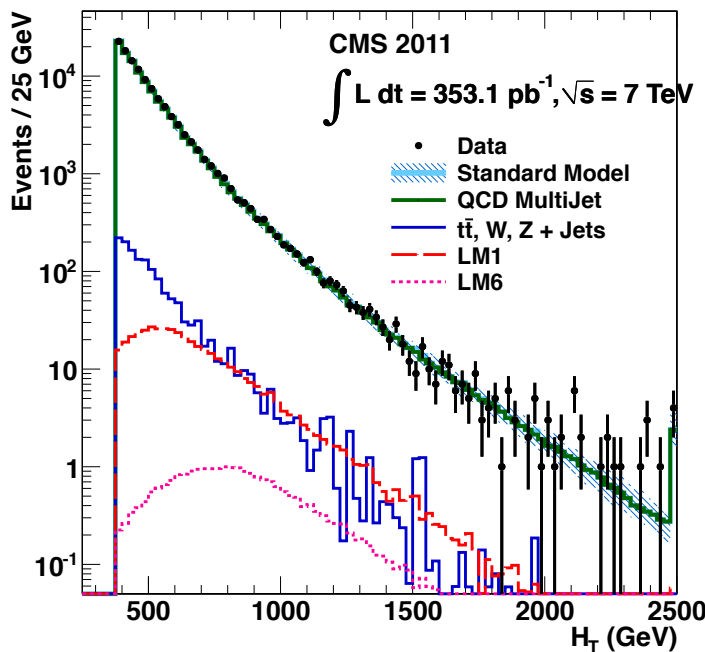


Figure 4.1.: Reconstructed offline H_T for 11.7fb^{-1} of data after a basic pre-selection. Sample is collected from prescaled H_T triggers. Overlaid are expectations from MC simulation of EWK processes as well as a reference signal model (labelled D2 from Table 4.1).

1253 Additional SM background from EWK processes with genuine \cancel{E}_T from escaping neutrinos
1254 comprise the irreducible background within this search and come mainly from:

1255 • $Z \rightarrow \nu\bar{\nu} + \text{jets}$,

- $W \rightarrow l\nu + \text{jets}$ in which a lepton falls outside of detector acceptance, or the lepton decays hadronically $\tau \rightarrow \text{had}$,
- $t\bar{t}$ with at least one leptonic W decay,
- small background contributions from DY, single top and Diboson (WW,ZZ,WZ) processes.

The search is designed to have a strong separation between events with genuine and “fake” \cancel{E}_T which is achieved primarily through the dimensionless kinematic variable, α_T [71][72].

4.1.1. The α_T variable

For a perfectly measured di-jet QCD event, conservation laws dictate that they must be produced back-to-back and of equal magnitude. However in di-jet events with real \cancel{E}_T , both of these jets are produced independently of one another, depicted in Figure 4.2.

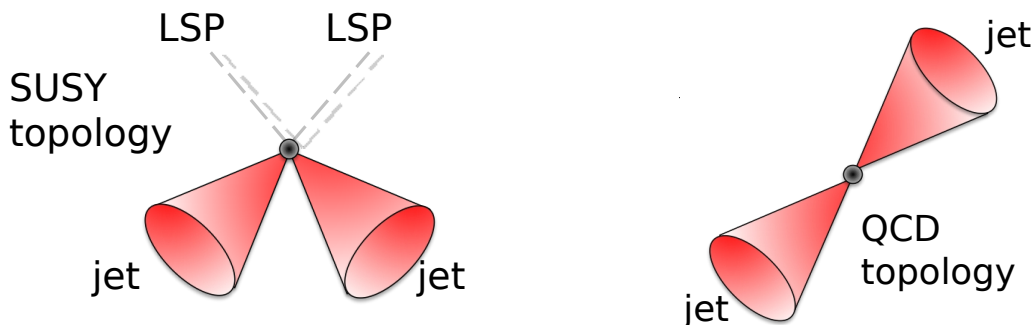


Figure 4.2.: The event topologies of background QCD di-jet events (right) and a generic SUSY signature with genuine \cancel{E}_T (left).

Exploiting this feature leads to the formulation of α_T in di-jet systems defined as,

$$\alpha_T = \frac{E_T^{j2}}{M_T}, \quad (4.3)$$

where E_T^{j2} is the transverse energy of the least energetic of the two jets and M_T defined as:

$$M_T = \sqrt{\left(\sum_{i=1}^2 E_T^{j_i}\right)^2 - \left(\sum_{i=1}^2 p_x^{j_i}\right)^2 - \left(\sum_{i=1}^2 p_y^{j_i}\right)^2} \equiv \sqrt{H_T^2 - \cancel{H}_T^2}. \quad (4.4)$$

1271 A perfectly balanced di-jet event i.e. $E_T^{j_1} = E_T^{j_2}$ would give an $\alpha_T = 0.5$, whereas events
1272 with jets which are not back-to-back, for example in events in which a W or Z recoils off
1273 a system of jets, α_T can achieve values in excess of 0.5.

1274 α_T can be extended to apply to any arbitrary number of jets, undertaken by modelling a
1275 system of n jets as a di-jet system, through the formation of two pseudo-jets [73]. The two
1276 pseudo-jets are built by merging the jets present in the event such that the 2 pseudo-jets
1277 are chosen to be as balanced as possible, i.e the $\Delta H_T \equiv |E_T^{pj_1} - E_T^{pj_2}|$ is minimised
1278 between the two pseudo jets. Using Equation (4.4), α_T can be rewritten as,

$$\alpha_T = \frac{1}{2} \frac{H_T - \Delta H_T}{\sqrt{H_T^2 - \cancel{H}_T^2}} = \frac{1}{2} \frac{1 - \Delta H_T/H_T}{\sqrt{1 - (\cancel{H}_T/H_T)^2}}. \quad (4.5)$$

1279 The distribution of α_T for the two jet categories used within this analysis, 2,3 and ≥ 4 jets,
1280 is shown in the Figure 4.3, demonstrating the ability of the α_T variable to discriminate
1281 between multi jet events and EWK processes with genuine \cancel{E}_T in the final state.

1282 The α_T requirement used within the search is chosen to be $\alpha_T > 0.55$ to ensure that
1283 the QCD multijet background is negligible even in the presence of moderate jet mis-
1284 measurement. There still remains other effects which can cause multijet events to
1285 artificially have a large α_T value, which are discussed in detail in Section (4.2.2).

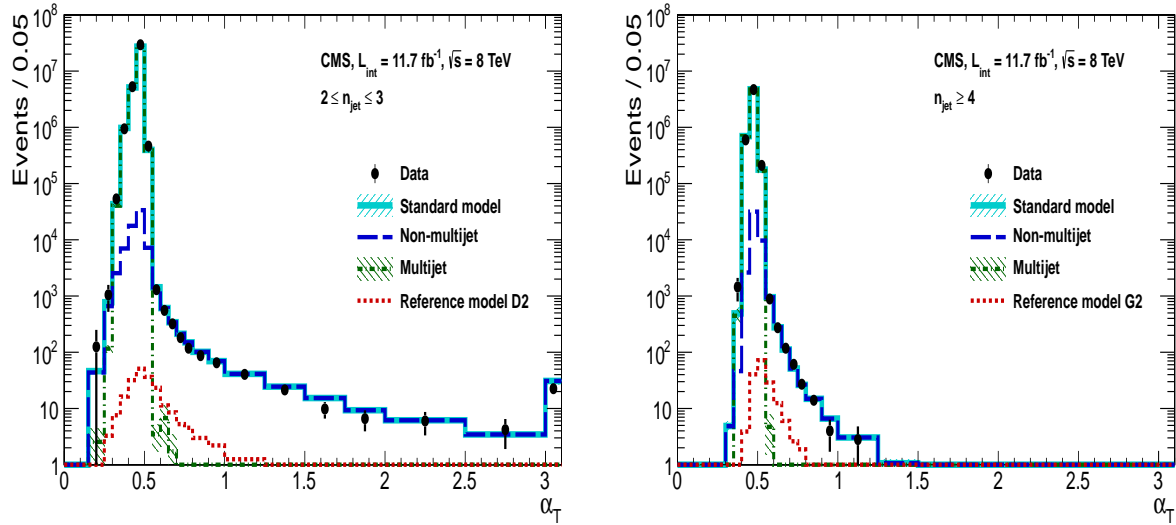


Figure 4.3.: The α_T distributions for the low 2-3 (left) and high ≥ 4 (right) jet multiplicities after a full analysis selection and shown for $H_T > 375$. Data is collected using both prescaled H_T triggers and dedicated α_T triggers for below and above $\alpha_T = 0.55$ respectively. . Expected yields as given by simulation are also shown for multijet events (green dash-dotted line), EWK backgrounds with genuine \cancel{E}_T (blue long-dashed line), the sum of all SM processes (cyan solid line) and the reference signal model D2 (left, red dotted line) or G2 (right, red dotted line).

1286 4.2. Search Strategy

1287 The aim of the analysis presented in this thesis is to identify an excess of events in data
1288 over the SM background expectation in multi-jet final states and significant \cancel{E}_T . The
1289 essential suppression of the dominant QCD background for such a search is addressed by
1290 the α_T variable described in the previous section. For estimation of the remaining EWK
1291 backgrounds, three independent data control samples are used to predict the different
1292 processes that compose the background :

- 1293 • $\mu +$ jets to determine $W +$ jets, $t\bar{t}$ and single top backgrounds,
- 1294 • $\gamma +$ jets to determine the irreducible $Z \rightarrow \nu\bar{\nu} +$ jets background,
- 1295 • $\mu\mu +$ jets to determine the irreducible $Z \rightarrow \nu\bar{\nu} +$ jets background.

1296 These control samples are chosen to both be rich in specific EWK processes, be free of
1297 QCD multi-jet events and to also be kinematically similar to the hadronic signal region
1298 that they are estimating the backgrounds of, see Section (4.2.3).

1299 To remain inclusive to a large range of possible **SUSY** models, the signal region is binned
1300 in the following categories to allow for increased sensitivity in the interpretation of results
1301 for different **SUSY** topologies:

1302 **Sensitivity to a range of SUSY mass splittings**

1303 The hadronic signal region is defined by $H_T > 275$, divided into eight bins in H_T .

- 1304 – Two bins of width 50 GeV in the range $275 < H_T < 375$ GeV,
1305 – five bins of width 100 GeV in the range $375 < H_T < 875$ GeV,
1306 – and a final open bin, $H_T > 875$ GeV.

1307 The choice at low H_T is driven primarily by trigger constraints. The mass difference
1308 between the **LSP** and the particle that it decays from is an important factor in the
1309 amount of hadronic activity in the event.

1310 A large mass splitting will lead to hard high p_T jets which contribute to the H_T
1311 sum. From Figure 4.1 it can be seen that the **SM** background falls sharply at high
1312 H_T values, therefore a large number of H_T bins will lead to easier identification
1313 of such signals. Conversely smaller mass splittings lead to softer jet p_T 's which will
1314 subsequently fall into the lower H_T range.

1315 **Sensitivity to production method of SUSY particles**

1316 The production mechanism of any potential **SUSY** signal can lead to different event
1317 topologies. One such way to discriminate between gluino ($g\tilde{g}$ - “high multiplicity”),
1318 and direct squark ($q\tilde{q}$ - “low multiplicity”) induced production of **SUSY** particles is
1319 realised through the number of reconstructed jets in the final state.

1320 The analysis is thus split into two jet categories : 2-3 jets , ≥ 4 jets to give sensitivity
1321 to both of these mechanisms.

1322 **Sensitivity to “Natural SUSY” via tagging jets from b-quarks**

1323 Jets originating from bottom quarks (b-jets) are identified through vertices that
1324 are displaced with respect to the primary interaction. The algorithm used to tag
1325 b-jets is the Combined Secondary Vertex Medium Working Point (**CSV**) tagger,
1326 described within Section (3.3.2). A cut is placed on the discriminator variable of
1327 > 0.679 , leading to a gluon/light-quark mis-tag rate of 1% and a jet p_T dependant
1328 b-tagging efficiency of 60-70% [64].

Natural SUSY models would be characterised through final-state signatures rich in bottom quarks. A search relying on methods to identify jets originating from bottom quarks through b-tagging, will significantly improve the sensitivity to this class of signature.

This is achieved via the binning of events in the signal region according to the number of b-tagged jets reconstructed in each event, in the following: 0,1,2,3, ≥ 4 b-tag categories . In the highest ≥ 4 b-tag category due to a limited number of expected signal and background, just three H_T bins are employed: 275-325 GeV, 325-375 GeV, ≥ 375 GeV.

This characterisation is identically mirrored in all control samples, with the information from all samples and b-tag categories used simultaneously in the likelihood model, see Section (4.8), in order to interpret the results in a coherent and powerful way.

The combination of the H_T , jet multiplicity and b-tag categorisation of the signal region as described above, resultantly leads to 67 different bins in which the analysis is interpreted in, which is depicted in Figure 4.4.

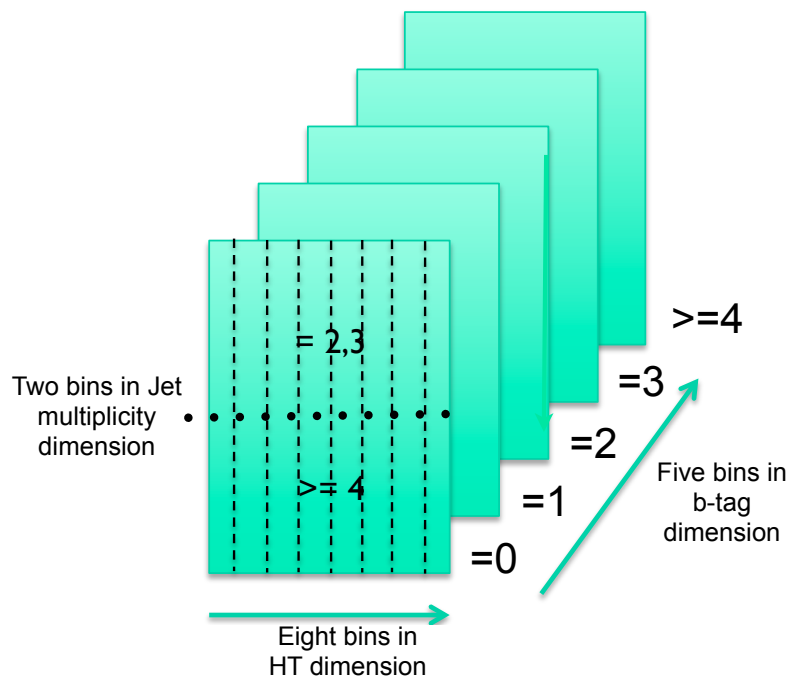


Figure 4.4.: Pictorial depiction of the analysis strategy employed by the α_T search to increase sensitivity to a wide spectra of SUSY models.

1345 **4.2.1. Physics objects**

1346 The physics objects used in the analysis defined below, follow the recommendation of
1347 the various CMS Physics Object Groups ([POGs](#)).

1348 **• Jets**

1349 The jets used in this analysis are CaloJets, reconstructed as described in Section
1350 ([3.3.1](#)) using the anti- k_T jet clustering algorithm.

1351 To ensure the jet object falls within the calorimeter systems a pseudo-rapidity
1352 requirement of $|\eta| < 3$ is applied. Each jet must pass a “loose” identification criteria
1353 to reject jets resulting from unphysical energy, the criteria of which are detailed in
1354 Table A.1 of Appendix A [[74](#)].

1355 **• Muons**

1356 Muons are selected in the $\mu + \text{jets}$ and $\mu\mu + \text{jets}$ control samples, and vetoed in
1357 the signal region. The same cut based identification criteria is applied to muons in
1358 both search regions and is summarised in Table 4.2 [[75](#)].

Categories	Criteria
Global Muon	True
PFMuon	True
χ^2	< 10
Muon chamber hits	> 0
Muon station hits	> 1
Transvere impact d_{xy}	< 0.2mm
Longitudinal distance d_z	< 0.5mm
Pixel hits	> 0
Track layer hits	> 5
PF Isolation (DeltaB corrected)	<0.12

Table 4.2.: Muon Identification criteria used within the analysis for selection/veto purposes in the muon control/signal selections.

1359 Additionally muons are required to be within the acceptance of the muon tracking
1360 systems. For the muon control samples, trigger requirements necessitate a $|\eta| <$
1361 2.1 for the selection of muons. In the signal region where muons are vetoed these
1362 conditions are relaxed to $|\eta| < 2.5$ and a minimum threshold of $p_T > 10$ GeV is
1363 required of muon objects.

1364 **• Photons**

¹³⁶⁵ Photons are selected within the $\gamma + \text{jets}$ control sample and vetoed in all other
¹³⁶⁶ selections. Photons are identified in both cases according to the cut based criteria
¹³⁶⁷ listed in Table 4.3 [76].

Variable	Definition
$H/E < 0.05$	The ratio of hadronic energy in the HCAL tower directly behind the ECAL super-cluster and the ECAL super-cluster itself.
$\sigma_{in\eta} < 0.011$	The log energy weighted width (σ), of the extent of the shower in the η dimension.
$R9 < 1.0$	The ratio of the energy of the 3×3 crystal core of the super-cluster compared to the total energy stored in the 5×5 super-cluster.
Combined Isolation < 6 GeV	The photons are required to be isolated with no electromagnetic or hadronic activity within a radius $\Delta R = 0.3$ of the photon object. A combination of the pileup subtracted [77], ECAL , HCAL and tracking isolation sums are used to determine the combined total isolation value.

Table 4.3.: Photon Identification criteria used within the analysis for selection/veto purposes in the $\gamma + \text{jets}$ control/signal selections.

¹³⁶⁸ Photon objects are also required to have a minimum momentum of $p_T > 25$ GeV.

• Electrons

¹³⁷⁰ Electron identification is defined for veto purposes. They are selected according to
¹³⁷¹ the following cut-based criteria listed in Table 4.4, utilising PF-based isolation.

Categories	Barrel	EndCap
$\Delta\eta_{In}$	0.007	0.009
$\Delta\phi_{In}$	0.15	0.10
$\sigma_{in\eta}$	0.01	0.03
H/E	0.12	0.10
$d0$ (vtx)	0.02	0.02
dZ (vtx)	0.20	0.20
$ (1/E_{ECAL} - 1/p_{track}) $	0.05	0.05
PF Combined isolation/ p_T	0.15	0.15
Vertex fit probability	10^{-6}	10^{-6}

Table 4.4.: Electron Identification criteria used within the analysis for veto purposes.

¹³⁷² Electrons are required to be identified at $|\eta| < 2.5$, with a minimum $p_T > 10$ GeV
¹³⁷³ threshold to ensure that the electron falls within the tracking system of the detector.

• Noise and E_T Filters

1375 A series of Noise filters are applied to veto events which contain spurious non-physical
1376 jets that are not picked up by the jet id, and events which give large unphysical \cancel{E}_T
1377 values. These filters are listed within Table A.3 of Appendix A.

1378 4.2.2. Event selection

1379 The selection criteria for events within the analysis are detailed below. A set of common
1380 cuts are applied to both signal (maximise acceptance to a range of SUSY signatures), and
1381 control samples (retain similar jet kinematics for background predictions), with additional
1382 selection cuts applied to each control sample to enrich the sample in a particular EWK
1383 processes, see Section (4.2.3).

1384 The jets considered in the analysis are required to have a transverse momentum $p_T > 50$
1385 GeV, with a minimum of two jets required in the event. The highest E_T jet is required
1386 to lie within the central tracker acceptance $|\eta| < 2.5$, and the two leading p_T jets must
1387 each have $p_T > 100$ GeV. Any event which has a jet with $p_T > 50$ GeV that either fails
1388 the “loose” identification criteria described in Section(4.2.1) or has $|\eta| > 3.0$, is rejected.
1389 Similarly events in which an electron, muon or photon fails object identification but pass
1390 η and p_T restrictions are identified as an “odd” lepton/photon and the event is vetoed.

1391 At low H_T , the jet threshold requirements applied to be considered as part of the analysis
1392 and enter the H_T sum are scaled downwards. These are scaled down in order to not
1393 restrict phase space, preserving jet multiplicities and background admixture in the lower
1394 H_T bins, as listed in Table 4.5.

H_T bin	minimum jet p_T	second leading jet p_T
$275 < H_T < 325$	36.7	73.3
$325 < H_T < 375$	43.3	86.6
$375 < H_T$	50.0	100.0

Table 4.5.: Jet thresholds used in the three H_T regions of the analysis.

1395 Within the signal region to suppress SM processes with genuine \cancel{E}_T from neutrinos,
1396 events containing isolated electrons or muons are vetoed. Furthermore to ensure a pure
1397 multi-jet topology, events are vetoed if an isolated photon is found with $p_T > 25$ GeV.

1398 An α_T requirement of > 0.55 is required to reduce the QCD multi-jet background
1399 to a negligible amount. Finally additional cleaning cuts are applied to protect against

1400 pathological deficiencies such as reconstruction failures or severe energy mis-measurements
1401 due to detector inefficiencies:

- Significant \cancel{H}_T can arise in events with no real \cancel{E}_T due to multiple jets falling below the p_T threshold used for selecting jets. This in turn leads to events which can then incorrectly pass the α_T requirements of the analysis. This effect can be negated by requiring that the missing transverse momentum reconstructed from jets alone does not greatly exceed the missing transverse momentum reconstructed from all of the detector's calorimeter towers,

$$R_{miss} = \cancel{H}_T / \cancel{E}_T < 1.25.$$

1402 • Fake \cancel{E}_T and \cancel{H}_T can arise due to significant jet mis-measurements caused by a small
1403 number of non-functioning **ECAL** regions. These regions absorb electromagnetic
1404 showers which are subsequently not added to the jet energy sum. To circumvent
1405 this problem the following procedure is employed : For each jet in the event, the
1406 angular separation

$$\Delta\phi_j^* \equiv \Delta\phi(\vec{p_j} - \sum_{i \neq j} \vec{p_i}), \quad (4.6)$$

1407 is calculated where that jet is itself removed from the event. Here $\Delta\phi^*$ is a measure
1408 of how aligned the \cancel{H}_T of an event is with a jet, a small value is compatible with the
1409 hypothesis of an inherently balanced event in which a jet has been mis-measured.
1410 For every jet in an event with $\Delta\phi^* < 0.5$, if the ΔR distance between the selected jet
1411 and the closest dead **ECAL** region is also < 0.3 , then the event is rejected. Similarly
1412 events are rejected if the jet points within $\Delta R < 0.3$ of the **ECAL** barrel-endcap
1413 gap at $|\eta| = 1.5$.

1414 Some of the key distributions of the data used in this analysis compared to MC simulation
1415 are shown in Figure 4.5. The MC samples are normalised to a luminosity of 11.7 fb^{-1} ,
1416 with no requirement placed upon the number of b-tagged jets or number of jets in the
1417 events.
1418 The distributions shown are presented for purely illustrative purposes, with the MC
1419 simulation itself not used in absolute term to estimate the yields from background

processes, see Sections (4.2.3,4.5). However it is nevertheless important to demonstrate that good agreement exists between simulation and observation in data.

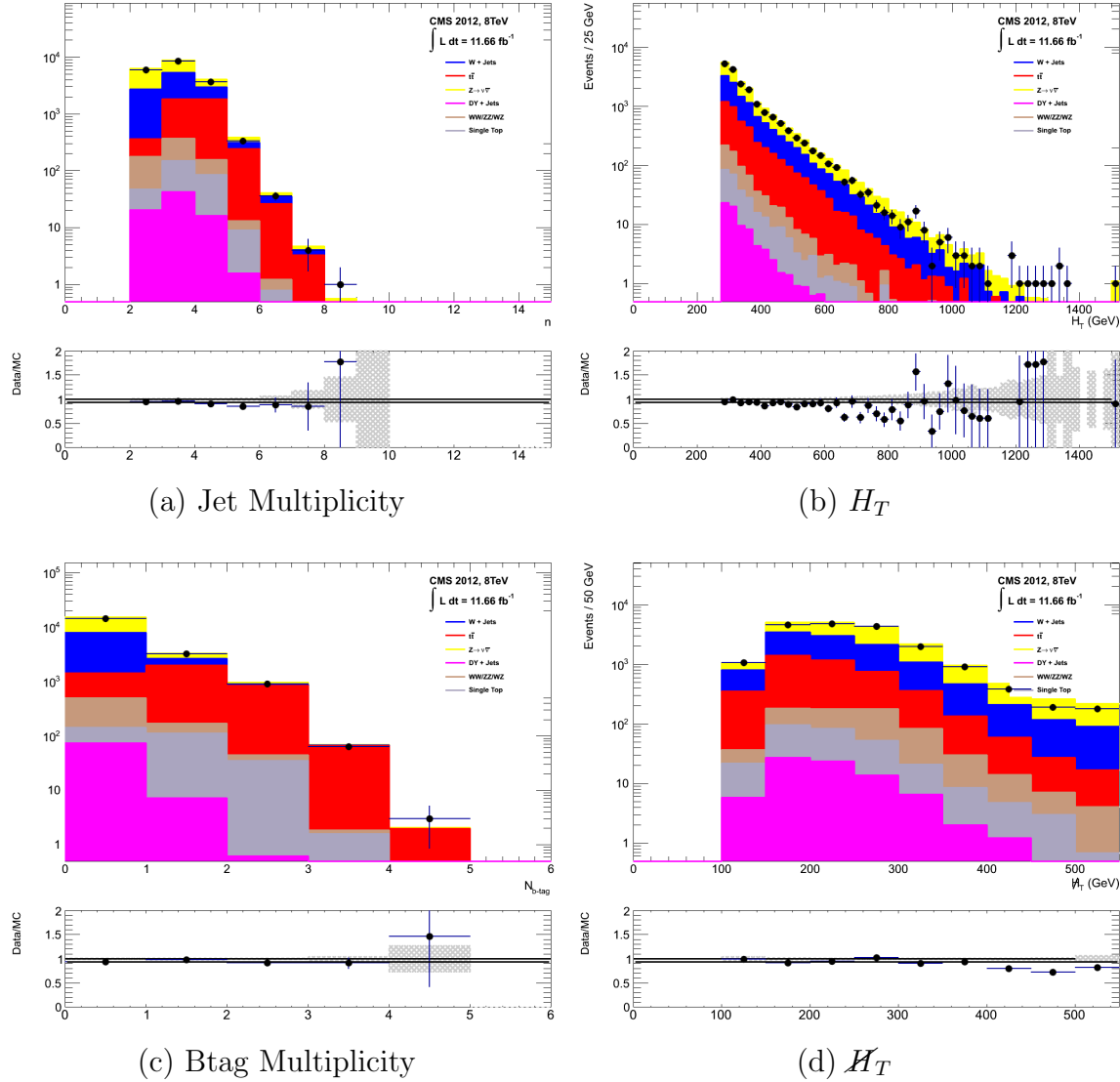


Figure 4.5.: Data/MC comparisons of key variables for the hadronic signal region, following the application of the hadronic selection criteria and the requirements of $H_T > 275$ GeV and $\alpha_T > 0.55$. Bands represent the uncertainties due to the statistical size of the MC samples. No requirement is made upon the number of b-tagged jets or jet multiplicity in these distributions.

4.2.3. Control sample definition and background estimation

The method used to estimate the background contributions in the hadronic signal region relies on the use of a Transfer Factor (TF). This is determined from MC simulation

¹⁴²⁶ in both the control, $N_{MC}^{control}$, and signal, N_{MC}^{signal} , region to transform the observed yield
¹⁴²⁷ measured in data for a control sample, $N_{obs}^{control}$, into a background prediction, N_{pred}^{signal} , via
¹⁴²⁸ Equation (4.7),

$$N_{pred}^{signal} = \frac{N_{MC}^{signal}}{N_{MC}^{control}} \times N_{obs}^{control}. \quad (4.7)$$

¹⁴²⁹ All MC samples are normalised to the luminosity of the data samples, 11.7 fb^{-1} . Through
¹⁴³⁰ this method, “vanilla” predictions for the **SM** background in the signal region can be
¹⁴³¹ made by considering separately the sum of the prediction from either the $\mu + \text{jets}$ and γ
¹⁴³² + jets or $\mu + \text{jets}$ and $\mu\mu + \text{jets}$ samples. However the final background estimation from
¹⁴³³ which results are interpreted, is calculated via a fitting procedure defined formally by
¹⁴³⁴ the likelihood model described in Section (4.8).

¹⁴³⁵ The sum of the expected yields from all MC processes, in each control sample enter the
¹⁴³⁶ denominator, $N_{MC}^{control}$, of the **TF** defined in Eq (4.7). However for the numerator, N_{MC}^{signal} ,
¹⁴³⁷ only the relevant processes that the control sample is used in estimating a background
¹⁴³⁸ for, enter into the **TF**.

¹⁴³⁹ For the $\mu + \text{jets}$ sample the simulated MC processes which enter the numerator of the
¹⁴⁴⁰ **TF** are,

$$N_{MC}^{signal}(H_T, n_{jet}) = N_W + N_{t\bar{t}} + N_{DY} + N_t + N_{di-boson}, \quad (4.8)$$

¹⁴⁴¹ whilst for both the $\mu\mu + \text{jets}$ and $\gamma + \text{jets}$ samples the only MC process used in the
¹⁴⁴² numerator is,

$$N_{MC}^{signal}(H_T, n_{jet}) = N_{Z \rightarrow \nu\bar{\nu}}. \quad (4.9)$$

¹⁴⁴³ The control samples and the **EWK** processes they are specifically tuned to select are
¹⁴⁴⁴ defined below, with distributions of key variables for each of the control samples shown
¹⁴⁴⁵ for illustrative purposes in Figures 4.6, 4.7 and 4.8. No requirement is placed upon
¹⁴⁴⁶ the number of b-tagged jets or jet multiplicity in the distributions shown. The MC

1447 distributions highlight the background compositions of each control sample, where in
1448 general, good agreement is observed between data and simulation, giving confidence
1449 that the samples are well understood. The contribution from QCD multi-jet events is
1450 expected to be negligible :

1451 **The $\mu + \text{jets}$ control sample**

1452 Events from $W + \text{jets}$ and $t\bar{t}$ processes enter into the hadronic signal sample due to
1453 unidentified leptons from acceptance or threshold effects and hadronic tau decays.
1454 These leptons originate from the decay of high p_T W bosons.

1455 The control samples specifically identifies $W \rightarrow \mu\bar{\nu}$ decays within the same phase-
1456 space of the signal region, where the muon is subsequently ignored in the calculation
1457 of event level variables, i.e. H_T , \mathcal{H}_T , α_T . All kinematic jet-based cuts are identical
1458 to those applied in the hadronic search region detailed in Section (4.2.2), with the
1459 same H_T , jet multiplicity and b-jet multiplicity binning described above.

- 1460 – Muons originating from W boson decays are selected by requiring one tightly
1461 isolated muon defined in Table 4.2, with a $p_T > 30$ GeV and $|\eta| < 2.1$. Both of
1462 these threshold arise from trigger restrictions.
- 1463 – The transverse mass of the W candidate must satisfy $M_T(\mu, \cancel{E}_T) < 30$ GeV (to
1464 suppress QCD multi-jet events).
- 1465 – Events which contain a jet overlapping with a muon $\Delta R(\mu, \text{jet}) < 0.5$ are vetoed
1466 to remove events from muons produced as part of a jet's hadronisation process.
- 1467 – Events containing a second muon candidate which has failed id, but passed p_T
1468 and $|\eta|$ requirements, are checked to have an invariant mass that satisfies $m_Z -$
1469 $25 < M_{\mu_1\mu_2} > m_Z + 25$, thus removing $Z \rightarrow \mu\mu$ contamination.

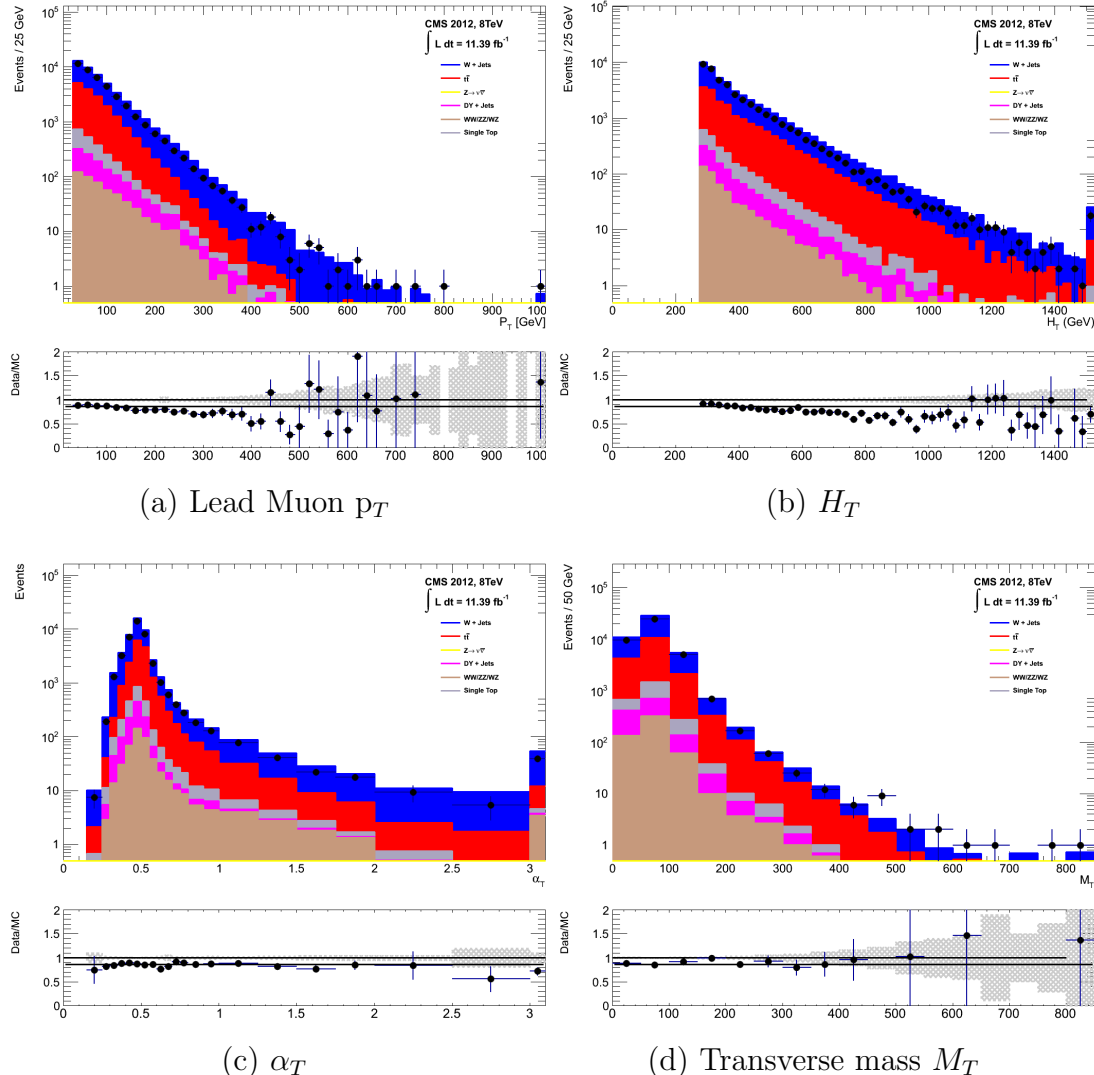


Figure 4.6.: Data/MC comparisons of key variables for the $\mu + \text{jets}$ selection, following the application of selection criteria and the requirements that $H_T > 275$ GeV. Bands represent the uncertainties due to the statistical size of the MC samples. No requirement is made upon the number of b-tagged jets or jet multiplicity in these distributions.

The $\mu\mu + \text{jets}$ control sample

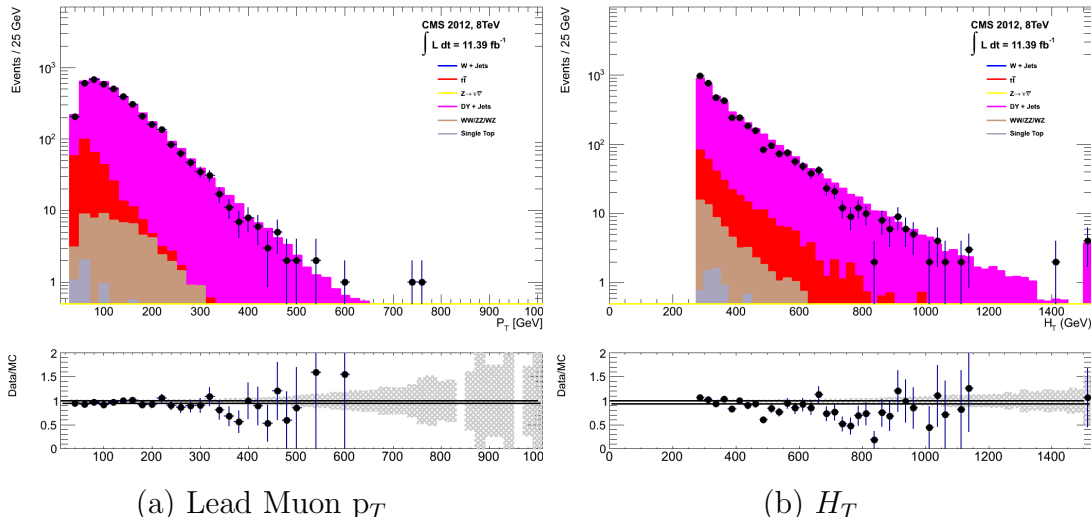
The $Z \rightarrow \nu\bar{\nu} + \text{jets}$ background enters into the signal region from genuine E_T from the escaping neutrinos. This background is estimated using two control samples, the first of which is the $Z \rightarrow \mu\bar{\mu} + \text{jets}$ process, which posses identical kinematic properties, but with different acceptance and branching ratio [1].

The same acceptance requirements as the $\mu + \text{jets}$ selection for muons is applied, as defined in Table 4.2. Muons in the event are ignored for the purpose of the

calculation of event level variables. Kinematic jet-based cuts and phase space binning identical to the hadronic search region are also applied.

- Muons origination from a Z boson decay are selected requiring exactly two tightly isolated muons. Due to trigger requirements the leading muon is required to have $p_T > 30$ GeV and $|\eta| < 2.1$. The requirement of the p_T on the second muon is relaxed to 10 GeV.
- Events are vetoed if containing a jet overlapping with a muon $\Delta R(\mu, \text{jet}) < 0.5$.
- In order to specifically select two muons both originating from a single Z boson decay, the invariant mass of the two muons must satisfy $m_Z - 25 > M_{\mu_1\mu_2} < m_Z + 25$.

The $\mu\mu + \text{jets}$ sample is used to make predictions in the signal region in the two lowest H_T bins, providing coverage where the $\gamma + \text{jets}$ sample is unable to, due to trigger requirements. In higher H_T bins, the higher statistics of the $\gamma + \text{jets}$ sample is instead used to determine the $Z \rightarrow \nu\bar{\nu}$ estimation.



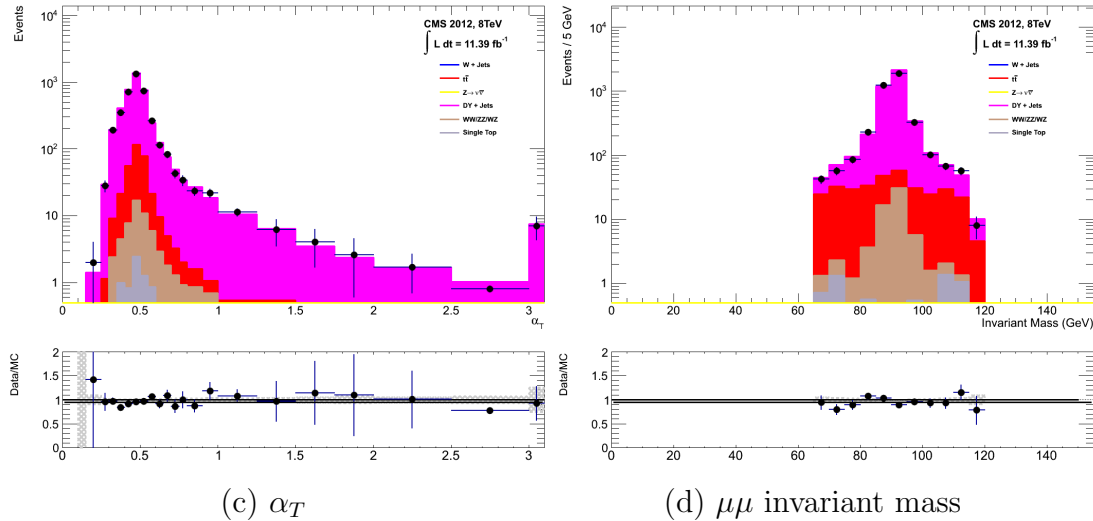


Figure 4.7.: Data/MC comparisons of key variables for the $\mu\mu + \text{jets}$ selection, following the application of selection criteria and the requirements that $H_T > 275$ GeV. Bands represent the uncertainties due to the statistical size of the MC samples. No requirement is made upon the number of b-tagged jets or jet multiplicity in these distributions.

The γ + jets control sample

The $Z \rightarrow \nu\bar{\nu} + \text{jets}$ background is also estimated from a $\gamma + \text{jets}$ control sample, which possesses a larger cross section and kinematic properties similar to those of $Z \rightarrow \mu\bar{\mu}$ events where the photon is ignored [78][79]. The photon is ignored for the purpose of the calculation of event level variables, and identical selection cuts to the hadronic signal region are applied.

- Exactly one photon is selected, satisfying identification criteria as detailed in Table 4.3, with a minimum $p_T > 165$ GeV to satisfy trigger thresholds and $|\eta| < 1.45$ to ensure the photon remains in the barrel of the detector.
 - A selection criteria of $\Delta R(\gamma, jet) < 1.0$, between the photon and all jets is applied to ensure the acceptance of only well isolated $\gamma + \text{jets}$ events.
 - Given that the photon is ignored, this control sample can only be applied in the H_T region > 375 GeV, due to the trigger thresholds on the minimum p_T of the photon, and the H_T requirement of an $\alpha_T > 0.55$ cut from Equation (4.5).

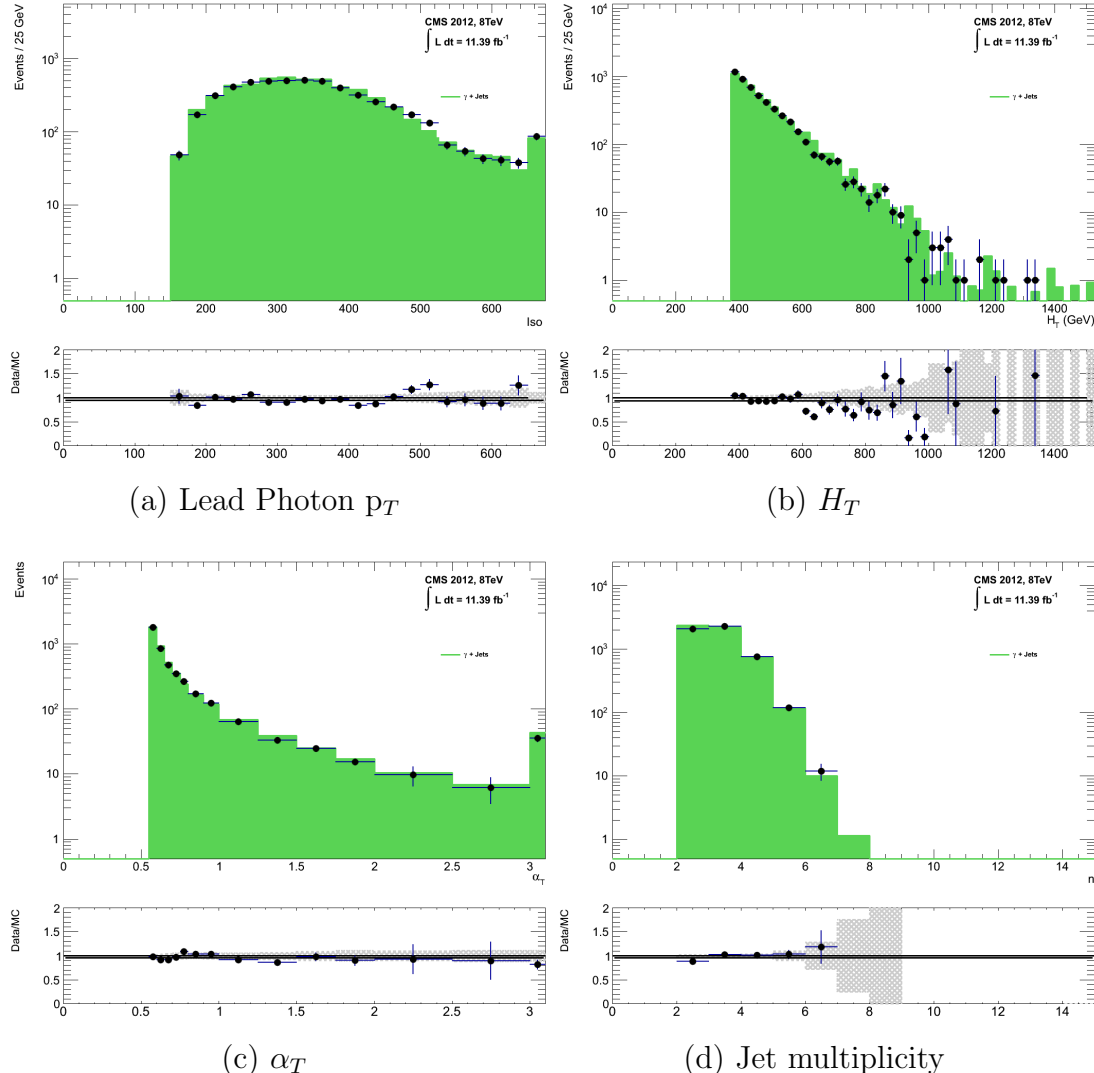


Figure 4.8.: Data/MC comparisons of key variables for the $\gamma + \text{jets}$ selection, following the application of selection criteria and the requirements that $H_T > 375 \text{ GeV}$ and $\alpha_T > 0.55$. Bands represent the uncertainties due to the statistical size of the MC samples. No requirement is made upon the number of b-tagged jets or jet multiplicity in these distributions.

1510 The selection criteria of the three control samples are defined to ensure background
 1511 composition and event kinematics mirror closely the signal region. This is done in order
 1512 to minimise the reliance on MC simulation to model correctly the backgrounds and event
 1513 kinematics in the control and signal samples.

1514 However in the case of the $\mu + \text{jets}$ and $\mu\mu + \text{jets}$ samples, the α_T requirement is relaxed
 1515 in the selection criteria of these samples. This is made possible as contamination from
 1516 QCD multi-jet events is suppressed to a negligible level by the other kinematic selection
 1517 criteria within the two control samples, to select pure EWK processes. Thus in this way,

1518 the acceptance of the two muon control samples can be significantly increased, which
1519 simultaneously improves their predictive power and further reduces the effect of any
1520 potential signal contamination.

1521 The modelling of the α_T variable is probed through a dedicated set of closure tests,
1522 described in Section (4.6), which demonstrate that the different α_T acceptances for the
1523 control and signal samples have no significant systematic bias on the prediction.

1524 4.2.4. Estimating the QCD multi-jet background

1525 A negligible background from QCD multi-jet events within the hadronic signal region
1526 is expected due to the selection requirement, and additional cleaning filters applied.
1527 However a conservative approach is still adopted and the likelihood model, see Section
1528 (4.8.2), is given the freedom to estimate any potential QCD multi-jet contamination.

1529 Any potential contamination can be identified through the variable R_{α_T} , defined as the
1530 ratio of events above and below the α_T threshold value used in the analysis. This is
1531 modelled by a H_T dependant falling exponential function which takes the form,

$$R_{\alpha_T}(H_T) = A \exp^{-k_{QCD} H_T}, \quad (4.10)$$

1532 where the parameters A and k_{QCD} are the normalisation and exponential decay constants
1533 respectively.

1534 For QCD event topologies this exponential behaviour is expected as a function of H_T for
1535 several reasons. The improvement of jet energy resolution at higher H_T due to higher p_T
1536 jets leads to a narrower peaked distribution, causing R_{α_T} to fall. Similarly at higher H_T
1537 values > 375 GeV, the jet multiplicity rises slowly with H_T . As shown in Figure 4.3, at
1538 higher jet multiplicities, the result of the combinatorics used in the determination of α_T ,
1539 also lead to a narrower α_T distribution.

1540 The value of the decay constant k_{QCD} is constrained via measurements within data
1541 sidebands to the signal region. This is also done to validate the falling exponential
1542 assumption for QCD multi-jet topologies. The sidebands are enriched in QCD multi-jet
1543 background and defined as regions where α_T is relaxed or that the R_{miss} cut is inverted.

1544 Figure 4.9 depicts the definition of these data sidebands used to constrain the value of
1545 k_{QCD} .

1546

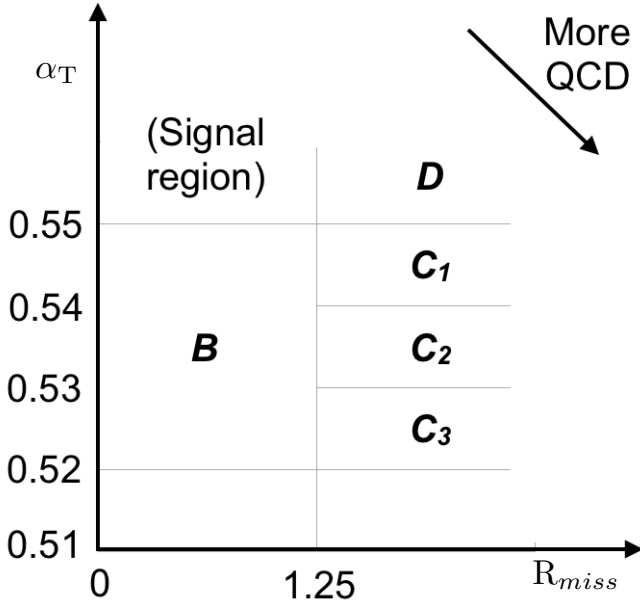


Figure 4.9.: QCD sideband regions, used for determination of k_{QCD} .

1547 The fits to determine the value of k_{QCD} are shown in Appendix (C.1), for which the best
1548 fit value obtained from sideband region B is determined to be $k_{QCD} = 2.96 \pm 0.64 \times 10^{-2}$
1549 GeV^{-1} .

1550 The best fit values of the remaining three C sideband regions are used to estimate
1551 the systematic uncertainty on the central value obtained from sideband region B. The
1552 variation of these measured values is used to determine the error on the determined
1553 central value, and is calculated to be $1.31 \pm 0.26 \times 10^{-2} \text{GeV}^{-1}$. This relative error of \sim
1554 20% gives an estimate of the systematic uncertainty of the measurement to be applied to
1555 k_{QCD} .

1556 Finally the same procedure is performed for sideband region D to establish that the
1557 value of k_{QCD} extracted from a lower α_T slice can be applied to the signal region $\alpha_T >$
1558 0.55. The likelihood fit is performed across all H_T bins within the QCD enriched region
1559 with no constraint applied to k_{QCD} . The resulting best fit value for k_{QCD} shows good
1560 agreement between that and the weighted mean determined from the three C sidebands
1561 regions. This demonstrates that the assumption of using the central value determined
1562 from sideband region B, to provide an unbiased estimator for k_{QCD} in the signal region
1563 ($\alpha_T > 0.55$) is valid.

1564 Table 4.6, summarises the best fit k_{QCD} values determined for each of the sideband
1565 regions to the signal region.

Sideband region	$k_{QCD} (\times 10^{-2} \text{GeV}^{-1})$	p -value
B	2.96 ± 0.64	0.24
C ₁	1.19 ± 0.45	0.93
C ₂	1.47 ± 0.37	0.42
C ₃	1.17 ± 0.55	0.98
C(weighted mean)	1.31 ± 0.26	-
D(likelihood fit)	1.31 ± 0.09	0.57

Table 4.6.: Best fit values for the parameters k_{QCD} obtained from sideband regions B,C₁,C₂,C₃. The weighted mean is determined from the three measurements made within sideband region C. The maximum likelihood value of k_{QCD} given by the simultaneous fit using sideband region D. Quotes errors are statistical only.

1566 4.3. Trigger Strategy

1567 A cross trigger based on the quantities H_T and α_T , labelled is used with varying thresholds
1568 across H_T bins to record the events used in the hadronic signal region. The α_T legs of the
1569 HT_alphaT triggers used in the analysis are chosen to fully suppress QCD multi-jet events,
1570 whilst maintaining a sustainable trigger rate. To further maintain an acceptable rate for
1571 these analysis specific triggers, only calorimeter information is used in the reconstruction
1572 of the H_T sum, leading to the necessity for Calo jets to be used within the analysis.

1573 A single object prescaled H_T trigger is used to collect events for the hadronic control
1574 region described above in Section (4.2.4).

1575 The performance of the α_T and H_T triggers used to collect data for the signal and
1576 hadronic control region is measured with respect to a reference sample collected using the
1577 muon system. This allows measurement of both the Level 1 seed and higher level triggers
1578 simultaneously, as the reference sample is collected independent of any jet requirements.

1579 The selection for the trigger efficiency measurement is identical to that described in
1580 Section (4.2.2), with the requirement of exactly one well identified muon with $p_T > 30$
1581 GeV which is subsequently ignored.

1582 The efficiencies measured for the HT_alphaT triggers in bins individual H_T and α_T legs, is
1583 summarised in Table 4.7.

H_T range (GeV)	ϵ on H_T leg (%)	ϵ on α_T leg (%)
275-325	$87.7^{+1.9}_{-1.9}$	$82.8^{+1.0}_{-1.1}$
325-375	$90.6^{+2.9}_{-2.9}$	$95.9^{+0.7}_{-0.9}$
375-475	$95.7^{+0.1}_{-0.1}$	$98.5^{+0.5}_{-0.9}$
475- ∞	$100.0^{+0.0}_{-0.0}$	$100.0^{+0.0}_{-4.8}$

Table 4.7.: Measured efficiencies of the H_T and α_T legs of the HT and HT_alphaT triggers in independent analysis bins. The product of the two legs gives the total efficiency of the trigger in a given offline H_T bin.

1584 Data for the control samples of the analysis, detailed in Section (4.2.3), are collected
 1585 using single object photon trigger for the $\gamma +$ jets sample, and a single object muon
 1586 trigger for both the $\mu +$ jets and $\mu\mu +$ jets control samples. The photon trigger is
 1587 measured to be full efficient for the threshold $p_T^{photon} > 150 GeV$, whilst the single muon
 1588 efficiency satisfying $p_T^{muon} > 30 GeV$ is measured to have an efficiency of $(88 \pm 2)\%$ that
 1589 is independent of H_T . In the case of the $\mu\mu +$ jets control sample, the efficiency is
 1590 measured to be $(95 \pm 2)\%$ for the lowest H_T bin, rising to $(98 \pm 2)\%$ for the highest H_T
 1591 bin.

1592 4.4. Measuring MC Normalisation Factors via H_T 1593 Sidebands

1594 The theoretical cross sections of different SM processes at Next to Next Leading Order
 1595 (NNLO) and the number of MC simulated events generated for that particular process,
 1596 is typically used to determine the appropriate normalisation for a MC sample. However
 1597 within the particular high- H_T and high- \cancel{E}_T corners of kinematic phase space probed
 1598 within this search, the theoretical cross sections for various processes are far less well
 1599 understood.

1600 To mitigate the problem of theoretical uncertainties and arbitrary choices of cross sections,
 1601 the normalisation of MC samples used in the analysis are determined through the use
 1602 data sidebands. The sidebands are used to calculate sample specific correct factors
 1603 (k-factors) that are appropriate for the H_T - \cancel{E}_T phase space covered by this analysis.

1604 They are defined within the $\mu +$ jets and $\mu\mu +$ jets control sample, by the region $200 <$
 1605 $H_T < 275$, using the same jet p_T thresholds as the adjacent first analysis bin. Individual
 1606 EWK processes are isolated within each of these control samples via requirements on

1607 jet multiplicity and the requirement on b-tags, summarised in Table 4.8. The purity of
1608 the samples are typically $> 90\%$ with any residual contamination corrected for. The
1609 resultant k-factor for each process is determined by then taking ratio of the data yield
1610 over the MC expectation in the sideband. Subsequently these k-factors are then applied
1611 to the processes within the phase space of the analysis.

Process	Selection	Observation	MC expectation	k-factor
W + jets	$\mu + \text{jets, } n_b=0, n_{jet} = 2,3$	26950	29993.2 ± 650.1	0.90 ± 0.02
$Z \rightarrow \mu\mu + \text{jets}$	$\mu\mu + \text{jets, } n_b=0, n_{jet} = 2,3$	3141	3402.0 ± 43.9	0.92 ± 0.02
$t\bar{t}$	$\mu + \text{jets, } n_b=2, n_{jet} = \geq 4$	2190	1967.8 ± 25.1	1.11 ± 0.02

Table 4.8.: k-factors calculated for different EWK processes. All k-factors are derived relative to theoretical cross sections calculated in NNLO. The k-factors measured for the $Z \rightarrow \mu\mu + \text{jets}$ processes, are also applied to the $Z \rightarrow \nu\bar{\nu} + \text{jets}$ and $\gamma + \text{jets}$ MC samples.

1612 4.5. Determining MC Simulation Yields with 1613 Higher Statistical Precision

1614 Reconstructing events from EWK processes with many b-tagged jets (≥ 3), n_b^{reco} , is largely
1615 driven by the mis-tagging of light jets within the event. This is clear when considering
1616 the main EWK backgrounds in the analysis, such as $t\bar{t} + \text{jets}$ events, which typically
1617 contain two b-flavoured jets from the decay of the top quarks, whilst W + jets and
1618 $Z \rightarrow \mu\mu + \text{jets}$ events will typically contain no b-flavoured jets.

1619 When the expectation for the number of n_b^{reco} is taken directly from simulation, the
1620 statistical uncertainty at large b-tag multiplicities becomes relatively large. In order to
1621 reduce this uncertainty one approach is to use the information encoded throughout all
1622 events in the simulation sample, to measure each of the four ingredients:

- 1623 1. the b-tagging efficiency in the event selection,
- 1624 2. the charm-tagging efficiency in the event selection
- 1625 3. the mis-tagging rate in the event selection,
- 1626 4. the underlying flavour distribution of the jets in the events,

1627 that determine the n_b^{reco} distribution of the process being measured. This method allows
1628 the determination of higher b-tag multiplicities to a higher degree of accuracy reducing

₁₆₂₉ the statical uncertainties of the MC which enter into the TF's. For the discussion that
₁₆₃₀ follows, these predictions are determined on average (i.e not on an event-by-event basis),
₁₆₃₁ and is known as the formula method.

₁₆₃₂ **4.5.1. The formula method**

₁₆₃₃ The assigning of jet flavours to reconstruction level jets in simulation is achieved via an
₁₆₃₄ algorithmic method defined as:

- ₁₆₃₅ • Try to find the parton that most likely determines the properties of the jet and
₁₆₃₆ assign that flavour as true flavour,
- ₁₆₃₇ • Here, the “final state” partons (after showering, radiation) are analysed (also within
₁₆₃₈ $\Delta R < 0.3$ of reconstructed jet cone),
- ₁₆₃₉ • Jets from radiation are matched with full efficiency,
- ₁₆₄₀ • If there is a b/c flavoured parton within the jet cone: label as b/c flavoured jet,
- ₁₆₄₁ • Otherwise: assign flavour of the hardest parton.

₁₆₄₂ Within each individual MC process and each H_T - n_{jet} bin in the analysis, the n_b^{reco}
₁₆₄₃ distribution is constructed in the following way:

₁₆₄₄ Let $N(n_b^{gen}, n_c^{gen}, n_q^{gen})$ represent the yield in simulation of events with b underlying
₁₆₄₅ b-quarks, c underlying c-quarks and q underlying light quarks which are matched to
₁₆₄₆ reconstructed jets as detailed above. Light quarks defined as those which originate from
₁₆₄₇ a u , d , s , g and τ jets, which having similar mis-tagging rates are grouped together.
₁₆₄₈ Similarly ϵ , β and m represent the measured b-tagging, c-tagging and mis-tagging
₁₆₄₉ efficiency averaged over all the jets within that particular analysis bin.

₁₆₅₀ Using this information the expected n_b^{reco} distribution can be analytically calculated
₁₆₅₁ using the formula :

$$N(n_b) = \sum_{n_b^{gen} + n_c^{gen} + n_q^{gen} = n_{jet}} \sum_{n_b^{tag} + n_c^{tag} + n_q^{tag} = n_b} N(n_b^{gen}, n_c^{gen}, n_q^{gen}) \times P(n_b^{tag}, n_b^{gen}, \epsilon) \times \\ P(n_c^{tag}, n_c^{gen}, \beta) \times P(n_q^{tag}, n_q^{gen}, m), \quad (4.11)$$

1652 with $N(n_b)$ representing the yield where n_b jets have been b-tagged. The variables
1653 n_b^{tag} , n_c^{tag} and n_q^{tag} represent the number of times that a particular jet flavour results
1654 in a b-tagged jet, and $P(n_b^{tag}, n_b^{gen}, \epsilon)$, $P(n_c^{tag}, n_c^{gen}, \beta)$ and $P(n_q^{tag}, n_q^{gen}, m)$ represent the
1655 binomial probabilities for that to happen.

1656 This approach ultimately results in a more precise n_b^{reco} distribution prediction as
1657 information from throughout the entire MC sample is used to estimate the underlying
1658 n_b^{reco} distribution.

1659 4.5.2. Establishing proof of principle

1660 In order to validate the procedure, the predictions obtained from the formula method
1661 summarised in Equation (4.11), are compared directly to those obtained directly from
1662 simulation. Resultantly no simulation to data correction factors are applied when making
1663 this comparison

1664 This sanity check for the $\mu +$ jets control sample is presented in Table 4.9, for all n_b^{reco}
1665 and H_T bins with no requirement placed upon the jet multiplicity of the events.

1666 It can be seen as expected, that there is good consistency between the results determined
1667 via the formula method and ‘raw’ simulation yields. Similarly the power of this approach
1668 can be seen in the reduction of this statistical error in the prediction across all H_T and
1669 n_b^{reco} bins. In particular the statistical uncertainty is reduced by several factors in the
1670 highest $n_b^{reco} \geq 4$ category.

1671 4.5.3. Correcting measured efficiencies in simulation to data

1672 As detailed in Section (3.3.2), it is necessary for certain p_T and η dependant corrections,
1673 to be applied to both the b-tagging efficiency and mis-tagging rates in order correct the
1674 efficiencies from simulation to the distributions seen in data. These corrections factors
1675 are considered when determining the simulation yields for each selection, which are used
1676 to construct the TF’s of the analysis.

1677 Each of the corrections factors for the b, c and light flavoured jets come with an associated
1678 systematic uncertainty. The uncertainties across different jet p_T and η bins, are considered
1679 as fully correlated. When computing the magnitude of the effect of this systematic
1680 uncertainty on the TF’s of the analysis, the scale factors are therefore scaled up/down

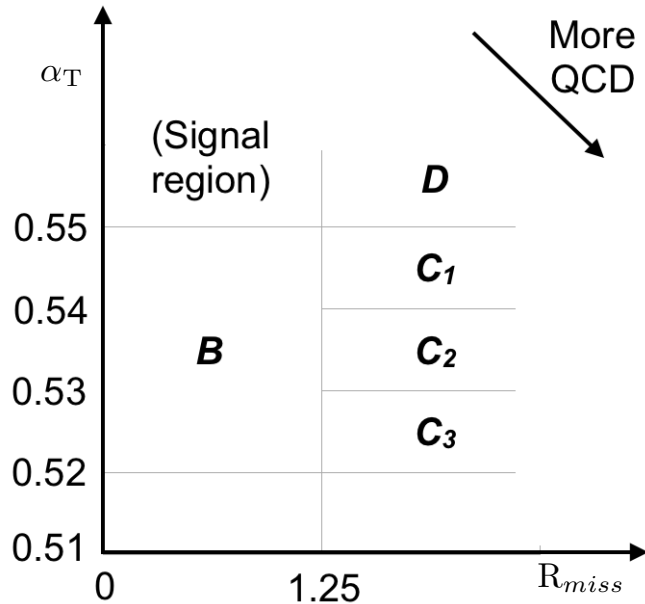
H_T Bin (GeV)	275–325	325–375	375–475	475–575
Formula $n_b = 0$	12632.66 \pm 195.48	6696.08 \pm 82.59	6368.96 \pm 75.34	2906.27 \pm 39.65
Vanilla $n_b = 0$	12612.95 \pm 198.68	6687.97 \pm 83.78	6359.27 \pm 76.50	2898.27 \pm 36.89
Formula $n_b = 1$	4068.09 \pm 45.71	2272.76 \pm 26.14	2181.32 \pm 25.07	1089.14 \pm 13.82
Vanilla $n_b = 1$	4067.73 \pm 60.30	2268.02 \pm 30.20	2180.69 \pm 28.73	1094.37 \pm 24.14
Formula $n_b = 2$	1963.71 \pm 22.44	1087.55 \pm 13.57	1055.57 \pm 13.25	554.96 \pm 7.95
Vanilla $n_b = 2$	1984.53 \pm 26.19	1094.43 \pm 16.67	1068.96 \pm 16.36	558.14 \pm 10.51
Formula $n_b = 3$	146.94 \pm 2.07	79.97 \pm 1.37	78.05 \pm 1.35	49.84 \pm 1.03
Vanilla $n_b = 3$	149.52 \pm 4.84	85.98 \pm 3.64	74.45 \pm 3.29	49.54 \pm 2.68
Formula $n_b \geq 4$	2.26 \pm 0.12	1.29 \pm 0.10	5.32 \pm 0.20	-
Vanilla $n_b \geq 4$	1.84 \pm 0.50	1.02 \pm 0.39	4.86 \pm 0.83	-

H_T Bin (GeV)	575–675	675–775	775–875	>875
Formula $n_b = 0$	1315.68 \pm 19.49	640.49 \pm 11.90	327.81 \pm 7.91	424.27 \pm 9.27
Vanilla $n_b = 0$	1315.23 \pm 20.20	641.96 \pm 12.48	329.09 \pm 8.36	424.02 \pm 9.73
Formula $n_b = 1$	490.41 \pm 7.45	226.95 \pm 4.42	109.91 \pm 2.84	129.97 \pm 3.07
Vanilla $n_b = 1$	490.52 \pm 9.92	222.22 \pm 6.21	107.46 \pm 4.15	129.64 \pm 4.64
Formula $n_b = 2$	256.75 \pm 4.58	113.45 \pm 2.70	52.10 \pm 1.69	59.29 \pm 1.78
Vanilla $n_b = 2$	253.43 \pm 6.52	117.17 \pm 4.27	52.70 \pm 2.80	59.45 \pm 3.00
Formula $n_b = 3$	25.66 \pm 0.69	12.48 \pm 0.46	5.52 \pm 0.31	6.83 \pm 0.33
Vanilla $n_b = 3$	29.18 \pm 2.06	11.77 \pm 1.26	6.18 \pm 0.95	7.53 \pm 1.05

Table 4.9.: Comparing yields in simulation within the $\mu +$ jets selection determined from the formula method described in Equation (4.11), and that taken directly from simulation . The numbers are normalised to 11.4fb^{-1} . No simulation to data corrections are applied.

¹⁶⁸¹ simultaneously within H_T bin of the analysis for each of the $SF_{b,c,s}$ scale factors. The
¹⁶⁸² magnitude of this correction is shown for each H_T bin within Figure 4.10.

1683

**Figure 4.10.: placeholder.**

1684 Varying the scale factor corrections by their systematic uncertainty will change the
 1685 absolute yields within each n_b^{reco} bin of all selections. However, ultimately it is the change
 1686 in the TF's which influences the final background prediction from each of the control
 1687 samples. The magnitude of these change is shown in Table 4.10, highlighting the absolute
 1688 change in each TF, constructed from when the $\mu +$ jets control sample is used to predict
 1689 the entire hadronic signal region background.

1690 It can be seen that the TF's are found to be relatively insensitive to the systematic
 1691 uncertainty of the b-tag scale factors (showing typically less than $\sim 2\%$ change). This can
 1692 be accounted for by the similar composition of the signal and control sample backgrounds,
 1693 such that any change in the underlying n_b^{reco} distribution will be reflected in both signal
 1694 and control regions and cancel out in the TF.

1695 Any overall systematic effect on the overall background prediction of the analysis from
 1696 these b-tag scale factor uncertainties is incorporated within the data driven systematics
 1697 introduced in the following section.

n_b^{reco}	275–325	325–375	375–475	475–575
= 0	0.557 $^{+0.001}_{-0.001}$ \pm 0.012	0.495 $^{+0.001}_{-0.001}$ \pm 0.009	0.383 $^{+0.001}_{-0.001}$ \pm 0.005	0.307 $^{+0.001}_{-0.002}$ \pm 0.006
= 1	0.374 $^{+0.006}_{-0.006}$ \pm 0.006	0.320 $^{+0.006}_{-0.005}$ \pm 0.005	0.251 $^{+0.005}_{-0.005}$ \pm 0.004	0.185 $^{+0.003}_{-0.003}$ \pm 0.004
= 2	0.226 $^{+0.002}_{-0.002}$ \pm 0.004	0.201 $^{+0.001}_{-0.002}$ \pm 0.004	0.159 $^{+0.001}_{-0.001}$ \pm 0.004	0.134 $^{+0.000}_{-0.001}$ \pm 0.004
= 3	0.221 $^{+0.002}_{-0.002}$ \pm 0.005	0.208 $^{+0.002}_{-0.001}$ \pm 0.007	0.164 $^{+0.001}_{-0.000}$ \pm 0.006	0.144 $^{+0.001}_{-0.001}$ \pm 0.007
≥ 4	0.222 $^{+0.004}_{-0.005}$ \pm 0.015	0.248 $^{+0.003}_{-0.003}$ \pm 0.035	0.123 $^{+0.002}_{-0.003}$ \pm 0.009	-
<hr/>				
	575–675	675–775	775–875	≥ 875
<hr/>				
= 0	0.263 $^{+0.001}_{-0.002}$ \pm 0.006	0.215 $^{+0.000}_{-0.001}$ \pm 0.007	0.171 $^{+0.000}_{-0.001}$ \pm 0.009	0.111 $^{+0.000}_{-0.001}$ \pm 0.006
= 1	0.154 $^{+0.003}_{-0.003}$ \pm 0.005	0.138 $^{+0.003}_{-0.004}$ \pm 0.006	0.121 $^{+0.005}_{-0.005}$ \pm 0.007	0.091 $^{+0.002}_{-0.002}$ \pm 0.006
= 2	0.104 $^{+0.000}_{-0.001}$ \pm 0.005	0.079 $^{+0.001}_{-0.001}$ \pm 0.006	0.063 $^{+0.001}_{-0.002}$ \pm 0.007	0.071 $^{+0.000}_{-0.000}$ \pm 0.008
= 3	0.116 $^{+0.001}_{-0.001}$ \pm 0.009	0.069 $^{+0.001}_{-0.001}$ \pm 0.007	0.079 $^{+0.001}_{-0.001}$ \pm 0.017	0.095 $^{+0.003}_{-0.002}$ \pm 0.020

Table 4.10.: The absolute change in the **TF**'s used to predict the entire signal region **SM** background, using the $\mu +$ jets control sample when the systematic uncertainties of the data to simulation scale factors are varied by $\pm 1\sigma$. The impact of the change is shown for each H_T and n_b^{reco} bin with no requirement made on the jet multiplicity of the events. (Also quoted are the statistical uncertainties)

1698 4.6. Systematic Uncertainties on Transfer Factors

1699 Since the **TF**'s used to establish the background prediction are obtained from simulation,
1700 an appropriate systematic uncertainty is assigned to each factor to account for theoretical
1701 uncertainties [80] and limitations in the simulation modelling of event kinematics and
1702 instrumental effects.

1703 The magnitudes of these systematic uncertainties are established through a set of data
1704 driven method, in which the three independent control samples of the analysis ($\mu +$ jets,
1705 $\mu\mu +$ jets, $\gamma +$ jets) are used to in a series of closure tests. The yields from one of these
1706 control samples, along with the corresponding **TF** obtained from simulation, are used to
1707 predict the yields in another control sample, using the same method of establishing a
1708 background prediction for the signal region as described in Section (4.2.3).

1709 The level of agreement between the predicted and observed yields is expressed as the
1710 ratio

$$\frac{(N_{obs} - N_{pred})}{N_{pred}}, \quad (4.12)$$

1711 while considering only the statistical uncertainties on N_{pred} , the prediction, and N_{obs} , the
 1712 observation. No systematic uncertainty is assigned to the prediction, and resultantly the
 1713 level of closure is defined by the statistical significance of a deviation from the ratio from
 1714 zero.

1715 This ratio is measured for each H_T bin in the analysis, allowing these closure tests to be
 1716 sensitive to both the presence of any significant biases or any possible H_T dependence on
 1717 the level of closure.

1718 Eight sets of closure tests are defined between the three data control samples, conducted
 1719 independently between the two jet multiplicity ($2 \leq n_{jets} \leq 3$, $n_{jet} \geq 4$) bins. Each of
 1720 these tests are specifically chosen to probe each of the different key ingredients of the
 1721 simulation modelling that can affect the background prediction.

1722 Each of the different modelling components and the relevant closure tests are described
 1723 below :

1724 **α_T modelling**

1725 The modelling of the α_T distribution in genuine \cancel{E}_T events is probed with the $\mu +$
 1726 jets control sample. This test is important to verify the approach of remove the α_T
 1727 > 0.55 requirement from the $\mu +$ jets and $\mu\mu +$ jets samples to increase the precision
 1728 of the background prediction. The test uses the $\mu +$ jets sample without an α_T cut
 1729 to make a prediction into the $\mu +$ jets sample defined with the requirement $\alpha_T >$
 1730 0.55.

1731 **Background admixture**

1732 The sensitivity of the translation factors to the relative admixture of events from
 1733 $W +$ jets and $t\bar{t}$ processes is probed by two closure tests. These tests represent
 1734 an extremely conservative approach as the admixture of the background remains
 1735 similar between the $\mu +$ jets sample and the signal region, contrary to the defined
 1736 closure tests which make predictions between two very different admixtures of $W +$
 1737 jets and $t\bar{t}$ events.

1738 Within the $\mu + \text{jets}$ sample, a W boson enriched sub-sample ($n_b = 0$) is used to
1739 predict yields in a $t\bar{t}$ enriched sub-sample ($n_b = 1$). Similarly the
1740 $t\bar{t}$ enriched sub-sample ($n_b = 1$) is also used to predict yields for a further enriched
1741 $t\bar{t}$ sub-sample ($n_b = 2$).

1742 Similarly a further closure test probes the relative contribution of $Z + \text{jets}$ to $W + \text{jets}$
1743 and $t\bar{t}$ events, through the use of the $\mu + \text{jets}$ sample to predict yields for the $\mu\mu +$
1744 jets control sample. This closure test, also at some level probes the muon trigger
1745 and reconstruction efficiencies, given that exactly one and two muons are required
1746 by the different selections.

1747 Consistency between control samples

1748 An important consistency check between the $\mu\mu + \text{jets}$ jets and $\gamma + \text{jets}$, which are
1749 both used in the prediction of the $Z \rightarrow \nu\bar{\nu}$ in the signal region, is measured by using
1750 the $\gamma + \text{jets}$ sample to predict yields for the $\mu\mu + \text{jets}$ control sample.

1751 Modelling of jet multiplicity

1752 The simulation modelling of the jet multiplicity within each control sample is
1753 important due to the exclusive jet multiplicity binning within the analysis. This is
1754 probed via the use of each of the three control samples to independently predict
1755 from the lower jet multiplicity category $2 \leq n_{jet} \leq 3$, to the high jet category ≥ 4 .

1756 For the case of the $\mu + \text{jets}$ and $\mu\mu + \text{jets}$ control samples this test is also a
1757 further probe of the admixture between $W + \text{jets}/Z + \text{jets}$ and $t\bar{t}$.

1758 To test for the assumption that no H_T dependences exist within the background predic-
1759 tions of the analysis, the first five closure tests defined above are taken, with zeroeth and
1760 first order polynomial fits are applied to each. This is summarised in Table 4.11 and
1761 Table 4.12 which show the results for both the $2 \leq n_{jet} \leq 3$ and ≥ 4 jet multiplicity bins
1762 respectively.

1763 Table 4.13 shows the same fits applied to the three closure tests that probe the modelling
1764 between the different n_{jet} bins. The best fit value and its uncertainty is listed for each
1765 set of closure tests in all three tables, along with the p-value of the constant and linear
1766 fits applied.

1767 The best fit value for the constant parameter is indicative of the level of closure, averaged
1768 across the full range of H_T bins in the analysis, and the p-value an indicator of any
1769 significant dependence on H_T within the closure tests. The best fit values of all the tests

Closure test	Symbol	Constant fit		Linear fit	
		Best fit value	p-value	Slope (10^{-4})	p-value
$\alpha_T < 0.55 \rightarrow \alpha_T > 0.55 (\mu + \text{jets})$	Circle	-0.06 ± 0.02	0.93	-1.3 ± 2.2	0.91
$0 \text{ b-jets} \rightarrow 1 \text{ b-jet } (\mu + \text{jets})$	Square	0.07 ± 0.02	0.98	-1.6 ± 1.6	1.00
$1 \text{ b-jets} \rightarrow 2 \text{ b-jet } (\mu + \text{jets})$	Triangle	-0.07 ± 0.03	0.76	-2.7 ± 3.0	0.76
$\mu + \text{jets} \rightarrow \mu\mu + \text{jets}$	Cross	0.10 ± 0.03	0.58	-1.1 ± 2.3	0.49
$\mu\mu + \text{jets} \rightarrow \gamma + \text{jets}$	Star	-0.06 ± 0.04	0.31	4.2 ± 4.3	0.29

Table 4.11.: A summary of the results obtained from fits of zeroeth order polynomials (i.e. a constant) to five sets of closure tests performed in the $2 \leq n_{jet} \leq 3$ bin. The final two columns show the best fit value for the slope obtained when performing a linear fit and the p-value for the linear fit.

Closure test	Symbol	Constant fit		Linear fit	
		Best fit value	p-value	Slope (10^{-4})	p-value
$\alpha_T < 0.55 \rightarrow \alpha_T > 0.55 (\mu + \text{jets})$	Circle	-0.05 ± 0.03	0.21	3.0 ± 2.9	0.21
$0 \text{ b-jets} \rightarrow 1 \text{ b-jet } (\mu + \text{jets})$	Square	-0.03 ± 0.03	0.55	-1.0 ± 1.9	0.47
$1 \text{ b-jets} \rightarrow 2 \text{ b-jet } (\mu + \text{jets})$	Triangle	-0.02 ± 0.03	0.39	1.1 ± 2.2	0.31
$\mu + \text{jets} \rightarrow \mu\mu + \text{jets}$	Cross	0.08 ± 0.07	0.08	4.8 ± 4.3	0.07
$\mu\mu + \text{jets} \rightarrow \gamma + \text{jets}$	Star	-0.03 ± 0.10	0.72	-4.0 ± 7.0	0.64

Table 4.12.: A summary of the results obtained from fits of zeroeth order polynomials (i.e. a constant) to five sets of closure tests performed in the $n_{jet} \geq q$ bin. The final two columns show the best fit value for the slope obtained when performing a linear fit and the p-value for the linear fit.

Closure test	Symbol	Constant fit		Linear fit	
		Best fit value	p-value	Slope (10^{-4})	p-value
$\mu + \text{jets}$	Inverted triangle	-0.03 ± 0.02	0.02	0.0 ± 1.0	0.01
$\mu + \text{jets}$ (outlier removed)	Inverted triangle	-0.04 ± 0.01	0.42	-1.4 ± 1.1	0.49
$\gamma + \text{jets}$	Diamond	0.12 ± 0.05	0.79	6.0 ± 4.7	0.94
$\mu\mu + \text{jets}$	Asterisk	-0.04 ± 0.07	0.20	4.9 ± 4.4	0.20

Table 4.13.: A summary of the results obtained from fits of zeroeth order polynomials (i.e. a constant) to five sets of closure tests performed in the $2 \leq n_{jet} \leq 3$ bin. The final two columns show the best fit value for the slope obtained when performing a linear fit and the p-value for the linear fit.

are either statistically compatible with zero bias (i.e, less than 2σ from zero) or at the level of 10% or less, with the exception of one closure test discussed below.

Within Table 4.13, there exists one test that does not satisfy the above statement, which is the $2 \leq n_{jet} \leq 3 \rightarrow n_{jet} \geq 4$ test using the $\mu + \text{jets}$ control sample. The low p-value can be largely attributed to an outlier in the $675 < H_T < 775$ GeV bin, rather than any significant trend in H_T . Removing this single outlier from the constant fit performed, gives a best fit value of -0.04 ± 0.01 , $\chi^2/\text{d.o.f} = 6.07/6$. and a p-value of 0.42. These modified fit results are included within Table 4.13 .

1778 In addition the best fit values for the slope terms of the linear fits in all three tables are
1779 of the order 10^{-4} , which corresponds to a percent level change per 100 GeV. However in
1780 all cases, the best fit values are fully compatible with zero (within 1σ) once again with
1781 the exception detailed above, indicating that the level of closure is H_T independent.

1782 4.6.1. Determining systematic uncertainties from closure tests

1783 Once it has been established that no significant bias or trend has been exist within
1784 the closure tests, systematic uncertainties are determined. The statistical precision
1785 of the closure tests is considered a suitable benchmark for determining the systematic
1786 uncertainties that are assigned to the TF's, which are propagated through to the likelihood
1787 fit.

1788 The systematic uncertainty band is split into five separate regions of H_T . Within each
1789 region the square root of the sample variance, σ^2 , is taken over the eight closure tests to
1790 determine the systematic uncertainties to be applied within that region.

1791 Using this procedure the systematic uncertainties for each region are calculated and are
1792 shown in Table 4.14, with the systematic uncertainty to be used in the likelihood model
1793 conservatively rounded up to the nearest decile, shown in brackets.

H_T band (GeV)	$2 \leq n_{jet} \leq 3$	$n_{jet} \geq 4$
$275 < H_T < 325$	6 (10)%	3 (10)%
$325 < H_T < 375$	6 (10)%	6 (10)%
$375 < H_T < 575$	7 (10)%	9 (10)%
$575 < H_T < 775$	13 (20)%	15 (20)%
$H_T > 775$	19 (20)%	21 (30)%

Table 4.14.: Calculated systematic uncertainties for the five H_T regions, determined from the closure tests. Uncertainties shown for both jet multiplicity categories. Values used within the likelihood model are conservatively rounded up to the nearest decile and shown in brackets.

1794 Figure 4.11 shows the sets of closure tests overlaid on top of grey bands that represent
1795 the H_T dependent systematic uncertainties. These systematic uncertainties are assumed
1796 to fully uncorrelated between the different n_b multiplicity categories and across the five
1797 H_T regions. This can be considered a more conservative approach given that some
1798 correlations between adjacent H_T bins could be expected due to comparable kinematics.

1799 As already referenced. These closure tests represent a conservative estimate of the
1800 systematic uncertainty in making a background perdition for the signal region. This

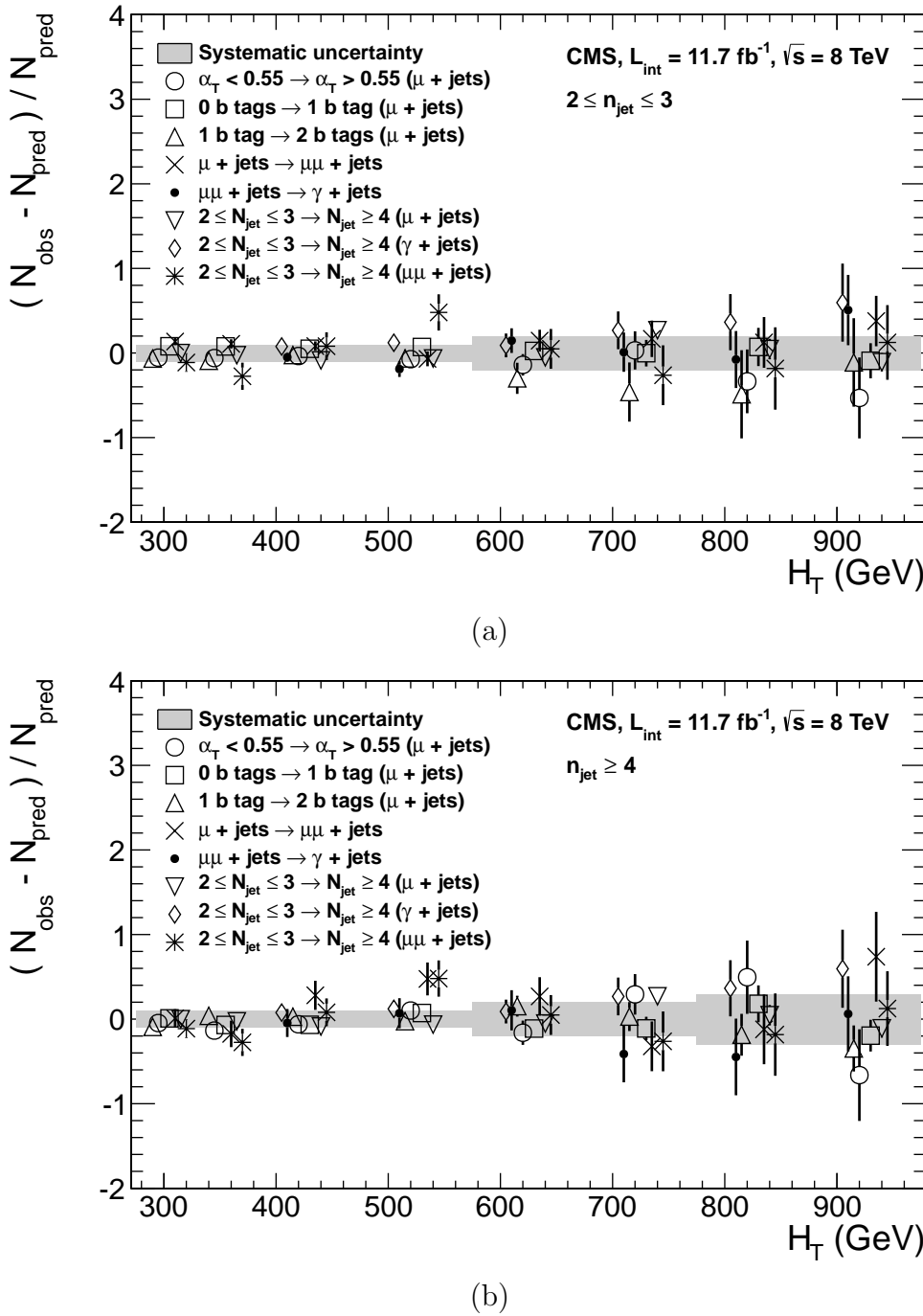


Figure 4.11.: Sets of closure tests (open symbols) overlaid on top of the systematic uncertainty used for each of the five H_T regions (shaded bands) and for the two different jet multiplicity bins: (a) $2 \leq n_{\text{jet}} \leq 3$ and (b) $n_{\text{jet}} \geq 4$.

¹⁸⁰¹ is due to significant differences in the background composition and event kinematics
¹⁸⁰² between the two sub-samples used in the closure tests. This is contrary to the signal
¹⁸⁰³ region prediction where the two sub-samples are both have a comparable background

1804 admixture and similar kinematics owing to the fact that the predictions are always made
1805 using the same (n_{jet}, n_b, H_T) bin.

1806 This point is emphasised when we examine the sensitivity of the **TF**'s to a change in the
1807 admixture of W + jets and $t\bar{t}$ with the control and signal samples. This is accomplished
1808 by varying the cross sections of the W + jets and $t\bar{t}$ by +20% and -20%, respectively.
1809 Figures C.2 and C.3 within Appendix C, show the effect upon the closure tests for both
1810 jet multiplicity categories. Given these variations in cross sections, the level of closure is
1811 found to be significantly worse, with biases as large as $\sim 30\%$, most apparent in the
1812 lowest H_T bins. However the **TF**'s used to extrapolate from control to signal are seen to
1813 change only at the percent level by this large change in cross section, shown in Table C.1.

1814 Given the robust behaviour of the translation factors with respect to large (and opposite)
1815 variations in the W + jets and $t\bar{t}$ cross sections, one can assume with confidence that
1816 any bias in the translation factors is adequately (and conservatively) covered by the
1817 systematic uncertainties used in the analysis.

1818 4.7. Simplified Models, Efficiencies and Systematic 1819 Uncertainties

1820 The results of the analysis are interpreted using various **SMS** signal models as already
1821 introduced in Section (2.4.1). Each model is parameterised in a two dimensional parameter
1822 space, ($m_{\tilde{q}/\tilde{g}}, m_{LSP}$), from which upper limits on the production cross sections of the
1823 various **SMS** models can be set.

1824 Each signal sample is generated at Next to Leading Order (**NLO**) and Next to Leading
1825 Logarithmic Order (**NLL**) [81] using the **Fastsim** framework. This framework represents
1826 a simplified simulation of the **CMS** detector, but allows for faster production of various
1827 signal topologies with different mass parameters. A series of correction factors are applied
1828 to account for the effects on the b-tagging rate between **Fastsim** [82] and **Fullsim** [83]
1829 and are detailed in Section (4.7.2).

1830 **4.7.1. Signal efficiency**

1831 The analysis selection efficiency, ϵ , is measured for each mass point of the interpreted
 1832 model, this serves as a measure of the sensitivity of the signal selection for that particular
 1833 sparticle and LSP mass . The signal yield is then given by

$$Y(m_{\tilde{q}/\tilde{g}}, m_{LSP}) = \epsilon \times \sigma \times \mathcal{L}, \quad (4.13)$$

1834 where σ represents the model's cross section and \mathcal{L} the luminosity. An upper limit on σ
 1835 taken from theory can then allow for the setting of limits in terms of the particle mass.

1836 Figure 4.12 shows the expected signal efficiency of the signal selection for the T1 and
 1837 T2 SMS models interpreted in this analysis. The efficiency maps are produced with the
 1838 requirement $H_T > 275$ GeV (i.e., no binning in H_T) and requirements on n_{jet} and n_b^{reco}
 1839 that are appropriate for the model in question.

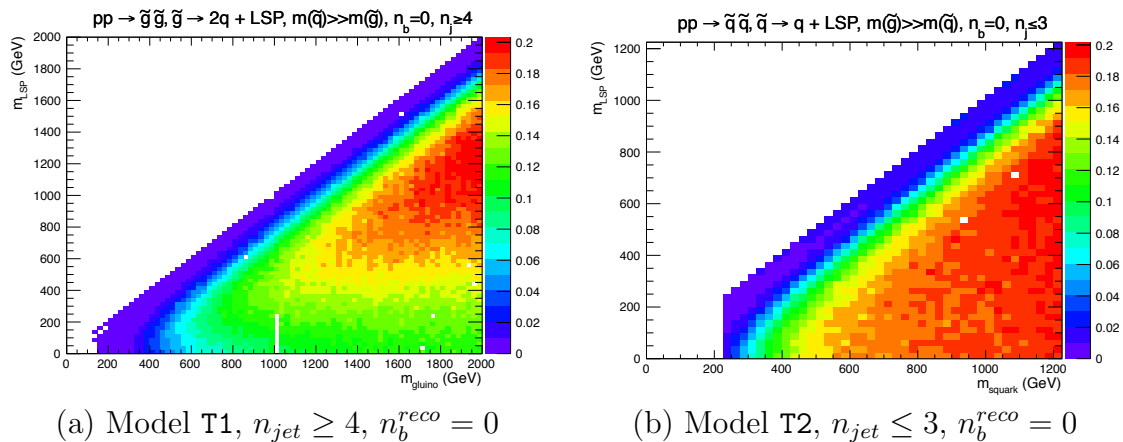


Figure 4.12.: Signal efficiencies for the SMS models (a) T1 ($\tilde{g}\tilde{g}^* \rightarrow q\tilde{\chi}_1^0 q\tilde{\chi}_1^0$) and (b) T2 ($\tilde{q}\tilde{q}^* \rightarrow q\tilde{\chi}_1^0 \bar{q}\tilde{\chi}_1^0$) when requiring $n_{jet} \geq 4$ and ≤ 3 respectively, and $n_b^{reco} = 0$.

1840 The same procedure is conducted in the analysis control samples. It is found in the μ
 1841 + jets control samples, that the S/B ratios for the expected signal yields in each of the
 1842 SMS models are many times (~ 40 -100) smaller than in the hadronic signal region. The
 1843 relative contamination for the $\mu\mu$ + jets sample is smaller still due to the requirement of
 1844 a second muon. The relative contamination for the γ + jets sample is expected to be
 1845 zero for the models under consideration. These small, relative levels of contamination
 1846 are accounted for in the fitting procedure, as described in Section (4.8.4).

1847 4.7.2. Applying b-tag scale factor corrections in signal samples

1848 High-statistic **FastSim** signal simulation samples are unavailable for each signal signal
 1849 point, which means that a different procedure to the formula method described in Section
 1850 (4.5) is employed. Furthermore, the use of the **FastSim** framework in the reconstruction
 1851 introduces an extra set of scale-factor corrections, to be applied simultaneously with
 1852 those correcting the full-simulation to the data.

1853 For these signal models, an event-by-event re-weighting procedure is applied. This applied
 1854 weight depends on both the flavour content and the b-tagging status of the reconstruction
 1855 level jets in the event.

1856 The re-weighting procedure can be described by first considering a single jet in an signal
 1857 sample event. The flavour of the jet is determined using the method described in Section
 1858 (4.5.1).

1859 Taking the flavour, p_T and η values of the jet, the expected tagging efficiency, $\epsilon_{MC}(p_T, \eta, f)$,
 1860 in simulation is retrieved from a map of tagging efficiencies determined from the **FullSim**
 1861 **SM** simulation samples, and binned as a function of jet p_T , η and flavour after the
 1862 application of the hadronic signal selection. The binning is chosen to reflect the set of p_T
 1863 and η dependant corrections of simulation to data defined by [84].

1864 The actual tagging efficiency of the **FastSim** jet, $\epsilon_{\text{FastSim}}(p_T, \eta, f)$, differs from that
 1865 measured in **FullSim**, $\epsilon_{MC}(p_T, \eta, f)$ and is related via an additional correction factor,

$$\epsilon_{\text{FastSim}}(p_T, \eta, f) = \frac{\epsilon_{MC}(p_T, \eta, f)}{SF_{\text{Fast} \rightarrow \text{Full}}(p_T, \eta, f)}, \quad (4.14)$$

1866 where $SF_{\text{Fast} \rightarrow \text{Full}}(p_T, \eta, f)$ represents a set of p_T and η dependant corrections determined
 1867 from the ratio between the efficiency and mis-tagging rates of a $t\bar{t}$ **FullSim** and $t\bar{t}$
 1868 **FastSim** sample. The central value for these corrections is the same for all signal samples.
 1869 Similarly the tagging efficiencies measured in data [64], $\epsilon_{Data}(p_T, \eta, f)$, are further related
 1870 to $\epsilon_{\text{FastSim}}(p_T, \eta, f)$ by the equation,

$$\begin{aligned}
\epsilon_{Data}(p_T, \eta, f) &= \epsilon_{MC}(p_T, \eta, f) \times SF_{MC \rightarrow Data}(p_T, \eta, f) \\
&= \epsilon_{FastSim}(p_T, \eta, f) \times \underbrace{SF_{Fast \rightarrow Full}(p_T, \eta, f) \times SF_{MC \rightarrow Data}(p_T, \eta, f)}_{SF_{Fast} \rightarrow Data}.
\end{aligned} \tag{4.15}$$

1871 For each jet, the weight of the event is re-weighted according to whether the jet fires the
1872 b-tagger. In the instance that the jet *is* b-tagged the event weight is modified by,

$$\text{weight} = SF_{Fast \rightarrow Data} \times \text{weight}, \tag{4.16}$$

1873 and in the case that the jet is *not* tagged,

$$\text{weight} = \frac{1 - \epsilon_{Data}(p_T, \eta, f)}{1 - \epsilon_{FastSim}(p_T, \eta, f)} \times \text{weight}. \tag{4.17}$$

1874 Once all events have been reweighted this way, the yields in each n_b^{reco} bin represent the
1875 corrected MC yields.

1876 4.7.3. Experimental uncertainties

1877 The systematic uncertainty on the expected signal acceptance times analysis efficiency is
1878 determined independently for the each **SMS** model considered. These systematics stem
1879 from uncertainties on the parton distribution functions, the luminosity measurement,
1880 jet energy scale, b-tag scale factor measurements and the efficiencies of various cuts used
1881 in the signal selection, including the H_T / E_T , dead **ECAL** cleaning filter and lepton /
1882 photon event vetoes.

1883 Rather than trying to estimate the level of systematic that is applicable point-by-point in
1884 a model space, general behaviours are considered and constant systematics are estimated
1885 in two regions of the **SMS** models parameter space. These two regions are defined as
1886 near to (small mass splittings) and far (large mass splittings) from the diagonal, where
1887 far is realised by the condition

$$m_{\tilde{q}/\tilde{g}} - m_{LSP} > 350 GeV \quad m_{\tilde{q}/\tilde{g}} > 475 GeV.$$

1888 The total systematics in each region are evaluated in the following ways:

1889 **Jet energy scale** : The relative change in the signal efficiency is gauged by varying
1890 the energy of all jets in an event up or down according to a p_T and η dependent jet
1891 energy scale uncertainty. Within the two systematic regions, the resulting systematic
1892 uncertainties for each **SMS** model are determined by taking the value of the 68th
1893 percentile for the distributions of the relative change in the signal efficiency.

1894 **Luminosity measurement** : The measurement of luminosity taken propagates
1895 through to an uncertainty on the signal event yield when considering any new
1896 physics model, which is currently 4.4% [85].

1897 **Parton density function** : The effects of varying the set of parton distribution
1898 functions used and changing the renormalization/factorization scale used to compute
1899 the cross sections by a factor of two up or down have been found to affect the
1900 efficiency by up to 10%.

1901 **H_T/E_T cleaning cut** : The ratio of the efficiencies of the cleaning cut are compared
1902 in simulation and data after application of the $\mu +$ jets control sample selection.
1903 No α_T cut or further event cleaning filters are applied. The ratio of the efficiencies
1904 observed in data and simulation for a cut value of $H_T/E_T < 1.25$ and the two jet
1905 multiplicity bins, $2 \leq n_{jet} \leq 3$ and $n_{jet} \geq 4$ are 1.028 ± 0.007 and 1.038 ± 0.015
1906 respectively. These deviations are taken to represent the systematic uncertainty on
1907 the simulation modelling of this variable.

1908 **Deal ECAL cleaning filter** : The ratio of the efficiencies observed in data and
1909 simulation for this filter in the two jet multiplicity bins, $2 \leq n_{jet} \leq 3$ and $n_{jet} \geq 4$,
1910 are 0.961 ± 0.008 and 0.961 ± 0.009 , respectively. These deviations from unity
1911 are taken to represent the systematic uncertainties in the modelling in simulation of
1912 this filter.

1913 **Lepton and photon vetoes** : The uncertainty on the efficiency of the lepton and
1914 photon vetoes is established by considering the efficiency of the vetoes after applying
1915 filters with identical logic but based on truth information. If the efficiency is not
1916 100%, then this represents the fraction of signal events that should not be vetoed.

This deviation is taken directly as the systematic uncertainty on the efficiency. The systematic uncertainty is only non-zero for models which contain third-generation quarks in the final state.

B-tag scale factor uncertainties : The relative change in the signal efficiency is observed when relevant flavour, p_T and η dependant b-tag correction factors, are varied up or down by their uncertainty. Within the two systematic regions, the resulting systematic uncertainties for each **SMS** model are determined by taking the value of the 68th percentile for the distributions of the relative change in the signal efficiency, over all mass points.

Tables 4.15 and 4.16 summarise all the aforementioned systematic uncertainties on the signal efficiencies for each individual **SMS** model interpreted in the analysis. The systematic uncertainties used for the region near to the diagonal fall in the range 13-15%; similarly, for the region far from the diagonal, the uncertainties used fall in the range 12-23%. These uncertainties are all included in the limit calculation.

Model	Luminosity	p.d.f	JES	H_T/\bar{E}_T	Dead ECAL	Lepton Veto	b-tagging	Total
T1	4.4	10.0	5.6	3.8	4.1	n/a	3.1	13.9
T2	4.4	10.0	4.1	2.8	4.1	n/a	2.4	12.9
T2tt	4.4	10.0	6.5	3.8	4.1	0.8	0.8	13.9
T2bb	4.4	10.0	4.8	2.8	4.1	0.3	2.2	13.1
T1tttt	n/a	n/a	n/a	n/a	n/a	n/a	n/a	n/a
T1bbbb	4.4	10.0	7.3	3.8	4.1	0.5	2.7	14.5

Table 4.15.: Estimates of systematic uncertainties on the signal efficiency (%) for various **SMS** models when considering points in the region near to the diagonal (i.e. small mass splitting and compressed spectra). The uncertainties are added in quadrature to obtain the total.

Model	Luminosity	p.d.f	JES	H_T/\bar{E}_T	Dead ECAL	Lepton Veto	b-tagging	Total
T1	4.4	10.0	0.8	3.8	4.1	n/a	6.6	14.0
T2	4.4	10.0	1.1	2.8	4.1	n/a	5.8	13.4
T2tt	4.4	10.0	3.5	3.8	4.1	0.6	1.6	12.9
T2bb	4.4	10.0	0.9	2.8	4.1	0.3	2.7	12.3
T1tttt	4.4	10.0	0.5	3.8	4.1	1.4	19.4	23.0
T1bbbb	4.4	10.0	1.5	3.8	4.1	0.4	10.1	16.0

Table 4.16.: Estimates of systematic uncertainties on the signal efficiency (%) for various **SMS** models when considering points in the region far from the diagonal (i.e. large mass splitting). The uncertainties are added in quadrature to obtain the total.

1931 4.8. Statistical Framework

1932 For a given category of events satisfying requirements on both n_{jet} and n_b^{reco} , a likelihood
1933 model of the observations in multiple data samples is used to gauge agreement between
1934 the observed yields in the hadronic signal region, and the predicted yields obtained from
1935 the control samples. In addition to checking whether the predictions are compatible with
1936 a **SM** only hypothesis, the likelihood model is also used to test for the presence of a
1937 variety of signal models.

1938 4.8.1. Hadronic sample

1939 Let N be the number of bins on H_T , with n^i the number of events observed satisfying
1940 all selection requirements in each H_T bin i . The likelihood of the observations can then
1941 be written :

$$L_{had} = \prod_i \text{Pois}(n^i | b^i + s^i), \quad (4.18)$$

1942 where b^i represents the expected **SM** background

$$b^i = EWK_i + QCD_i, \quad (4.19)$$

1943 and s^i the expected number of signal events from the different **SMS** models interpreted.
1944 Pois refers to the Poisson distribution of these values and is defined as :

$$\text{Pois}(\chi|\lambda) = \frac{\lambda^\chi \exp^{-\lambda}}{k!}. \quad (4.20)$$

₁₉₄₅ **4.8.2. H_T evolution model**

- ₁₉₄₆ The hypothesis, that for a process the α_T ratio falls exponentially see Section (4.2.4) in H_T is defined by Equation (4.10), where k_{QCD} is constrained by measurements in a signal sideband region.
- ₁₉₄₉ The expected QCD background, QCD^i , within a bin i is then modelled as,

$$QCD^i = m^i A_{QCD} e^{-k_{QCD}\langle H_T \rangle}, \quad (4.21)$$

- ₁₉₅₀ where m_i represent the number of events observed with $\alpha_T \leq 0.55$ in each H_T bin i , and ₁₉₅₁ $\langle H_T \rangle$ represents the mean H_T of each bin. Expressed as functions of just the zeroth bin, ₁₉₅₂ QCD^0 , and k_{QCD} , the QCD expectation is given by

$$QCD^i = QCD^0 \left(\frac{m^i}{m^0} \right) e^{-k_{QCD}(\langle H_T \rangle^i - \langle H_T \rangle^0)}. \quad (4.22)$$

₁₉₅₃ **4.8.3. EWK control samples**

- ₁₉₅₄ The **EWK** background estimation within each bin, i , is broken into two components, the ₁₉₅₅ expected yield from $Z \rightarrow \nu\bar{\nu}$ and $t\bar{t}-W$ (plus other residual backgrounds) events. This is ₁₉₅₆ written as, Z_{inv}^i and $t\bar{t}W^i$, and it follows that

$$EWK^i = Z_{inv}^i + t\bar{t}W^i. \quad (4.23)$$

- ₁₉₅₇ This can be further expressed as

$$Z_{inv}^i \equiv f_{Z_{inv}}^i \times EWK^i, \quad (4.24)$$

$$t\bar{t}W^i \equiv (1 - f_{Z_{inv}}^i) \times EWK^i, \quad (4.25)$$

1958 where f_{Zinv}^i represents the expected yield from $Z \rightarrow \nu\bar{\nu}$ in bin i divided by the expected
1959 **EWK** background EWK^i . This fraction is modelled as a linear component

$$f_{Zinv}^i = f_{Zinv}^0 + \frac{\langle H_T \rangle^i - \langle H_T \rangle^0}{\langle H_T \rangle^{N-1} - \langle H_T \rangle^0} (f_{Zinv}^{N-1} - f_{Zinv}^i), \quad (4.26)$$

1960 where N again represents the number of H_T bins, and f_{Zinv}^i and f_{Zinv}^{N-1} are float parameters
1961 whose final values are limited between zero and one.

1962 Within each H_T bin there are three background measurements for the different control
1963 samples, n_γ^i , n_μ^i and $n_{\mu\mu}^i$, representing the event yields from the $\gamma +$ jets, $\mu +$ jets and
1964 $\mu\mu +$ jets control samples respectively. Each of these have a corresponding yield in
1965 simulation, MC_γ^i , MC_μ^i and $MC_{\mu\mu}^i$. Within the hadronic signal region there are also
1966 corresponding simulated yields for $Z \rightarrow \nu\bar{\nu}$ (MC_{Zinv}^i) and $t\bar{t} + W$ ($MC_{t\bar{t}+W}^i$), which are
1967 used to define

$$r_\gamma^i = \frac{MC_\gamma^i}{MC_{Zinv}^i}; \quad r_{\mu\mu}^i = \frac{MC_{\mu\mu}^i}{MC_{Zinv}^i}; \quad r_\mu^i = \frac{MC_\mu^i}{MC_{t\bar{t}+W}^i}, \quad (4.27)$$

1968 where r_p^i represents the inverse of the **TF**'s used to extrapolate the yield of each background
1969 process.

1970 The likelihoods regarding the three measured yields n_γ^i , $n_{\mu\mu}^i$, n_μ^i can then be fully expressed
1971 as

$$L_\gamma = \prod_i \text{Pois}(n_\gamma^i | \rho_{\gamma Z}^j \cdot r_\gamma^i \cdot Z_{inv}^i), \quad (4.28)$$

$$L_{\mu\mu} = \prod_i \text{Pois}(n_{\mu\mu}^i | \rho_{\mu\mu Z}^j \cdot r_{\mu\mu}^i \cdot Z_{inv}^i), \quad (4.29)$$

$$L_\mu = \prod_i \text{Pois}(n_\mu^i | \rho_{\mu Y}^j \cdot r_\mu^i \cdot Y^i + s_\mu^i), \quad (4.30)$$

$$(4.31)$$

1972 which contain an additional term s_μ^i , which represents the signal contamination in the
1973 $\mu +$ jets sample. The parameters $\rho_{\gamma Z}^j$, $\rho_{\mu\mu}^j$ and ρ_μ^j represent “correction factors” that

1974 accommodate the systematic uncertainties associated with the control sample based
1975 background constraints.

1976 Each of these equations are used to estimate the maximum likelihood value for relevant
1977 background in the signal region given the observations n_p^i in each of the control samples
1978 (see Section (4.2.3)).

1979 The measurements in each of the control samples and the hadronic signal region, along
1980 with the ratios r_γ^i , $r_{\mu\mu}^i$, and r_μ^i , are all considered simultaneously through the relationships
1981 defined by Equations (4.19),(4.24) and (4.25).

1982 In addition to the Poission product, an additional log-normal term is introduced to
1983 accommodate the systematic uncertainties given by,

$$L_{EWK \ syst} = \prod_j \text{Logn}(1.0 | \rho_{\mu W}^j, \sigma_{\mu W}^j) \times \text{Logn}(1.0 | \rho_{\mu\mu Z}^j, \sigma_{\mu\mu Z}^j) \times \text{Logn}(1.0 | \rho_{\gamma Z}^j, \sigma_{\gamma Z}^j), \quad (4.32)$$

1984 where $\sigma_{\gamma Z}^j$, $\sigma_{\mu\mu Z}^j$ and $\sigma_{\mu W}^j$ represent the relative systematic uncertainties for the control
1985 sample constraints and Logn is the log-normal distribution [86],

$$\text{Logn}(x | \mu, \sigma_{rel}) = \frac{1}{x\sqrt{2\pi}\ln k} \exp\left(\frac{\ln^2(\frac{x}{\mu})}{2\ln^2 k}\right); \quad k = 1 + \sigma_{rel}. \quad (4.33)$$

1986 Five parameters per control sample are used to span the eight H_T bins, with just one
1987 used for the three H_T bins in the $n_b^{reco} \geq 4$ category. These parameters span the same
1988 H_T ranges described in Section (4.6) and is shown in Table 4.17.

H_T bin (i)	0	1	2	3	4	5	6	7
syst. parameter (j)	0	1	2	2	3	3	4	4

H_T bin (i)	0	1	2
syst. parameter (j)	0	0	0

Table 4.17.: The systematic parameters used in H_T bins. Left: categories with eight bins;
right: category with three bins.

1989 Alternatively, in the higher n_b^{reco} categories ($n_b^{reco} = 3$, $n_b^{reco} \geq 4$), the single muon sample
1990 is used to constrain the total EWK background. Therefore the likelihood function is
1991 greatly simplified and is represented by

$$L'_\mu = \prod_i \text{Pois}(n_\mu^i | \rho_{\mu Y}^j \cdot r'_\mu \cdot EWK^i + s_\mu^i), \quad (4.34)$$

1992 where,

$$r'_\mu = \frac{MC_\mu^i}{MC_{tot}^i}. \quad (4.35)$$

1993 **4.8.4. Contributions from signal**

1994 The cross section for each model is represented by x and l represents the total recorded
1995 luminosity considered by the analysis in the signal region. Let ϵ_{had}^i and ϵ_μ^i represent the
1996 analysis selection efficiency for that particular signal model in H_T bin i of the hadronic
1997 and $\mu +$ jets control sample respectively. Letting δ represent the relative uncertainty on
1998 the signal yield, assumed to be fully correlated across all bins, and ρ_{sig} the “correction
1999 factor” to the signal yield which accommodates this uncertainty. f represents an unknown
2000 multiplicative factor on the signal cross section, for which an allowed interval is computed.

2001 The expected signal yield s^i is thus given by

$$s^i \equiv f \rho_{sig} x l \epsilon_{had}^i \quad (4.36)$$

2002 and signal contamination with the $\mu +$ jets control sample by

$$s_\mu^i \equiv f \rho_{sig} x l \epsilon_\mu^i \quad (4.37)$$

2003 The systematic uncertainty on the signal is additionally included by the term

$$L_{sig} = \text{Logn}(1.0 | \rho_{sig}, \delta). \quad (4.38)$$

2004 A discussion of the **SMS** signal models through which the analysis is interpreted can be
2005 found in the following Chapter.

2006 **4.8.5. Total likelihood**

2007 The total likelihood function for a given signal bin $k(n_b^{reco}, n_{jet})$ is given by the product
2008 of the likelihood functions introduced within the previous sections:

$$L^k = L_{had}^k \times L_\mu^k \times L_\gamma^k \times L_{\mu\mu}^k \times L_{EWKsyst}^k \times L_{QCD}^k. \quad (4.39)$$

2009 In categories containing eight H_T bins and utilising the three control samples ($\mu + \text{jets}, \mu\mu + \text{jets}, \gamma + \text{jets}$), there are 25 nuisance parameters, whilst when just one control sample is
2010 used to estimate the **EWK** background, there are 15 nuisance parameters. Where three
2011 H_T bins are used (the highest n_b^{reco} category), there are 6 nuisance parameters. This
2012 information is summarised within Table 4.18.
2013

Nuisance parameter	Total
$(EWK^i)_{i:0-7(2)}$	8 (3)
f_{Zinv}^0 *	1
f_{Zinv}^7 *	1
QCD^0	1
k_{QCD}	1
$(\rho_{\gamma Z}^j)_{j:2-4}$ *	3
$(\rho_{\mu\mu Z}^j)_{j:0-4}$ *	5
$(\rho_{\mu W}^j)_{j:0-4(0)}$	5 (1)

Table 4.18.: Nuisance parameters used within the different hadronic signal bins of the analysis. Parameters denoted by a * are not considered in the case of a single control sample being used to predict the **EWK** background. Numbers within brackets highlight the number of nuisance parameters in the case of three H_T bins being used.

2014 When considering **SUSY** signal models within the likelihood, an additional parameter is
2015 introduced, ρ_{sig} . When multiple categories are fit simultaneously the total likelihood is
2016 then represented by

$$L = L_{sig} \times \prod_k L_{had}^k \times L_\mu^k \times L_\gamma^k \times L_{\mu\mu}^k \times L_{EWKsyst}^k \times L_{QCD}^k. \quad (4.40)$$

Chapter 5.

²⁰¹⁷ Results and Interpretation

²⁰¹⁸ Using the statistical framework outlined in the previous chapter, results are compared to
²⁰¹⁹ a **SM**-only hypothesis (Section (5.1)) and interpreted using various **SMS** models (Section
²⁰²⁰ (5.2)).

²⁰²¹ 5.1. Standard Model

²⁰²² The **SM** background only hypothesis is tested by removing any signal contributions
²⁰²³ within the signal and control samples, and the likelihood function is maximised over all
²⁰²⁴ parameters using Rootfit [87] and MINUIT [88]. The results of the search consist of the
²⁰²⁵ observed yields in the hadronic signal sample, and the $\mu + \text{jets}$, $\mu\mu + \text{jets}$ and $\gamma + \text{jets}$
²⁰²⁶ control samples.

²⁰²⁷ These observed yields along with the expectations and uncertainties given by the simulta-
²⁰²⁸ neous fit for the hadronic signal region are given in Table 5.2. The results obtained from
²⁰²⁹ the simultaneous fits, including that of the three control samples, are shown in Figure
²⁰³⁰ 5.1-5.8, as summarised in Table 5.1.

²⁰³¹ The figures show a comparison between the observed yields and the **SM** expectations
²⁰³² across all H_T bins, for events in both n_{jet} and n_b^{reco} multiplicity categories. In all categories
²⁰³³ the samples are well described by the **SM** only hypothesis. In particular no significant
²⁰³⁴ excess is observed above **SM** expectation within the hadronic signal region.

n_{jet}	n_b^{reco}	Control samples fitted	Figure
2-3	0	$\mu + \text{jets}, \mu\mu + \text{jets}, \gamma + \text{jets}$	5.1
2-3	1	$\mu + \text{jets}, \mu\mu + \text{jets}, \gamma + \text{jets}$	5.2
2-3	1	$\mu + \text{jets}$	5.3
≥ 4	0	$\mu + \text{jets}, \mu\mu + \text{jets}, \gamma + \text{jets}$	5.4
≥ 4	1	$\mu + \text{jets}, \mu\mu + \text{jets}, \gamma + \text{jets}$	5.5
≥ 4	2	$\mu + \text{jets}$	5.6
≥ 4	3	$\mu + \text{jets}$	5.7
≥ 4	4	$\mu + \text{jets}$	5.8

Table 5.1.: Summary of control samples used by each fit results, and the Figures in which they are displayed.

Cat	n_b^{reco}	n_{jet}	H_T bin (GeV)							
			275-325	325-375	375-475	474-575	575-675	675-775	775-875	875- ∞
SM Data	0	≤ 3	6235^{+100}_{-67}	2900^{+60}_{-54}	1955^{+34}_{-39}	558^{+14}_{-15}	186^{+11}_{-10}	$51.3^{+3.4}_{-3.8}$	$21.2^{+2.3}_{-2.2}$	$16.1^{+1.7}_{-1.7}$
			6232	2904	1965	552	177	58	16	25
SM Data	0	≥ 4	1010^{+34}_{-24}	447^{+19}_{-16}	390^{+19}_{-15}	250^{+12}_{-11}	111^{+9}_{-7}	$53.3^{+4.3}_{-4.3}$	$18.5^{+2.4}_{-2.4}$	$19.4^{+2.5}_{-2.7}$
			1009	452	375	274	113	56	16	27
SM Data	1	≤ 3	1162^{+37}_{-29}	481^{+18}_{-19}	341^{+15}_{-16}	$86.7^{+4.2}_{-5.6}$	$24.8^{+2.8}_{-2.7}$	$7.2^{+1.1}_{-1.0}$	$3.3^{+0.7}_{-0.7}$	$2.1^{+0.5}_{-0.5}$
			1164	473	329	95	23	8	4	1
SM Data	1	≥ 4	521^{+25}_{-17}	232^{+15}_{-12}	188^{+12}_{-11}	106^{+6}_{-6}	$42.1^{+4.1}_{-4.4}$	$17.9^{+2.2}_{-2.0}$	$9.8^{+1.5}_{-1.4}$	$6.8^{+1.2}_{-1.1}$
			515	236	204	92	51	13	13	6
SM Data	2	≤ 3	224^{+15}_{-14}	$98.2^{+8.4}_{-6.4}$	$59.0^{+5.2}_{-6.0}$	$12.8^{+1.6}_{-1.6}$	$3.0^{+0.9}_{-0.7}$	$0.5^{+0.2}_{-0.2}$	$0.1^{+0.1}_{-0.1}$	$0.1^{+0.1}_{-0.1}$
			222	107	58	12	5	1	0	0
SM Data	2	≥ 4	208^{+17}_{-9}	103^{+9}_{-7}	$85.9^{+7.2}_{-6.9}$	$51.7^{+4.6}_{-4.7}$	$19.9^{+3.4}_{-3.0}$	$6.8^{+1.2}_{-1.3}$	$1.7^{+0.7}_{-0.4}$	$1.3^{+0.4}_{-0.3}$
			204	107	84	59	24	5	1	2
SM Data	3	≥ 4	$25.3^{+5.0}_{-4.2}$	$11.7^{+1.7}_{-1.8}$	$6.7^{+1.4}_{-1.2}$	$3.9^{+0.8}_{-0.8}$	$2.3^{+0.6}_{-0.6}$	$1.2^{+0.3}_{-0.4}$	$0.3^{+0.2}_{-0.1}$	$0.1^{+0.1}_{-0.1}$
			25	13	4	2	2	3	0	0
SM Data	4	≥ 4	$0.9^{+0.4}_{-0.7}$	$0.3^{+0.2}_{-0.2}$				$0.6^{+0.3}_{-0.3}$		
			1	1				3		

Table 5.2.: Comparison of the measured yields in the each H_T , n_{jet} and n_b^{reco} jet multiplicity bins for the hadronic sample with the SM expectations and combined statistical and systematic uncertainties given by the simultaneous fit.

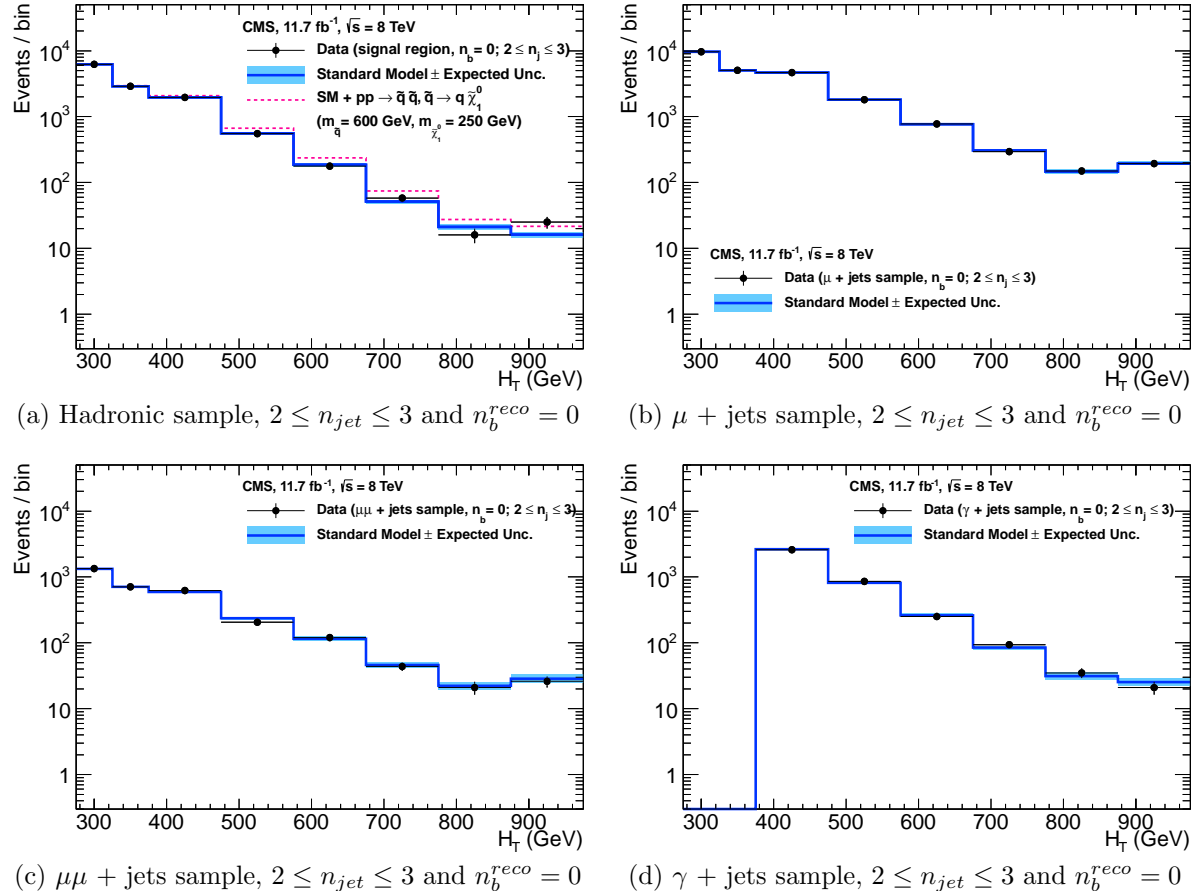


Figure 5.1.: Comparison of the observed yields and SM expectations given by the simultaneous fit in bins of H_T for the (a) hadronic, (b) $\mu +$ jets, (c) $\mu\mu +$ jets and (d) $\gamma +$ jets samples when requiring $n_b^{reco} = 0$ and $n_{jet} \leq 3$. The observed event yields in data (black dots) and the expectations and their uncertainties for all SM processes (blue line with light blue bands) are shown. An example signal expectation (red solid line) for the D1 SMS signal point from Table 4.1 is superimposed on the SM background expectation.

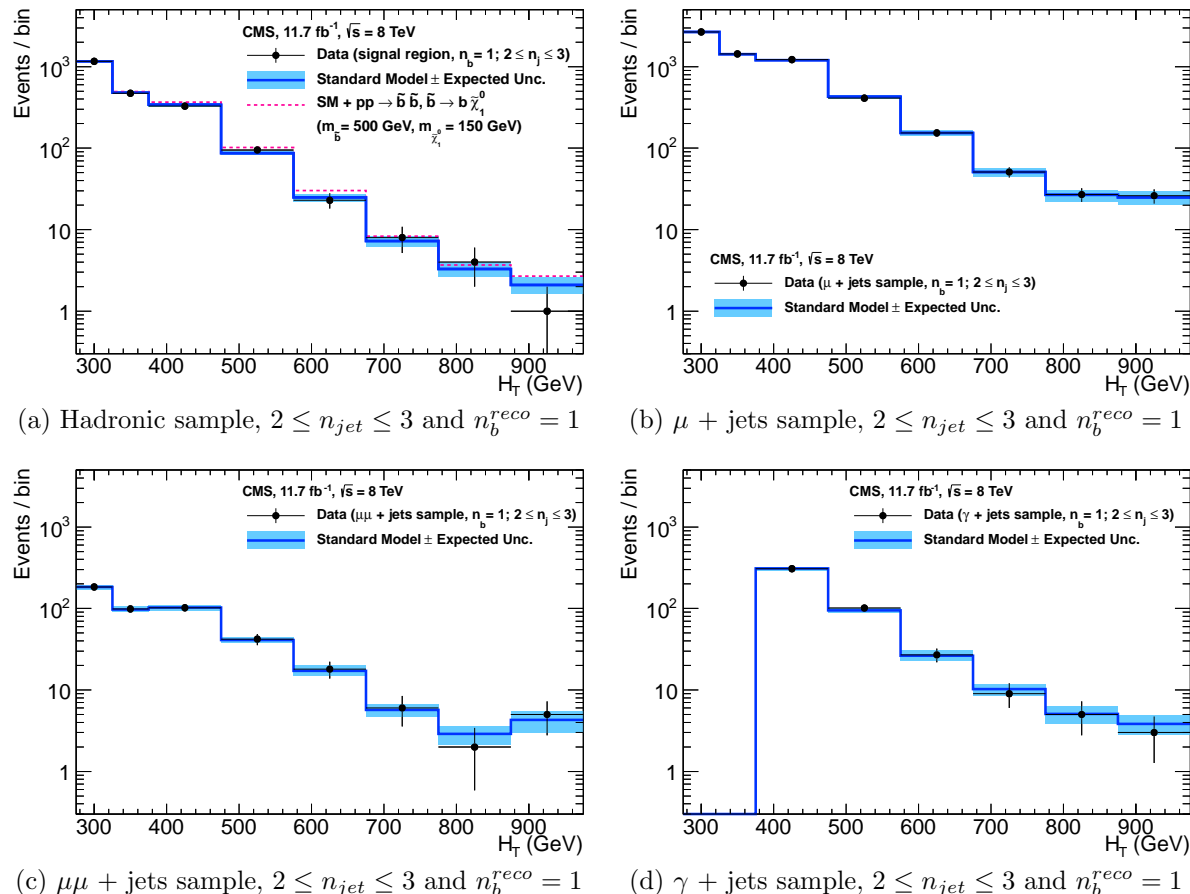


Figure 5.2.: Comparison of the observed yields and SM expectations given by the simultaneous fit in bins of H_T for the (a) hadronic, (b) $\mu +$ jets, (c) $\mu\mu +$ jets and (d) $\gamma +$ jets samples when requiring $n_b^{reco} = 1$ and $n_{jet} \leq 3$. The observed event yields in data (black dots) and the expectations and their uncertainties for all SM processes (blue line with light blue bands) are shown. An example signal expectation (red solid line) for the D2 SMS signal point from Table 4.1 is superimposed on the SM background expectation.

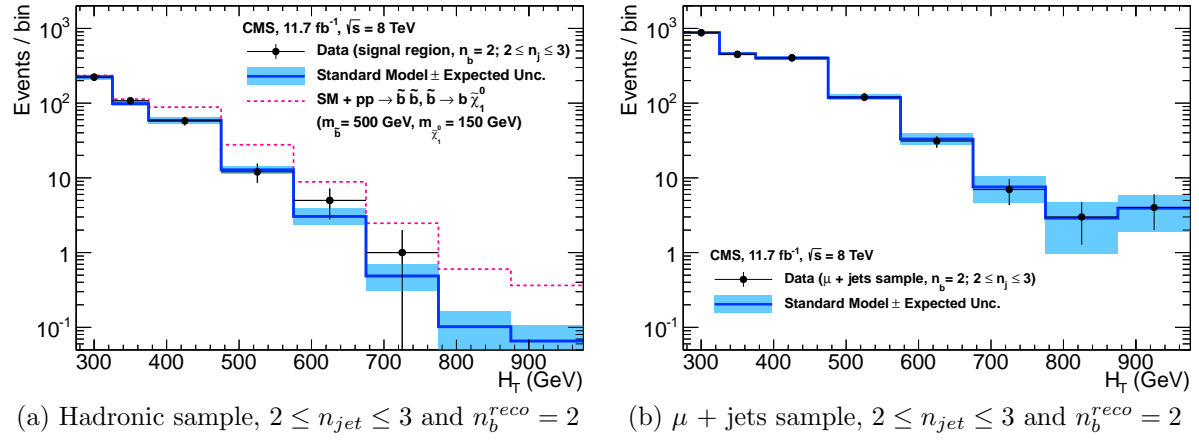


Figure 5.3.: Comparison of the observed yields and SM expectations given by the simultaneous fit in bins of H_T for the (a) hadronic, (b) $\mu + \text{jets}$, (c) $\mu\mu + \text{jets}$ and (d) $\gamma + \text{jets}$ samples when requiring $n_b^{reco} = 2$ and $n_{jet} \leq 3$. The observed event yields in data (black dots) and the expectations and their uncertainties for all SM processes (blue line with light blue bands) are shown. An example signal expectation (red solid line) for the D2 SMS signal point from Table 4.1 is superimposed on the SM background expectation.

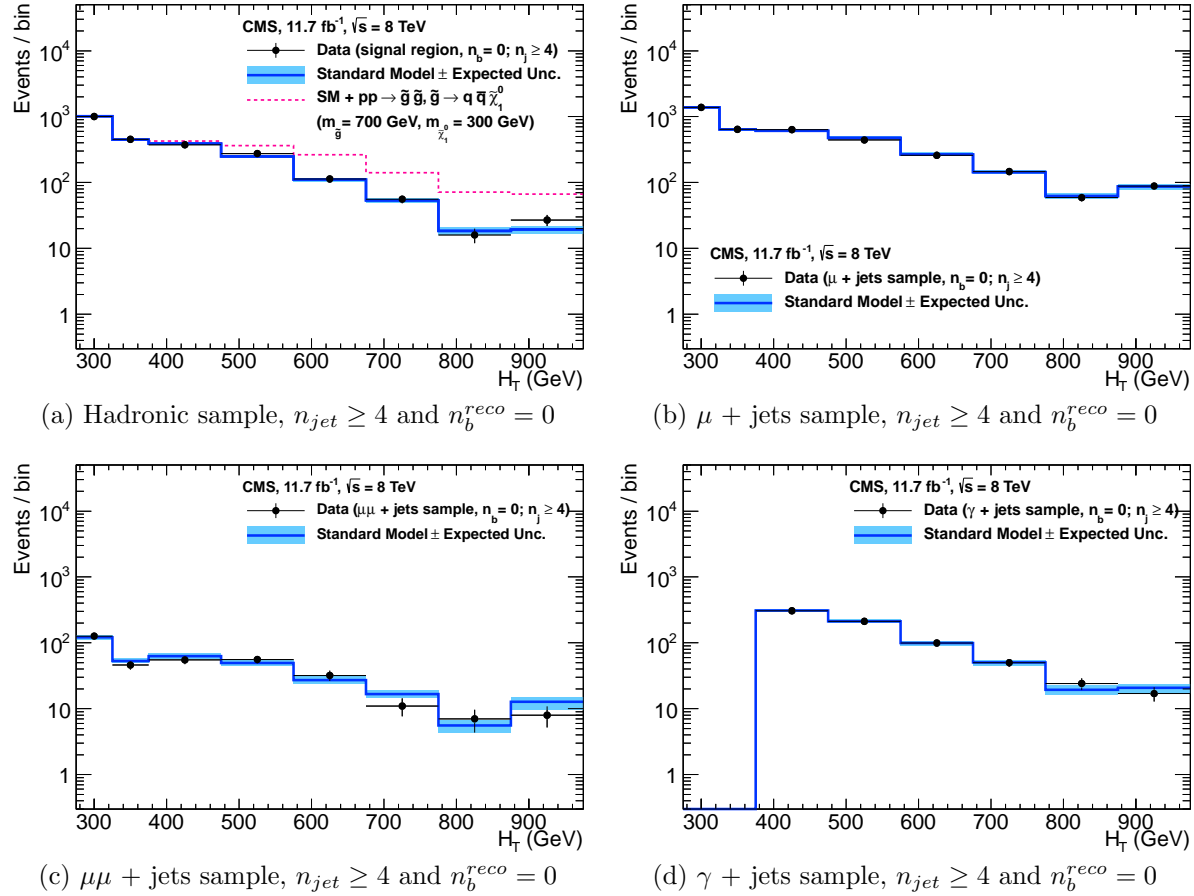


Figure 5.4.: Comparison of the observed yields and SM expectations given by the simultaneous fit in bins of H_T for the (a) hadronic, (b) $\mu +$ jets, (c) $\mu\mu +$ jets and (d) $\gamma +$ jets samples when requiring $n_b^{reco} = 0$ and $n_{jet} \geq 4$. The observed event yields in data (black dots) and the expectations and their uncertainties for all SM processes (blue line with light blue bands) are shown. An example signal expectation (red solid line) for the D2 SMS signal point from Table 4.1 is superimposed on the SM background expectation.

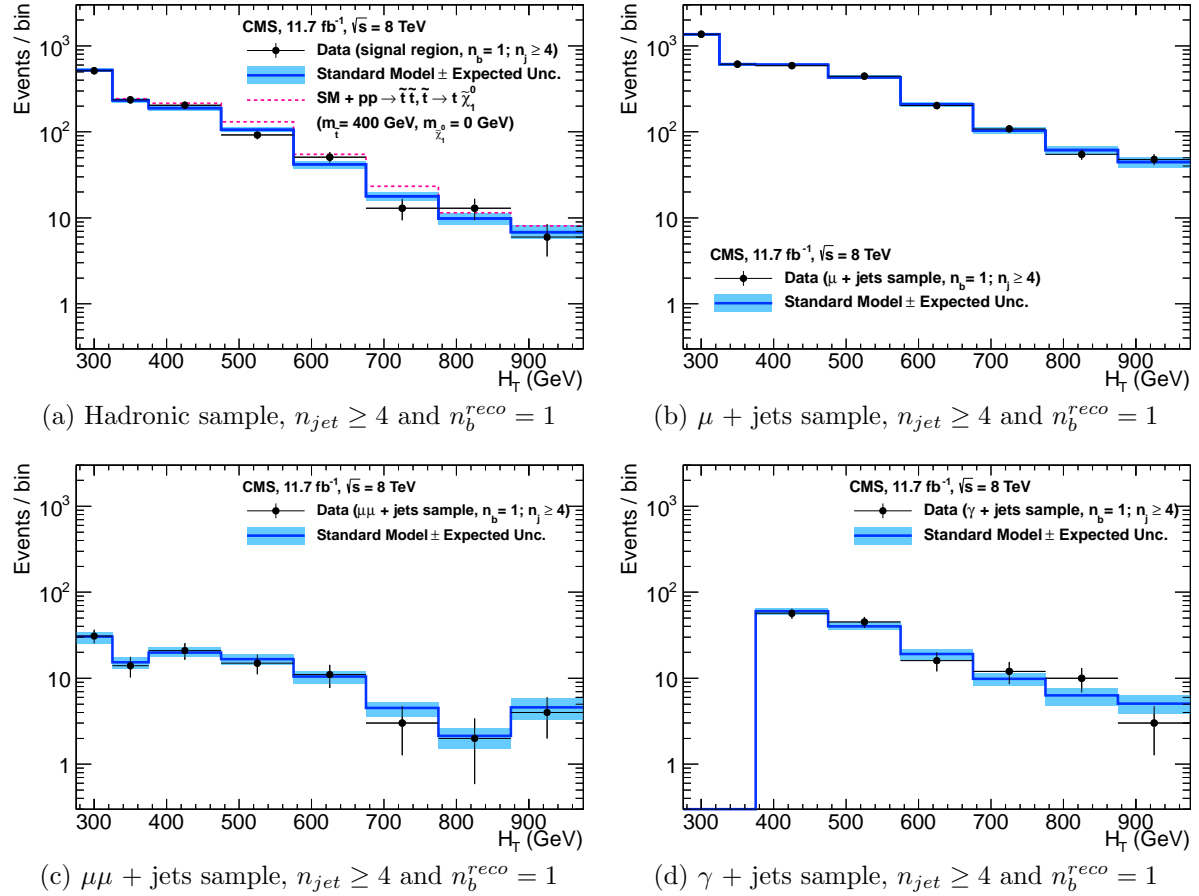


Figure 5.5.: Comparison of the observed yields and SM expectations given by the simultaneous fit in bins of H_T for the (a) hadronic, (b) $\mu +$ jets, (c) $\mu\mu +$ jets and (d) $\gamma +$ jets samples when requiring $n_b^{reco} = 1$ and $n_{jet} \geq 4$. The observed event yields in data (black dots) and the expectations and their uncertainties for all SM processes (blue line with light blue bands) are shown.

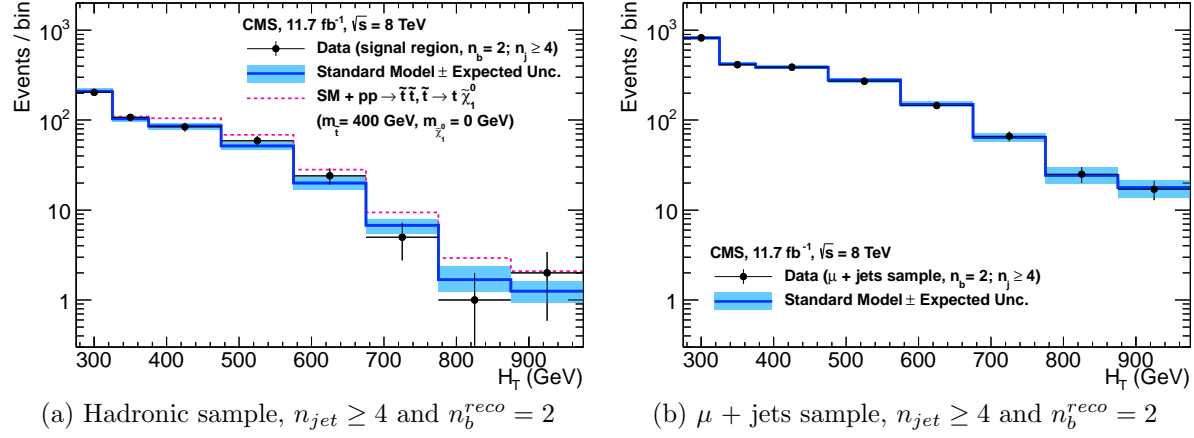


Figure 5.6.: Comparison of the observed yields and SM expectations given by the simultaneous fit in bins of H_T for the (a) hadronic, (b) $\mu +$ jets, (c) $\mu\mu +$ jets and (d) $\gamma +$ jets samples when requiring $n_b^{reco} = 2$ and $n_{jet} \geq 4$. The observed event yields in data (black dots) and the expectations and their uncertainties for all SM processes (blue line with light blue bands) are shown. An example signal expectation (red solid line) for the D3 SMS signal point from Table 4.1 is superimposed on the SM background expectation.

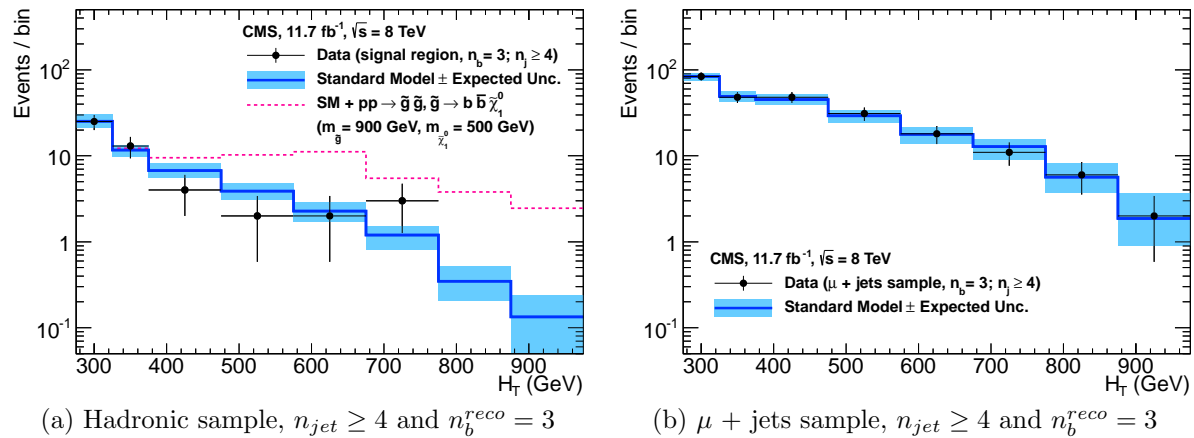


Figure 5.7.: Comparison of the observed yields and SM expectations given by the simultaneous fit in bins of H_T for the (a) hadronic, (b) $\mu +$ jets, (c) $\mu\mu +$ jets and (d) $\gamma +$ jets samples when requiring $n_b^{reco} = 3$ and $n_{jet} \geq 4$. The observed event yields in data (black dots) and the expectations and their uncertainties for all SM processes (blue line with light blue bands) are shown. An example signal expectation (red solid line) for the G2 SMS signal point from Table 4.1 is superimposed on the SM background expectation.

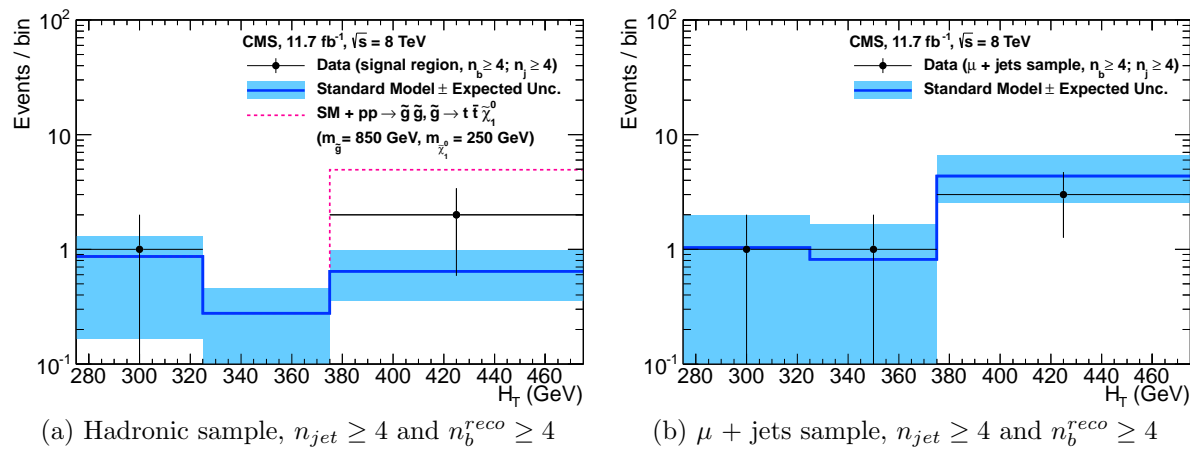


Figure 5.8.: Comparison of the observed yields and SM expectations given by the simultaneous fit in bins of H_T for the (a) hadronic, (b) $\mu +$ jets, (c) $\mu\mu +$ jets and (d) $\gamma +$ jets samples when requiring $n_b^{reco} \geq 4$ and $n_{jet} \geq 4$. The observed event yields in data (black dots) and the expectations and their uncertainties for all SM processes (blue line with light blue bands) are shown. An example signal expectation (red solid line) for the G3 SMS signal point from Table 4.1 is superimposed on the SM background expectation.

2035 **5.2. SUSY**

2036 Limits are set in the parameter space of a set of **SMS** models that characterise both
2037 natural **SUSY** third generation squark production, and compressed spectra where the
2038 mass splitting between the particle and **LSP** is small, leading to soft final state jets.
2039 However as detailed in Section (2.4.1), the individual models are not representative of a
2040 real physical **SUSY** model as only one decay process is considered. Instead these models
2041 represent a way to test for signs of specific signatures indicating new physics.

2042 **5.2.1. The CL_s method**

2043 The CL_s method [89][90][91] is used to compute the limits for signal models, with the
2044 one-sided profile likelihood ratio as the test statistic [92].

The test statistic is defined as

$$q(\mu) = \begin{cases} -2\log\lambda(\mu) & \text{when } \mu \geq \hat{\mu}, \\ 0 & \text{otherwise.} \end{cases} \quad (5.1)$$

2045 where

$$\lambda(\mu) = \frac{L(\mu, \theta_\mu)}{L(\hat{\mu}, \hat{\theta})} \quad (5.2)$$

2046 represents the profile likelihood ratio, in which $\mu \equiv f$ from Section (4.8.4), is the
2047 parameter characterising the signal strength. $\hat{\mu}$ is defined at the maximum likelihood
2048 value, $\hat{\theta}$ the set of maximum likelihood values of the nuisance parameters and θ_μ the set
2049 of maximum values of the nuisance parameters for a given value of μ .

2050 When $\mu \equiv f = 1$, the signal model is considered at its nominal production cross section.
2051 The distribution of q_μ is built up via the generation of pseudo experiments in order to
2052 obtain two distributions for the background (B) and signal plus background (S+B) cases.

2053 The compatibility of a signal model with observations in data is determined by the
2054 parameter CL_s ,

$$\text{CL}_S = \frac{\text{CL}_{S+B}}{\text{CL}_B}, \quad (5.3)$$

with CL_B and CL_{S+B} defined as one minus the quantiles of the observed value in the data of the two distributions. A model is considered to be excluded at 95% confidence level when $\text{CL}_s \leq 0.05$ [93].

5.2.2. Interpretation in simplified signal models

Different n_{jet} and n_b^{reco} bins are used in the interpretation of different **SMS** models. The choice of the categories used are made to increase sensitivity to that particular type of final state signature. The production and decay modes of the **SMS** models under consideration are summarised in Table 5.3, with limit plots of the experimental reach in these models shown in Figure 5.10.

The models T1 and T2 are used to characterise the pair production of gluinos and first or second generation squarks, respectively, with parameters for the sparticle mass as well as on the **LSP** mass. The simplified models T2bb, T1tttt, and T1bbbb describe various production and decay mechanisms in the context of third-generation squarks.

Model	Production/decay	n_{jet}	n_b^{reco}	Process	Limit	$m_{\tilde{q}/\tilde{g}}^{\text{best}}$ (GeV)	$m_{\text{LSP}}^{\text{best}}$ (GeV)
T1	$pp \rightarrow \tilde{g}\tilde{g}^* \rightarrow q\bar{q}\tilde{\chi}_1^0 q\bar{q}\tilde{\chi}_1^0$	≥ 4	0	5.9(a)	5.10(a)	~ 950	~ 450
T2	$pp \rightarrow \tilde{q}\tilde{q}^* \rightarrow q\tilde{\chi}_1^0 \bar{q}\tilde{\chi}_1^0$	≤ 3	0	5.9(b)	5.10(b)	~ 775	~ 325
T2bb	$pp \rightarrow \tilde{b}\tilde{b}^* \rightarrow b\tilde{\chi}_1^0 \bar{b}\tilde{\chi}_1^0$	≤ 3	1,2	5.9(c)	5.10(c)	~ 600	~ 200
T1tttt	$pp \rightarrow \tilde{g}\tilde{g}^* \rightarrow t\bar{t}\tilde{\chi}_1^0 t\bar{t}\tilde{\chi}_1^0$	≥ 4	$2,3,\geq 4$	5.9(d)	5.10(d)	~ 975	~ 325
T1bbbb	$pp \rightarrow \tilde{b}\tilde{b}^* \rightarrow b\tilde{b}\tilde{\chi}_1^0 b\tilde{b}\tilde{\chi}_1^0$	≥ 4	$2,3,\geq 4$	5.9(e)	5.10(e)	~ 1125	~ 650

Table 5.3.: A table representing the **SMS** models interpreted within the analysis. The model name and production and decay chain is specified in the first two columns. Each **SMS** model is interpreted in specific n_{jet} and n_b^{reco} categories which are detailed in the third and fourth columns. The last two columns indicate the search sensitivity for each model, representing the largest $m_{\tilde{q}/\tilde{g}}$ mass beyond which no limit can be set for this particular decay topology. The quotes values are conservatively determined from the observed exclusion based on the theoretical production cross section minus 1σ uncertainty.

Experimental uncertainties on the **SM** background predictions (10 – 30%, Section (4.6.1)), the luminosity measurement (4.4%), and the total acceptance times efficiency of the selection for the considered signal model (12 – 18%, Section (4.7)) are included in the calculation of the limit.

2072 Signal efficiency in the kinematic region defined by $0 < m_{\tilde{g}(\tilde{q})} < 175$ GeV or $m_{\tilde{g}(\tilde{q})} < 300$
2073 GeV is strongly affected by the presence of Initial State Radiation (**ISR**). This region in
2074 which direct (i.e., non-**ISR** induced) production is kinematically forbidden due to the H_T
2075 > 275 GeV requirement, therefore a large percentage of signal acceptance is due to the
2076 effect of **ISR** jets. Given the large associated uncertainties, no interpretation is provided
2077 for this kinematic region.

2078 The estimates on mass limits shown in Table 5.3, are determined conservatively from
2079 the observed exclusion based on the theoretical production cross section, minus 1σ
2080 uncertainty. The most stringent mass limits on pair-produced sparticles are obtained at
2081 low **LSP** masses, while the limits typically weaken for compressed spectra points close to
2082 the diagonal. In particular, for all of the considered **SMS** models, there is an **LSP** mass
2083 beyond which no limit can be set, which can be observed from the figures referenced in the
2084 table.

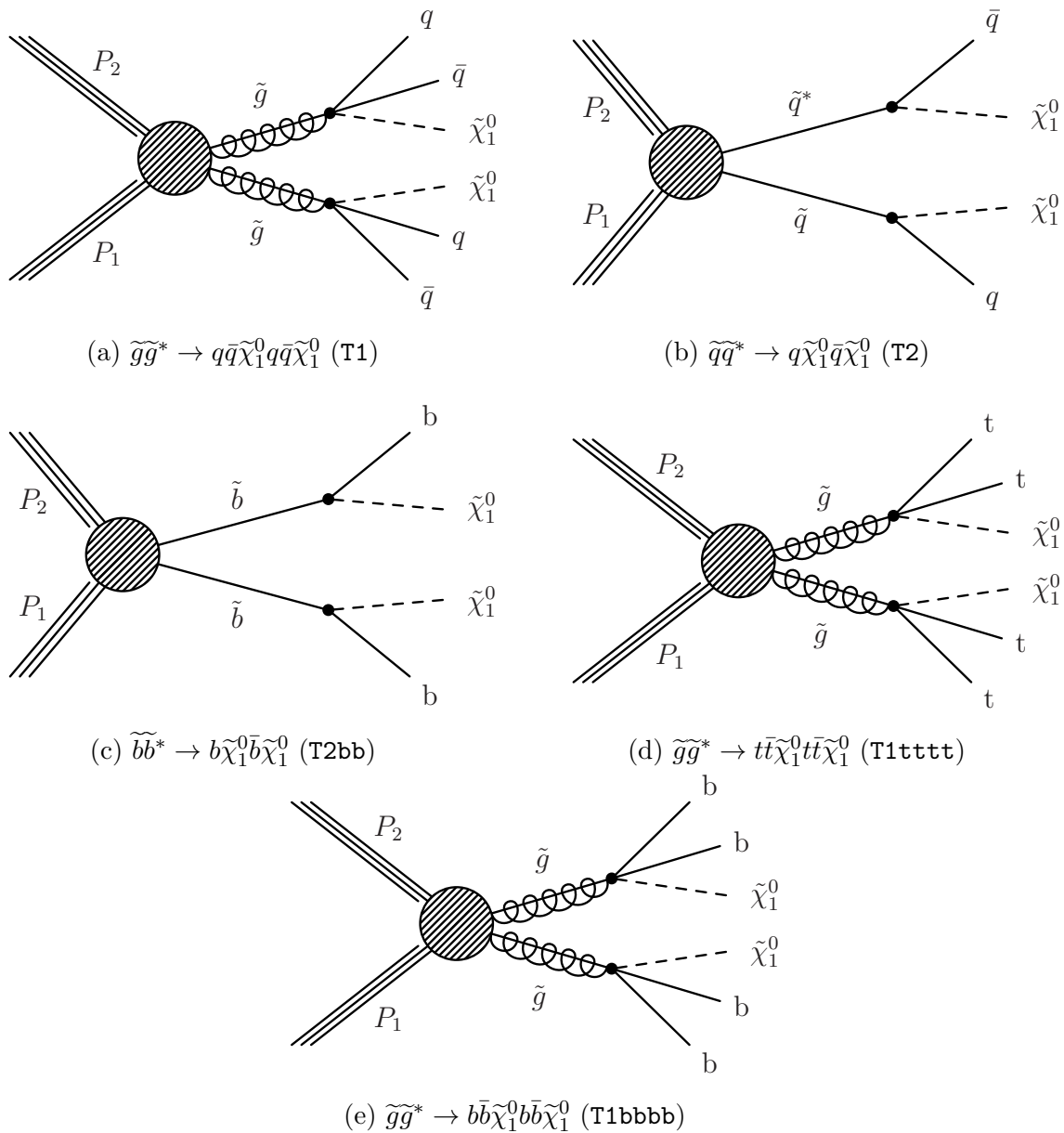


Figure 5.9.: Production and decay modes for the various **SMS** models interpreted within the analysis.

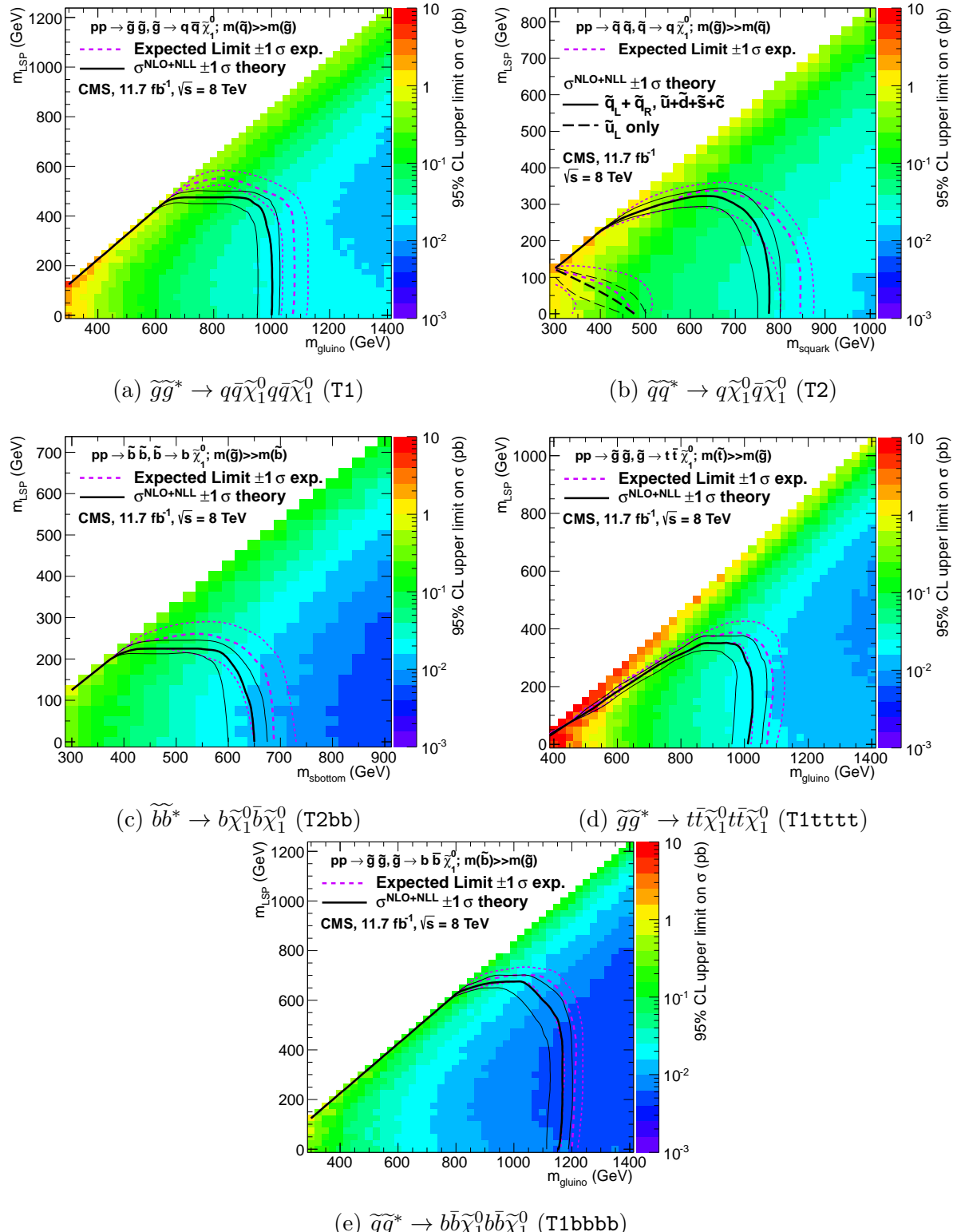


Figure 5.10.: Upper limit of cross section at 95% CL as a function of $m_{\tilde{q}/\tilde{g}}$ and m_{LSP} for various SMS models. The solid thick black line indicates the observed exclusion region assuming NLO and NLL SUSY production cross section. The analysis selection efficiency is measured for each interpreted model, with the signal yield per point given by $\epsilon \times \sigma$. The thin black lines represent the observed excluded region when varying the cross section by its theoretical uncertainty. The dashed purple lines indicate the median (thick line) 1σ (thin lines) expected exclusion regions.

Chapter 6.

2085 Searches For Natural SUSY With 2086 B-tag Templates.

2087 Within this chapter a complimentary technique is discussed as a means to predict the
2088 distribution of three and four reconstructed b-quark jets in an event. The recent discovery
2089 of the Higgs boson has made third-generation “Natural SUSY” models attractive, given
2090 that light top and bottom squarks are a candidate to stabilise divergent loop corrections
2091 to the Higgs boson mass.

2092 Using the α_T search as a base, a simple templated fit is employed to estimate the
2093 SM background in higher b-tag multiplicities (3-4) from a region of a low number of
2094 reconstructed b-jets (0-2). As a proof-of-concept, the procedure after being shown to
2095 close in simulation, is applied to the SM enriched $\mu + \text{jets}$ control sample of the α_T
2096 all-hadronic search detailed in Chapter 4. To highlight the relative insensitivity of the
2097 choice of the b-tagging algorithm working points in the effectiveness of the procedure,
2098 results are presented using the CSV tagger (introduced in Section (3.3.2)) for the “Loose”,
2099 “Medium” and “Tight” working points.

2100 6.1. Concept

2101 The dominant SM backgrounds most SUSY searches are typically $t\bar{t} + \text{jets}$, $W + \text{jets}$ and
2102 $Z \rightarrow \nu\bar{\nu} + \text{jets}$. These process are characterised by typically having zero or two underlying
2103 b-quarks per event. The first step in this approach is to categorise two templates to be
2104 fitted to the low n_b^{reco} multiplicity in terms of these underlying b-quark event topologies :

2105 Z0 - W + jets, Z $\rightarrow \nu\bar{\nu}$ + jets, DY + jets

2106 Z2 - $t\bar{t}$, single top

2107 where Z0 and Z2 represent processes which have an underlying b-quark content of zero
2108 or two respectively.

2109 Both these templates can be generated through the application of the relevant event
2110 selection and taking the underlying n_b^{reco} distribution directly from simulation. However
2111 as discussed within Section (4.5), there are large uncertainties for high n_b^{reco} multiplicities
2112 due to limited MC statistics. This is particularly prominent for the Z0 templates, where
2113 the number of reconstructed b-tags is driven primarily by the light-quark mis-tagging
2114 rate. Therefore to improve the statistical precision of the predictions the formula method,
2115 introduced in Section (4.5.1) is used.

2116 The generation of these templates is then dependant upon the jet-flavour content and
2117 b-tagging rate within the phase space of interest, with the tagging probabilities of a jet
2118 being a function of the jet p_T , the pseudo-rapidity $|\eta|$, and the jet-flavour. This can be
2119 observed in Figure 6.1, where the b-tagging / c-quark mis-tagging / light mis-tagging
2120 efficiency for the three working points of the CSV tagger is shown as a function of jet p_T .

2121 Before the templates are generated, the relevant jet p_T and η corrections are applied to
2122 correct simulation to data, as specified in Section (4.5.3), to then determine the average
2123 tagging rates per analysis bin.

2124 These two templates are then fit to data in the low n_b^{reco} region (0-2). The fit result is
2125 used, along with the knowledge of the template shapes, to extrapolate an estimate to the
2126 high n_b^{reco} signal region (3,4), which is then compared to what is observed in data.

2127 This method can, in principle, be applied to any analysis where the signal hypothesis
2128 has a larger underlying b-quark spectra than the SM backgrounds, as it solely relies on
2129 fitting to the shape of the n_b^{reco} distribution.

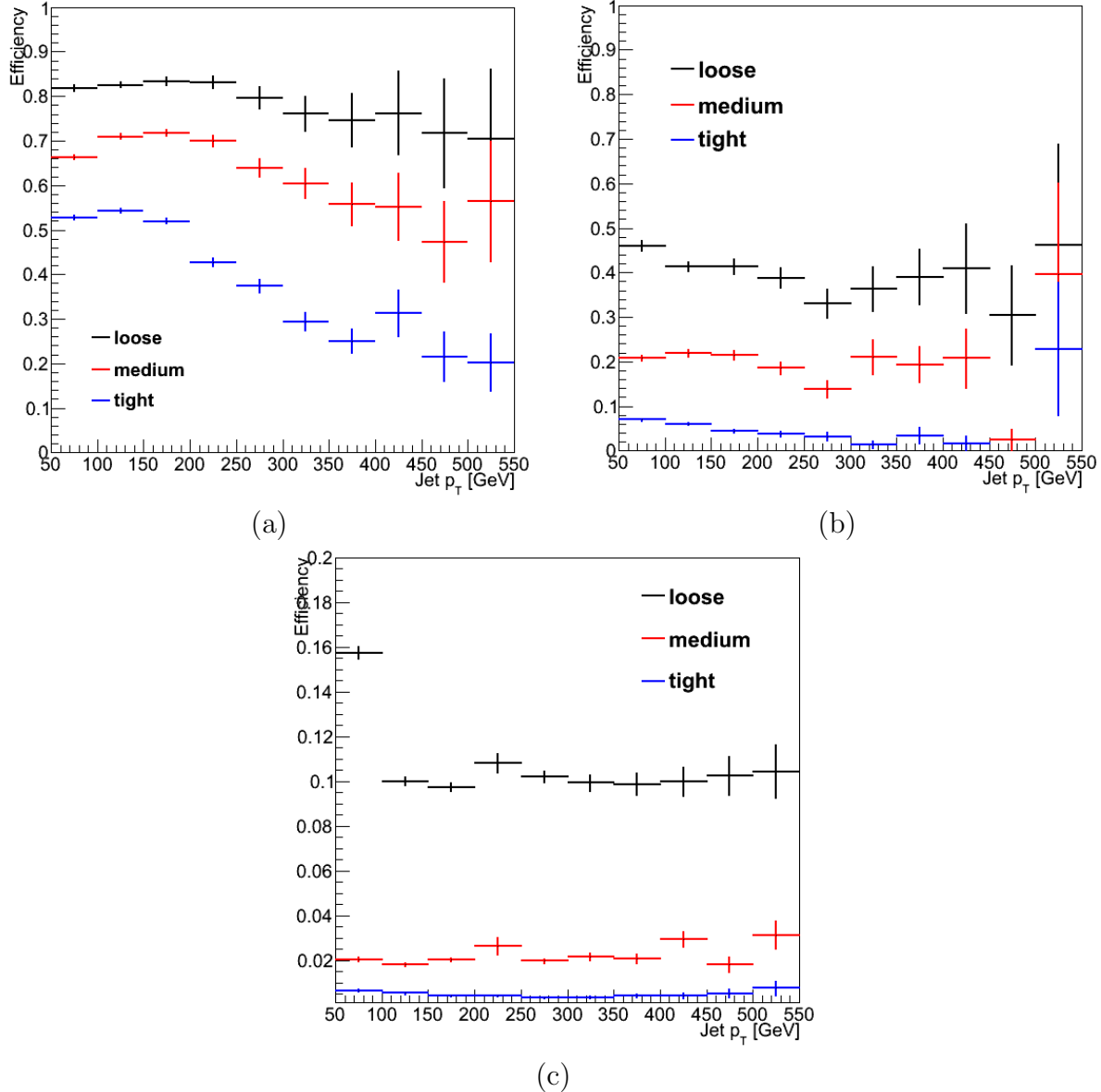


Figure 6.1.: The b-tagging (a), c-quark mis-tagging (b), and light-quark mis-tagging rate (c) as measured in simulation after the α_T analysis, $\mu + \text{jets}$ control sample selection in the region $H_T > 375$.

2130 6.2. Application to the α_T Search

2131 As detailed in the previous chapter, the α_T analysis is a search for **SUSY** particles
 2132 in all-hadronic final states, utilising the kinematic variable α_T to suppress QCD to a
 2133 negligible level. **SM** enriched control samples are used to estimate the background within
 2134 an all-hadronic signal region.

2135 The selection for the $\mu +$ jets control samples defined in Section (4.2.3) is used to
 2136 demonstrate the template fitting procedure both conceptually in simulation, and also
 2137 when applied in data. This is chosen, as such a selection is dominated by events stemming
 2138 from the SM processes with little or no signal contamination from potential new physics..

2139 Neither are contributions from rate SM processes with a higher underlying b-quark
 2140 content (e.g. $t\bar{t}bb$) expected. For these reasons, there is a degree of confidence that the
 2141 procedure should close when applied to this phase space.

2142 The analysis presented here is binning in source jet multiplicity bins, of 3,4 and ≥ 5
 2143 reconstructed jets per event (di-jet events are not included as there is no contribution
 2144 to the high n_b^{reco} region (3,4)) , in order to reduce the kinematic jet p_T dependence.
 2145 Furthermore the analysis is split into three H_T regions,

2146 • 275-325 GeV

2147 • 325-375 GeV

2148 • > 375 GeV

2149 contrary to the eight used within the α_T analysis. Templates for both underlying b-quark
 2150 content hypotheses are then generated for the nine defined analysis bins.

2151 6.2.1. Proof of principle in simulation

2152 In order to demonstrate that the template procedure produces accurate predictions
 2153 within simulation, the simulation samples in the analysis are firstly split into two to allow
 2154 for statistically independent fits to be performed.

2155 By combining the relevant ingredients necessary to employ the formula method, n_b^{reco}
 2156 templates for $Z = 0$ and $Z= 2$ are generated individually for each n_{jet} and H_T bin using
 2157 one half of each simulation sample. A fit of these two templates is then performed in the
 2158 low n_b^{reco} (0-2) region, back to the sum of the other halves of each simulation sample in
 2159 order to check that the relevant information can be recovered in the n_b^{reco} signal region
 2160 (3-4).

2161 The fits are performed independently within each of the defined analysis bins to reduce the
 2162 dependence of the shapes of these distributions on simulation. The half of the simulation
 2163 sample for which the templates are fitted too, are taken directly from simulation, extending
 2164 this procedure to also be a validation of the formula method to accurately estimate

the n_b^{reco} distribution. Additionally as this test is performed in simulation, the relevant corrections of the b-tagging rates between data and simulation are *not* applied.

Within Figure 6.2, the results of this fitting procedure is shown for each CSV working point. Results are presented for the $n_{jet} \geq 5$ category, using the $\mu +$ jets control sample selection in the inclusive $H_T > 375$ GeV analysis bin. The grey bands represent the statistical uncertainty on the template shapes. Additional fits are shown for other n_{jet} category within Appendix D.1.

Furthermore the extrapolated fit predictions within the high n_b^{reco} signal region, are summarised for all H_T bins and working points in Table 6.1.

H_T	275-325	325-375	>375
Loose working point			
Simulation $n_b = 3$	344.0 ± 6.8	158.8 ± 4.5	324.9 ± 6.5
Template $n_b = 3$	347.5 ± 11.6	162.6 ± 4.7	322.9 ± 6.9
Simulation $n_b = 4$	29.8 ± 1.9	11.1 ± 1.1	40.2 ± 2.4
Template $n_b = 4$	32.6 ± 2.0	13.0 ± 1.0	37.0 ± 1.8
Medium working point			
Simulation $n_b = 3$	58.2 ± 2.87	33.3 ± 2.1	72.1 ± 3.1
Template $n_b = 3$	60.1 ± 1.9	32.1 ± 1.5	70.8 ± 2.3
Simulation $n_b = 4$	1.0 ± 0.4	0.3 ± 0.2	1.5 ± 0.4
Template $n_b = 4$	1.2 ± 0.1	0.4 ± 0.1	2.2 ± 0.2
Tight working point			
Simulation $n_b = 3$	58.2 ± 2.87	33.3 ± 2.1	72.1 ± 3.1
Template $n_b = 3$	60.1 ± 1.9	32.1 ± 1.5	70.8 ± 2.3
Simulation $n_b = 4$	1.0 ± 0.4	0.3 ± 0.2	1.5 ± 0.4
Template $n_b = 4$	1.2 ± 0.1	0.4 ± 0.1	2.2 ± 0.2

Table 6.1.: Summary of the fit predictions in the n_b^{reco} signal region for $n_{jet} = 3, = 4, \geq 5$. The fit region is $n_b^{reco} = 0, 1, 2$ and simulation yields are normalised to an integrated luminosity of 10 fb^{-1} . The uncertainties quoted on the template yields are purely statistical.

The pull distributions for all the fits performed are compatible with a mean of zero and standard distributions, see Appendix D.2.

The good overall agreement summarised in the table validates both the formula method used to generate the templates as well as the fitting method itself. The application of this method to the same selection in data is used to demonstrate necessary control over the efficiency and mis-tagging rates.

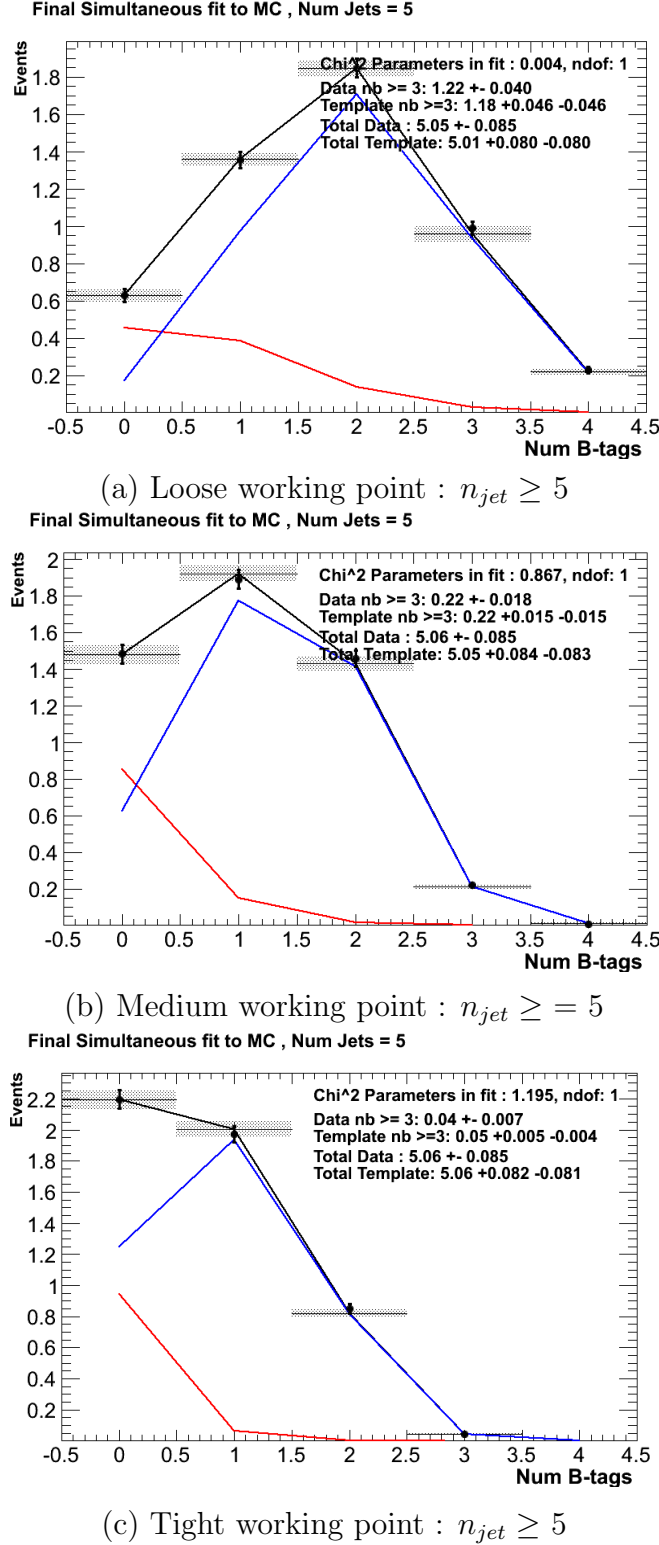


Figure 6.2.: The results of fitting the $Z = 0$ and $Z = 2$ templates to the $n_b^{reco} = 0, 1, 2$ bins taken directly from simulation in the region $H_T > 375$ GeV, for the $n_{jet} \geq 5$ category. The red template represents $Z = 0$, while the blue template represents $Z = 2$. Grey bands represent the statistical uncertainty of the fit. The χ^2 parameter displayed represents the goodness of fit to the low n_b^{reco} (0-2) control region.

 2180 6.2.2. Results in a data control sample

2181 The method above is now applied to the 2012 8 TeV dataset in the $\mu +$ jets control
 2182 sample, to establish the validity of this method in data. The relevant data to simulation
 2183 scale factors are applied to get corrected values of the efficiency and mis-tagging rates
 2184 measured in data [64] [84].

2185 Figure 6.3 show the the results of the templates derived from simulation to each of the
 2186 three defined H_T bins, in the $n_{jet} \geq 5$ category for the medium working point CSV
 2187 tagger (the same working point used within the α_T analysis). Grey bands represent the
 2188 statistical uncertainty of the fit combined in quadrature with the systematic uncertainties
 2189 of varying the data to simulation scale factors up and down by their measured systematic
 2190 uncertainties. Additional fit results for the other working points are found in Appendix
 2191 D.3

2192 The numerical results and extrapolation to the $n_b^{reco} = 3, 4$ bins for all H_T and working
 2193 points is shown in Table 6.2.

H_T	275-325	325-375	>375
Loose working point			
Data $n_b = 3$	717	338	618
Template $n_b = 3$	782.6 ± 16.8	340.6 ± 10.2	601.9 ± 14.2
Data $n_b = 4$	68	39	68
Template $n_b = 4$	75.0 ± 2.7	27.6 ± 1.3	71.6 ± 2.6
Medium working point			
Data $n_b = 3$	124	73	137
Template $n_b = 3$	124.3 ± 2.3	62.0 ± 1.7	121.9 ± 2.5
Data $n_b = 4$	1	1	3
Template $n_b = 4$	2.6 ± 0.1	1.3 ± 0.1	4.0 ± 0.1
Tight working point			
Data $n_b = 3$	21	13	23
Template $n_b = 3$	26.7 ± 0.5	11.7 ± 0.3	21.9 ± 0.5
Data $n_b = 4$	0	0	0
Template $n_b = 4$	0.23 ± 0.07	0.09 ± 0.04	0.29 ± 0.09

Table 6.2.: Summary of the fit predictions in the n_b^{reco} signal region of the $\mu +$ jets control sample, for $n_{jet} = 3, = 4, \geq 5$. The fit region is $n_b^{reco} = 0, 1, 2$ using 11.5 fb^{-1} of data at $\sqrt{s} = 8\text{TeV}$. The uncertainties quoted on the template yields are purely statistical.

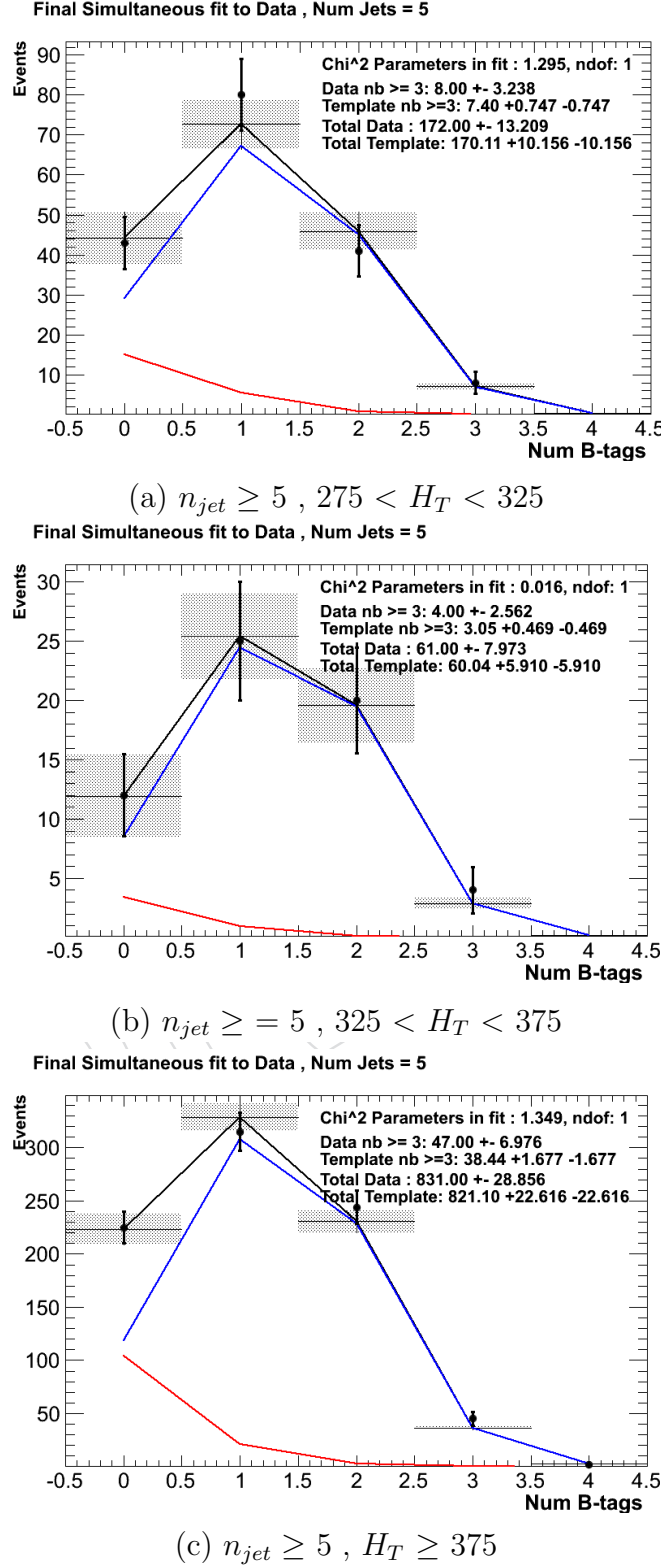


Figure 6.3.: The results of fitting the $Z = 0$ and $Z = 2$ templates to the $n_b^{reco} = 0, 1, 2$ bins taken directly from data, for the $n_{jet} \geq 5$ category and medium CSV working point. The red template represents $Z = 0$, while the blue template represents $Z = 2$. The χ^2 parameter displayed represents the goodness of fit to the low n_b^{reco} (0-2) control region.

2194 The agreement for all working points demonstrates a good control of the b-tagging
2195 efficiency and mis-tagging rates and gives confidence in the method outlined.

2196 6.2.3. Application to the α_T hadronic search region

2197 As an accompaniment to the background estimation methods outlined by the α_T search.
2198 The b-tag template method offers a complimentary way of estimated the background
2199 within the hadronic signal region of the search.

2200 6.3. Summary

2201 A **SUSY** signature such as one from gluino-induced third-generation squark production,
2202 would result in a final state with an underlying b-quark content greater than two. In
2203 order to be able to discriminate such signatures from the **SM** background, templates are
2204 generated based on a parameterisation of the number of the **SM** processes, where the
2205 underlying b-quarks per event is typically zero or two. These templates are then fit to
2206 data in a low n_b^{reco} (0-2) control region in order to extrapolate a prediction in a high
2207 n_b^{reco} (3-4) signal region.

2208 The method was demonstrated both in simulation and also in data, using the **SM** enriched
2209 $\mu + \text{jets}$ selection from the α_T search, to prove conceptually and experimentally that the
2210 method works and there is adequate control over the efficiency and mis-tagging rates in
2211 data for all working points of the **CSV** tagger. Additionally this method was also applied
2212 to the α_T analysis signal region where good agreement is observed between data and the
2213 background estimation method of the α_T analysis.

Chapter 7.

²²¹⁴ Conclusions

²²¹⁵ A search for supersymmetry is presented based on a data sample of pp collisions collected
²²¹⁶ at $\sqrt{s} = 8$ TeV, corresponding to an integrated luminosity of 11.7 ± 0.5 fb⁻¹. Final
²²¹⁷ states with two or more jets and significant \cancel{E}_T , a typical final state topology of R-parity
²²¹⁸ conserving SUSY models have been analysed. The sum of standard model backgrounds
²²¹⁹ per bin are estimated from a simultaneous binned likelihood fit to hadronic, $\mu +$ jets,
²²²⁰ $\mu\mu +$ jets, and $\gamma +$ jets samples. Systematic errors due to theory, detector effects and
²²²¹ analysis choices are quantified through the use of data driven closure tests and accounted
²²²² for in the final interpretation.

²²²³ No excess of events is observed over the expected SM background. The analysis is
²²²⁴ further interpreted in a set of SMS models, with a special emphasis on third generation
²²²⁵ squarks and compressed spectra scenarios. In the considered models with gluino pair
²²²⁶ production and for small LSP masses, exclusion limits of the gluino mass are in the range
²²²⁷ 950-1125 GeV. For SMS with squark pair production, first or second generation squarks
²²²⁸ are excluded up to around 775 GeV and bottom squarks are excluded up to 600 GeV,
²²²⁹ again for small LSP masses.

²²³⁰ A complementary approach using a templated method to estimate the b-tag jet distribu-
²²³¹ tion of SM processes, is used to search for gluino induced third generation squark SUSY
²²³² production. The α_T analysis is used to demonstrate conceptually and experimentally
²²³³ this technique in the $\mu +$ jets control sample. This method is further applied to the
²²³⁴ α_T hadronic search region where good agreement is observed between the data and the
²²³⁵ background estimation procedure of the α_T analysis.

²²³⁶ The performance of the Level-1 trigger for jets and energy sum quantities is also presented.
²²³⁷ These studies quantify any change in level-1 performance after the introduction of a 5

₂₂₃₈ GeV jet seed threshold into the jet algorithm configuration. No significant change in
₂₂₃₉ single jet trigger efficiencies is observed and good performance is observed for a range of
₂₂₄₀ level-1 quantities.

₂₂₄₁

Appendix A.

²²⁴² Miscellaneous

²²⁴³ A.1. Noise Filters

²²⁴⁴ For Calo jets the following criteria were applied:

Loose CaloJet Id	
Variable	Definition
$f_{HPD} < 0.98$	Fraction of jet energy contributed from “hottest” HPD , which rejects HCAL noise.
$f_{EM} > 0.01$	Noise from the HCAL is further suppressed by requiring a minimal electromagnetic component to the jet f_{EM} .
$N_{hits}^{90} \geq 2$	Jets that have $> 90\%$ of its energy from a single channel are rejected, to serve as a safety net that catches jets arising from undiagnosed noisy channels.

Table A.1.: Criteria for a reconstructed jet to pass the loose calorimeter jet id.

²²⁴⁵ For PF jets the following criteria were applied:

Loose PF jet Id	
Variable	Definition
$\text{nfhJet} < 0.99$	Fraction of jet composed of neutral hadrons. HCAL noise tends to populate high values of neutral hadron fraction.
$\text{nemfJet} < 0.99$	Fraction of jet composed of neutral electromagnetic energy. ECAL noise tends to populate high values of neutral EM fraction.
$\text{nmultiJet} > 1$	Number of constituents that jet is composed from.
$\text{chfJet} > 0$	Fraction of jet composed of charged hadrons.
$\text{cmultiJet} > 0$	Number of charged particles that compose jet.
$\text{cemfJet} < 0.99$	Fraction of jet composed of charged electromagnetic energy.

Table A.2.: Criteria for a reconstructed jet to pass the loose PF jet id.

²²⁴⁶ The following noise filters are applied, to remove events with spurious, non-physical jets
²²⁴⁷ or missing transverse energy.

Noise Filters	
Variable	Definition
CSC tight beam halo filter	As proton beams circle the LHC , proton interactions with the residual gas particles or the beam collimators can occur, producing showers of secondary particles which can interact with the CMS detector.
HBHE noise filter with isolated noise rejection	Anomalous noise in the HCAL not due to electronics noise, but rather due to instrumentation issues associated with the HPD 's and Readout Boxes (RBXs).
HCAL laser filter	The HCAL uses laser pulses for monitoring the detector response. Some laser pulses have accidentally been fired in the physics orbit, and ended up polluting events recorded for physics analysis.
ECAL dead cell trigger primitive (TP) filter	EB and EE have single noisy crystals which are masked in reconstruction. Use the Trigger Primitive (TP) information to assess how much energy was lost in masked cells.
Bad EE Supercrystal filter	Two supercrystals in EE are found to occasionally produce high amplitude anomalous pulses in several channels at once, causing a large \cancel{E}_T spike.
ECAL Laser correction filter	A laser calibration multiplicative factor is applied to correct for transparency loss in each crystal during irradiation. A small number of crystals receive unphysically large values of this correction and become very energetic, resulting in \cancel{E}_T .

Table A.3.: Noise filters that are applied to remove spurious and non-physical \cancel{E}_T signatures within the **CMS** detector.

2248 A.2. Primary Vertices

2249 The pileup per event is defined by the number of 'good' reconstructed primary vertices
2250 in the event, with each vertex satisfying the following requirements

Good primary vertex requirement	
Variable	Definition
$N_{dof} > 4$	The number of degree of freedom, from the vertex fit to compute the best estimate of the vertex parameters.
$ \Delta z_{vtx} < 24\text{cm}$	The distance, $ \Delta z_{vtx} $, to the position of the closest HLT primary vertex.
$\rho < 2\text{cm}$	The perpendicular distance of track position to the beam spot.

Table A.4.: Criteria for a vertex in an event to be classified as a 'good' reconstructed primary vertex.

Appendix B.

2251 L1 Jets

2252 B.1. Jet matching efficiencies

2253 The single jet turn-on curves are derived from events independent of whether the leading
2254 jet in an event is matched to a Level 1 jet using ΔR matching detailed in Section (3.4.3)
2255 or not. These turn-ons are produced from events which are not triggered on jet quantities
2256 and therefore it is not guaranteed that the lead jet of an event will be seeded by a Level
2257 1 jet. Figure B.1 shows the particular matching efficiency of a lead jet to a L1 jet.

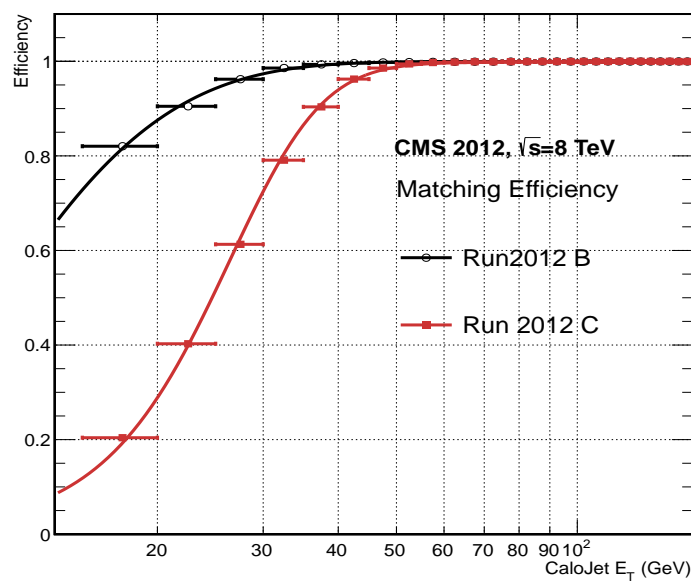


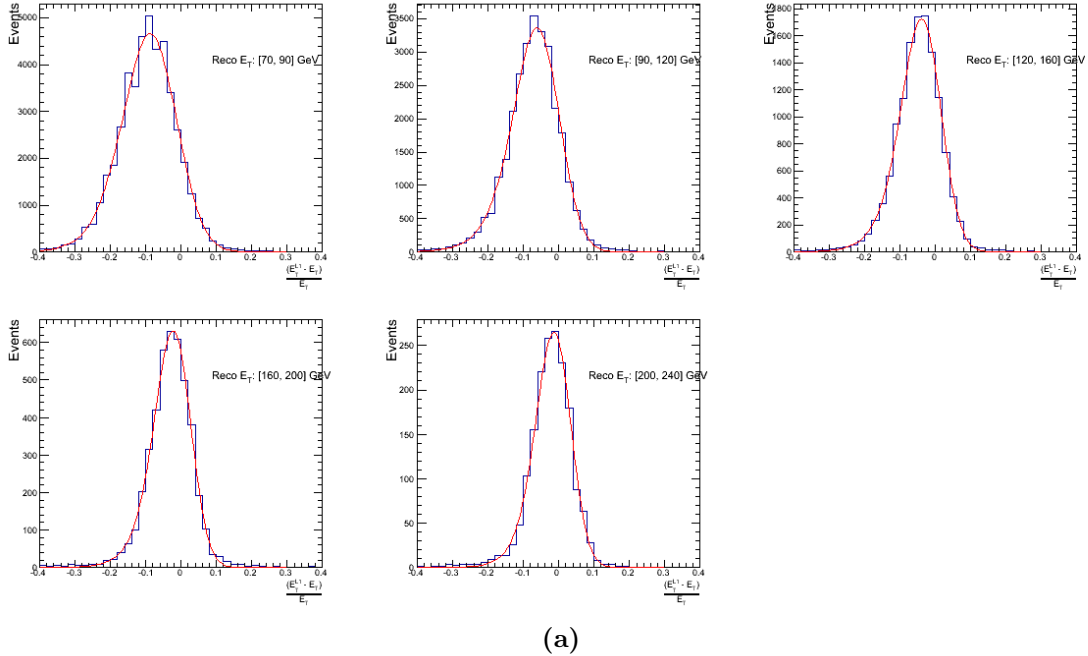
Figure B.1.: Leading jet matching efficiency as a function of the offline CaloJet E_T , measured in an isolated muon triggered dataset in the 2012B and 2012C run periods.

Run Period	μ	σ
2012B	6.62 ± 0.01	0.79 ± 0.03
2012C	19.51 ± 0.03	7.14 ± 0.02

Table B.1.: Results of a cumulative EMG function fit to the turn-on curves for the matching efficiency of the leading jet in an event to a Level-1 jet in run 2012C and 2012B data, measured in an isolated muon triggered sample. The turn-on point, μ , and resolution, σ , are measured with respect to offline Calo Jet E_T .

- 2258 It can be seen that the turn on is sharper during the 2012B run period. The seed
 2259 threshold requirement of a 5 GeV jet seed in run 2012C results in more events in which
 2260 even the lead offline jet does not have an associated L1 jet. For larger jet E_T thresholds,
 2261 typical of thresholds used in physics analyses, 100% efficiency is observed.
 2262 The matching efficiencies have a μ values of 6.62 GeV and 19.51 GeV for Run 2012B
 2263 and 2012C respectively and is shown in Table B.1.

2264 B.2. Leading Jet Energy Resolution



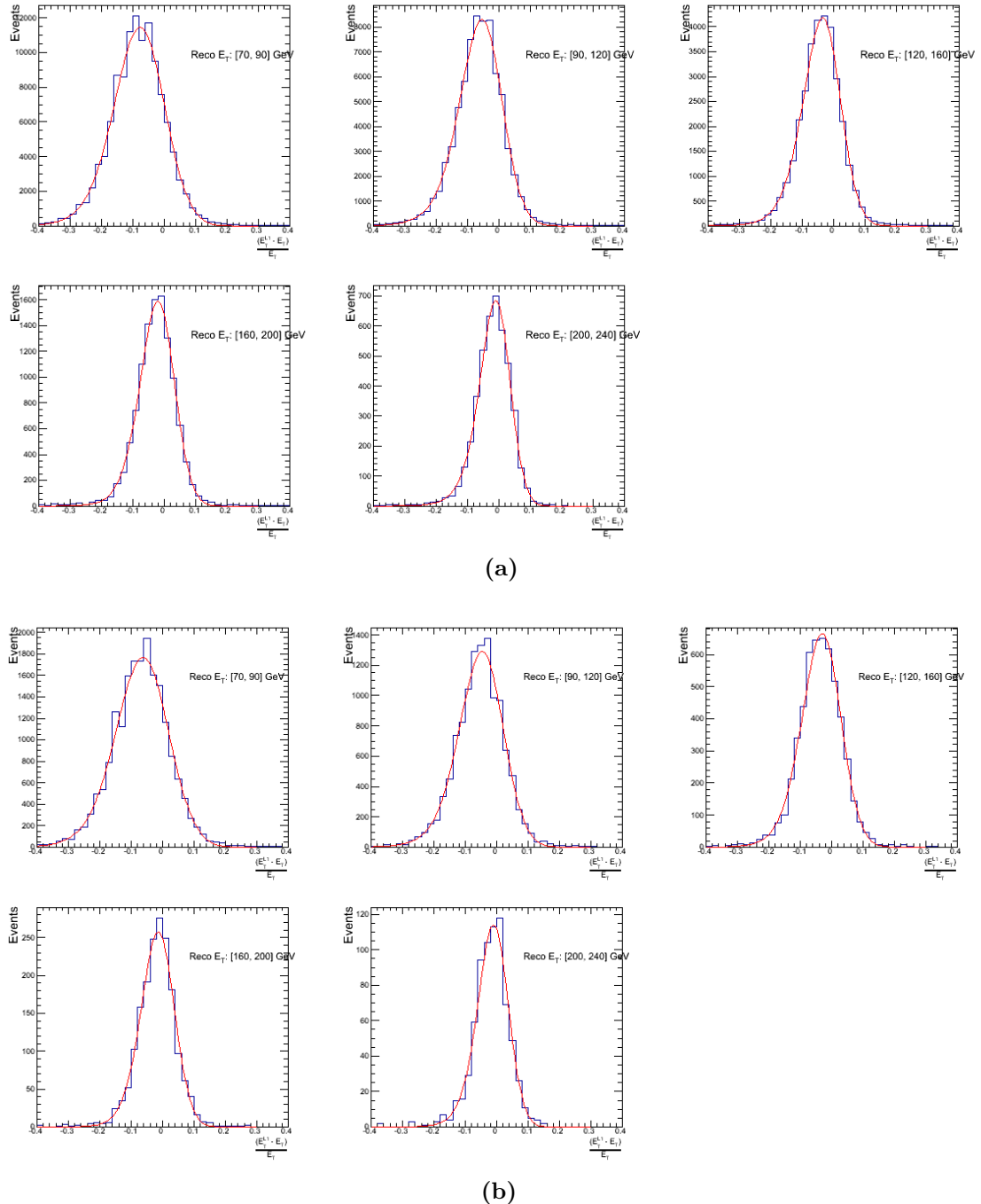
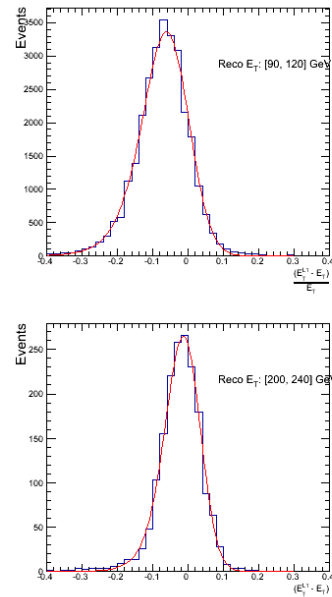
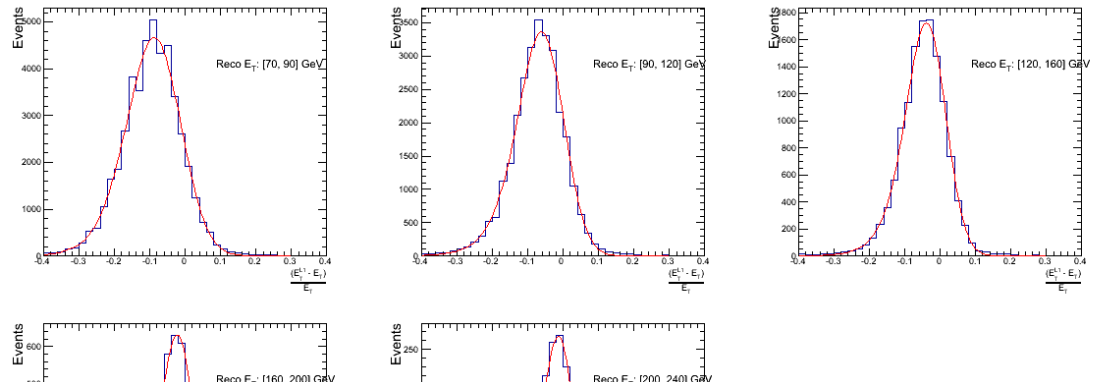
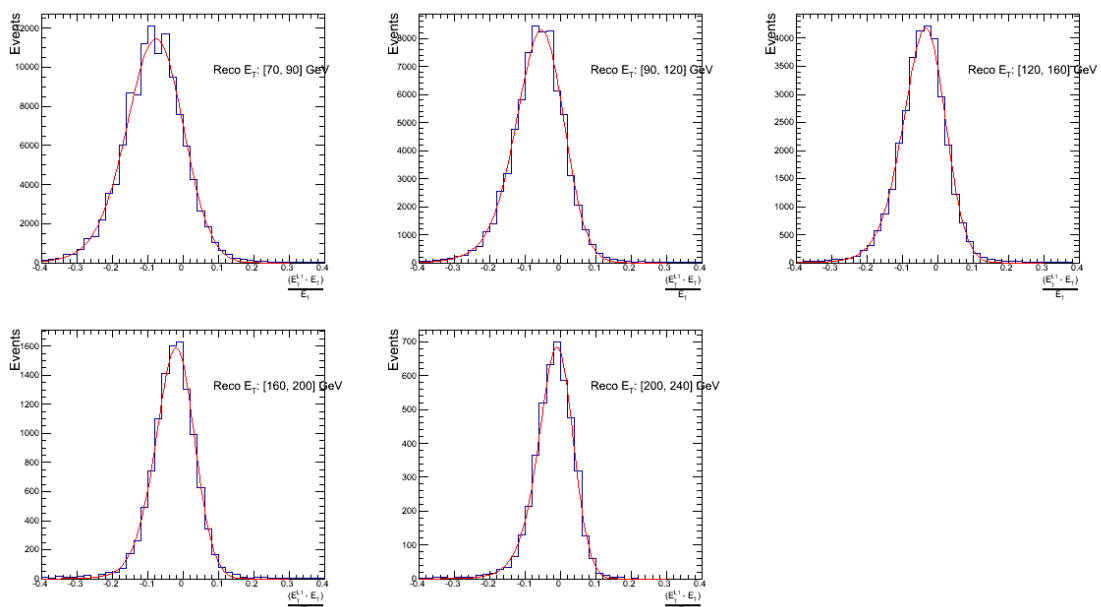


Figure B.2.: Resolution plots of the leading offline jet Calo E_T measured as a function of $\frac{(\text{L1 } E_T - \text{Offline } E_T)}{\text{Offline } E_T}$ for low (a), medium (b) and high (c) pile-up conditions.



(a)



(b)

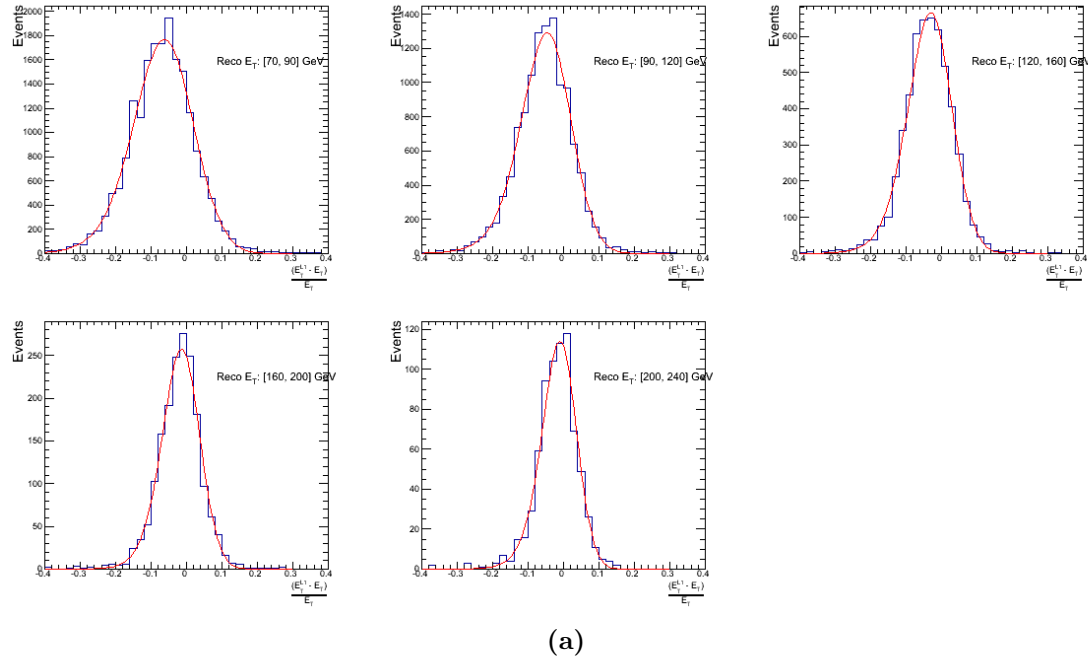


Figure B.3.: Resolution plots of the leading offline jet PF E_T measured as a function of $\frac{(L1 E_T - \text{Offline } E_T)}{\text{Offline } E_T}$ for low (a), medium (b) and high (c) pile-up conditions.

2265 B.3. Resolution for Energy Sum Quantities

2266 The following plots show the resolution parameters for the four energy sum quantities as
 2267 a function of the quantity (q) itself. In this case, The mean and RMS of the individual
 2268 $\frac{(L1 q - \text{Offline } q)}{\text{Offline } q}$ distributions, in bins of the quantity q is displayed.

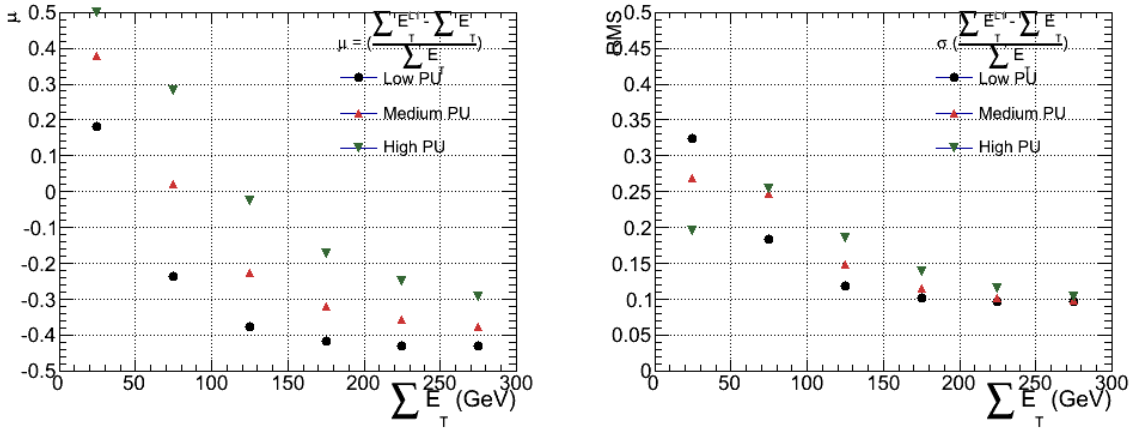


Figure B.4.: $\sum E_T$ resolution parameters in bins of Calo $\sum E_T$ measured for the defined low, medium and high pile up conditions. The plots show the mean μ (left), resolution σ (RMS) of the $\frac{\Delta q}{q}$ distributions.

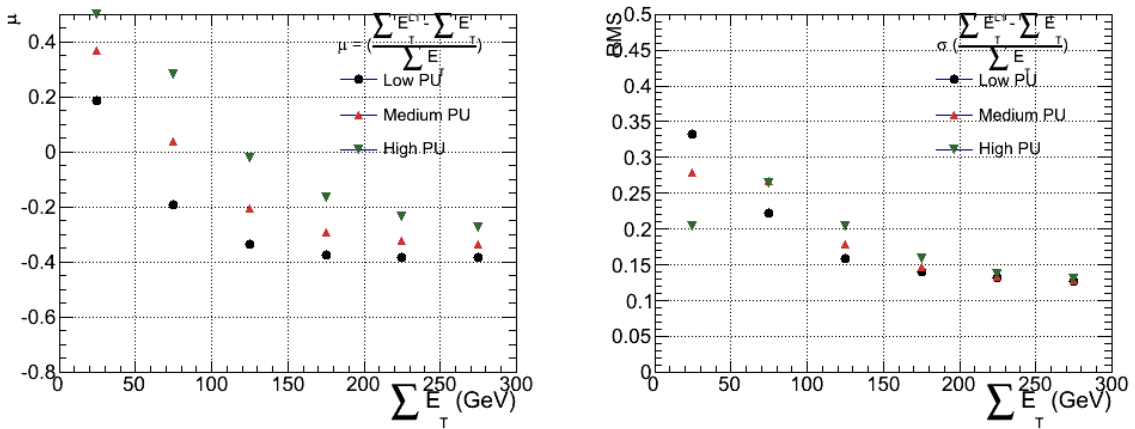


Figure B.5.: $\sum E_T$ resolution parameters in bins of PF $\sum E_T$ measured for the defined low, medium and high pile up conditions. The plots show the mean μ (left), resolution σ (RMS) of the $\frac{\Delta q}{q}$ distributions.

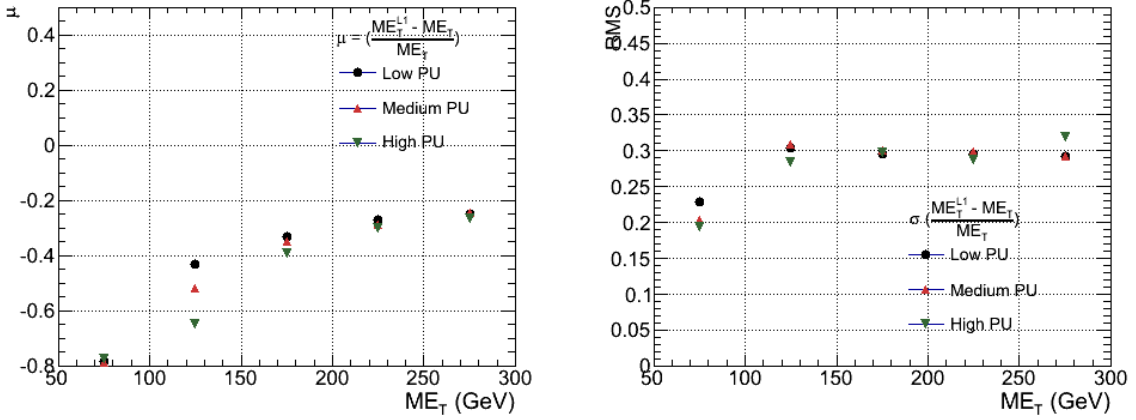


Figure B.6.: \mathcal{E}_T resolution parameters in bins of Calo \mathcal{E}_T measured for the defined low, medium and high pile up conditions. The plots show the mean μ (left), resolution σ (RMS) of the $\frac{\Delta q}{q}$ distributions.

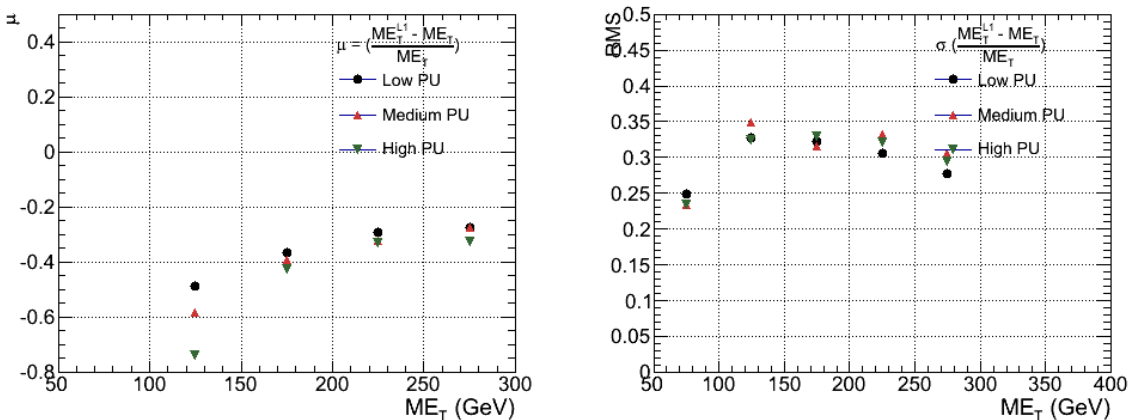


Figure B.7.: \mathcal{E}_T resolution parameters in bins of PF \mathcal{E}_T measured for the defined low, medium and high pile up conditions. The plots show the mean μ (left), resolution σ (RMS) of the $\frac{\Delta q}{q}$ distributions.

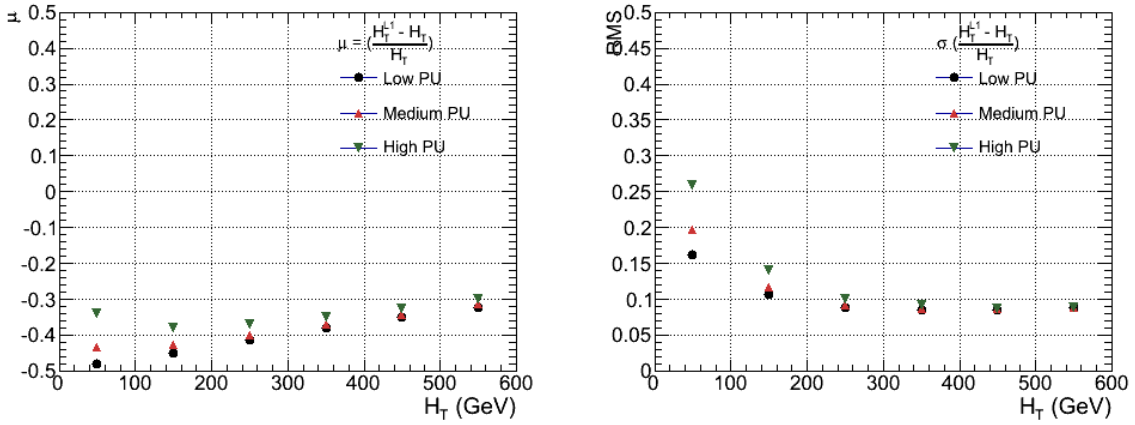


Figure B.8.: H_T resolution parameters in bins of Calo H_T measured for the defined low, medium and high pile up conditions. The plots show the mean μ (left), resolution σ (RMS) of the $\frac{\Delta q}{q}$ distributions.

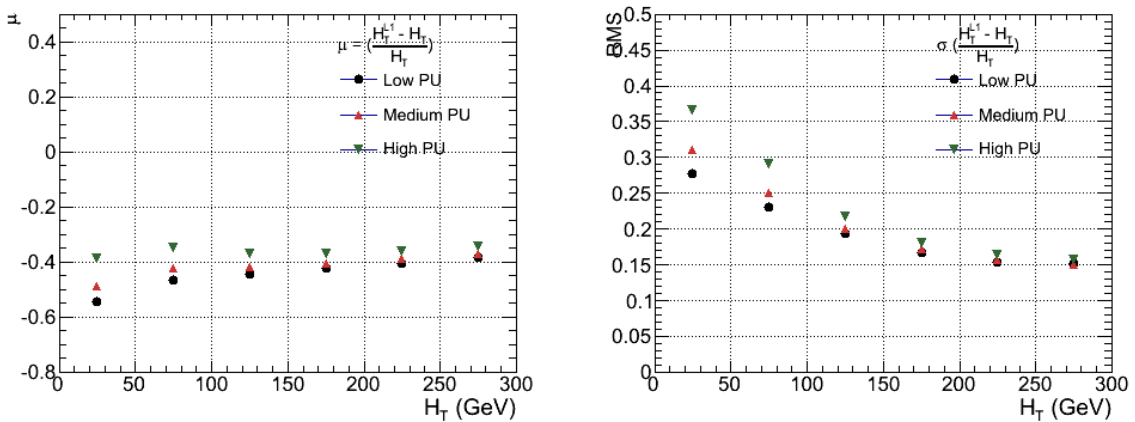


Figure B.9.: H_T resolution parameters in bins of PF H_T measured for the defined low, medium and high pile up conditions. The plots show the mean μ (left), resolution σ (RMS) of the $\frac{\Delta q}{q}$ distributions.

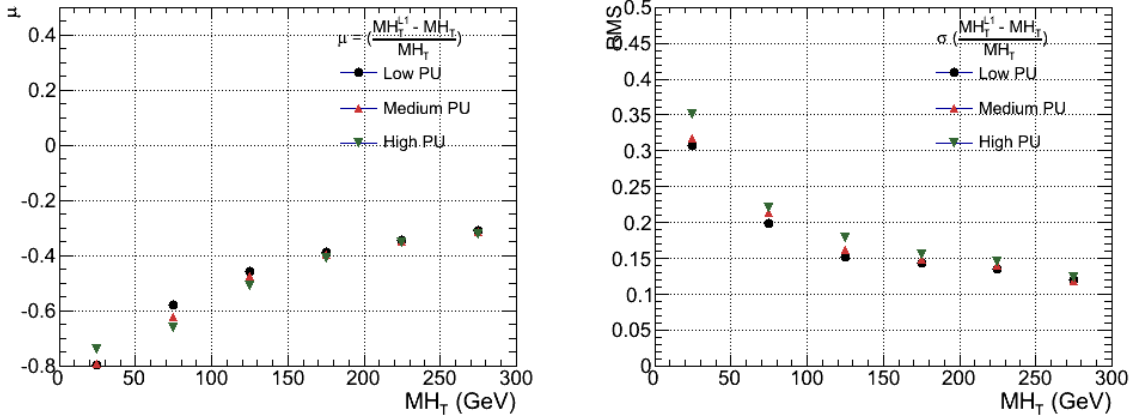


Figure B.10.: H_T resolution parameters in bins of H_T measured for the defined low, medium and high pile up conditions. The plots show the mean μ (left), resolution σ (RMS) of the $\frac{\Delta q}{q}$ distributions.

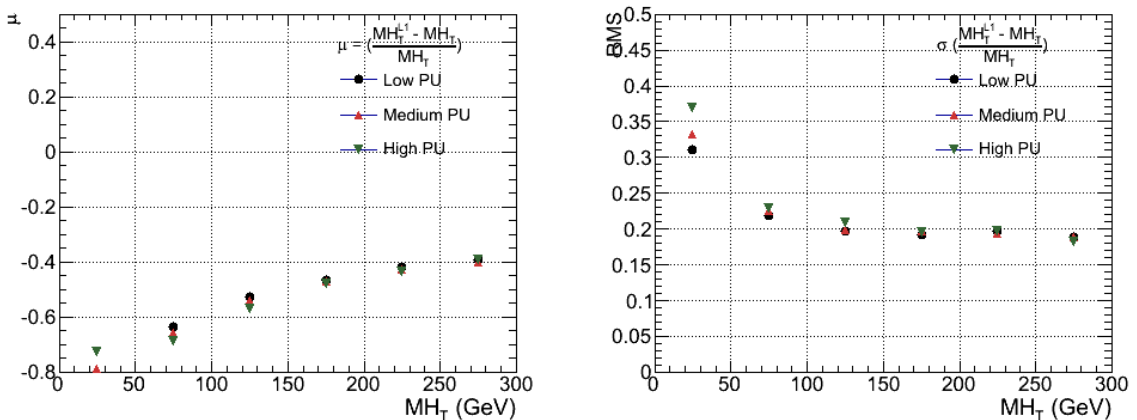


Figure B.11.: H_T resolution parameters in bins of PF H_T measured for the defined low, medium and high pile up conditions. The plots show the mean μ (left), resolution σ (RMS) of the $\frac{\Delta q}{q}$ distributions.

Appendix C.

2269 **Additional material on background
2270 estimation methods**

2271 **C.1. Determination of k_{QCD}**

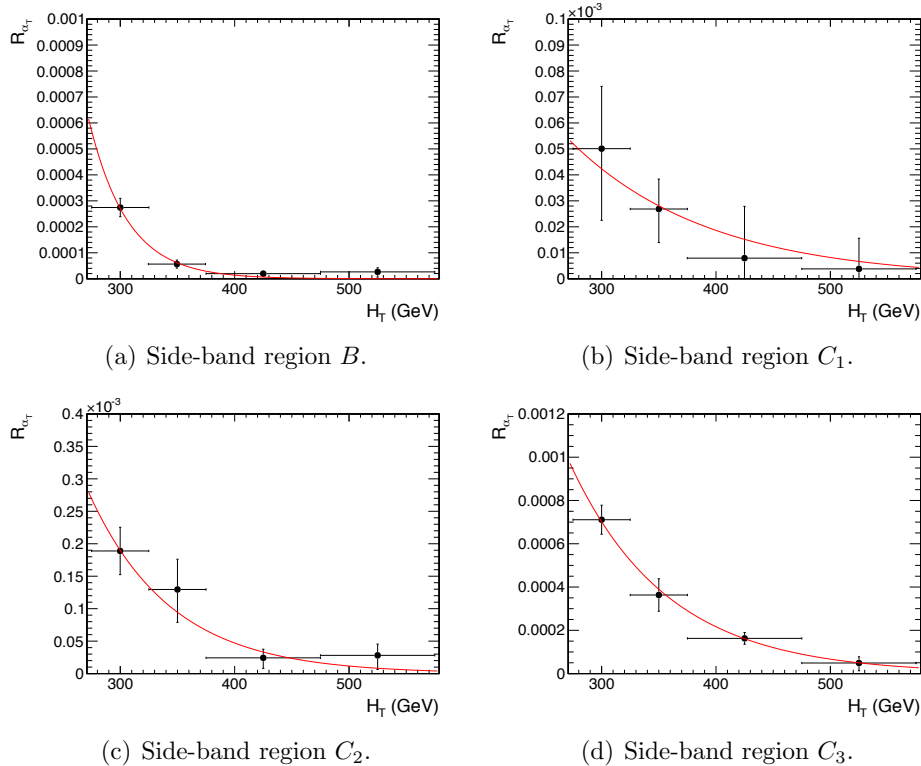


Figure C.1.: $R_{\alpha_T}(H_T)$ and exponential fits for each of the data sideband regions. Fit is conducted between the H_T region $275 < H_T < 575$.

2273 **C.2. Effect of varying background cross sections on**
2274 **closure tests**

2275 Closure tests with cross section variations of +20% and -20% applied to $W + \text{jets}$ and $t\bar{t}$
2276 processes respectively.

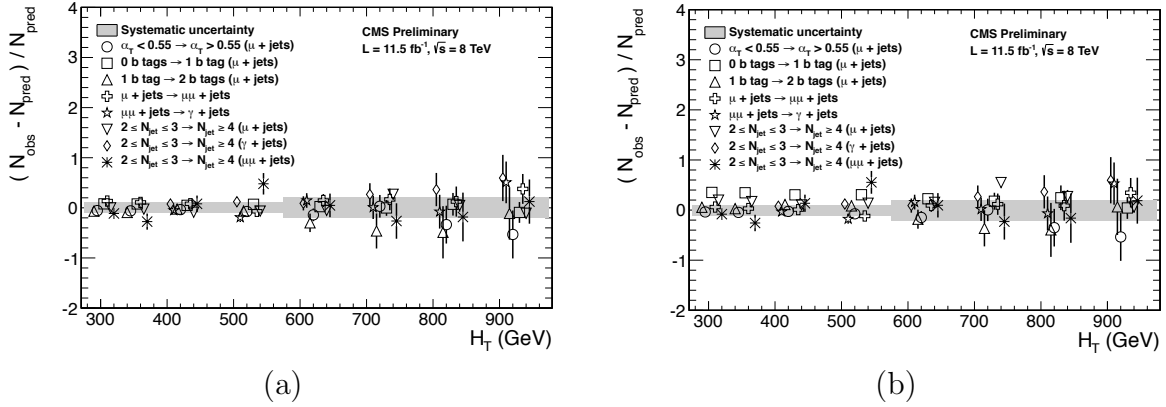


Figure C.2.: Sets of closure tests (open symbols) overlaid on top of the systematic uncertainty used for each of the five H_T regions (shaded bands) and for the two different jet multiplicity bins: (a) $2 \leq n_{jet} \leq 3$ and (b) $n_{jet} \geq 4$.

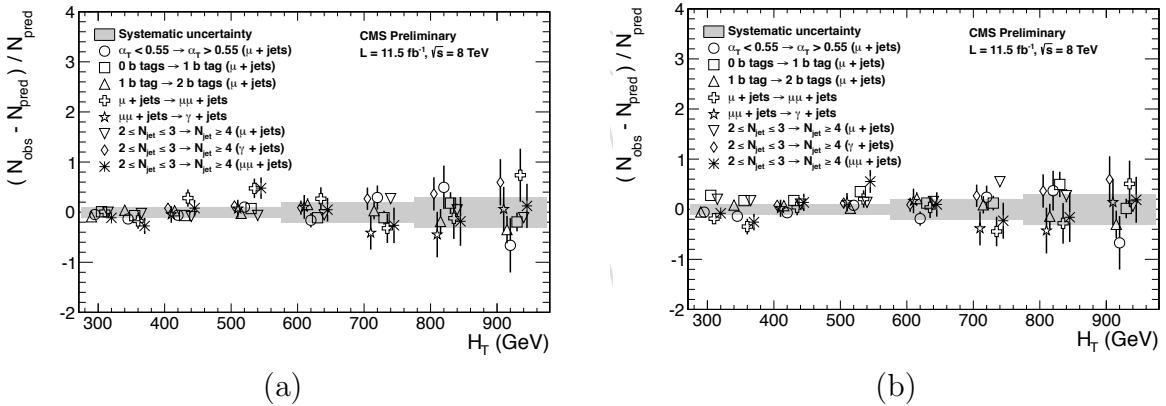


Figure C.3.: Sets of closure tests (open symbols) overlaid on top of the systematic uncertainty used for each of the five H_T regions (shaded bands) and for the two different jet multiplicity bins: (a) $2 \leq n_{jet} \leq 3$ and (b) $n_{jet} \geq 4$.

	H_T (GeV)
--	-------------

Table C.1.

Appendix D.

²²⁷⁷ Additional Material For B-tag ²²⁷⁸ Template Method

²²⁷⁹ D.1. Templates Fits in Simulation

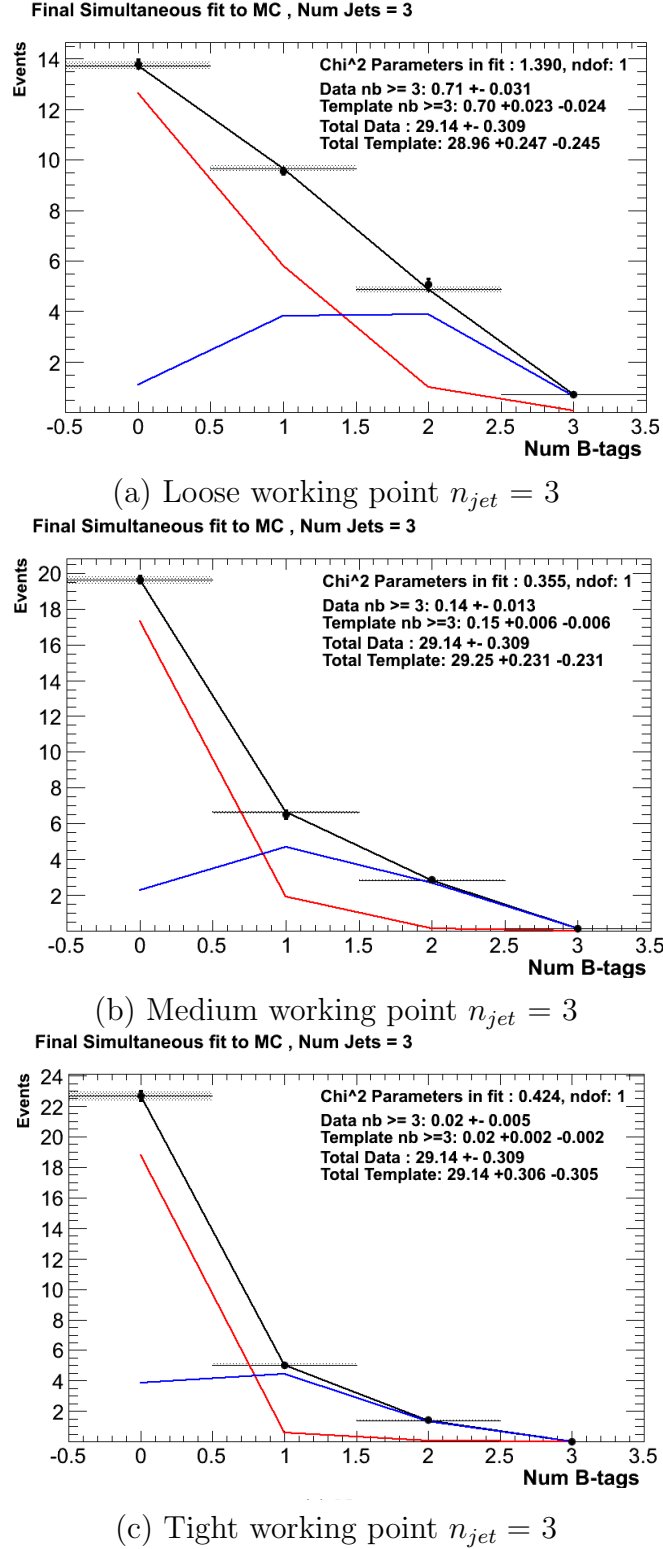


Figure D.1.: The results of fitting the $Z = 0$ and $Z = 2$ templates to the $n_b^{reco} = 0, 1, 2$ bins taken directly from simulation in the region $H_T > 375$ GeV, for the $n_{jet} = 3$ category. The red template represents $Z = 0$, while the blue template represents $Z = 2$. Grey bands represent the statistical uncertainty of the fit. The χ^2 parameter displayed represents the goodness of fit to the low n_b^{reco} (0-2) control region.

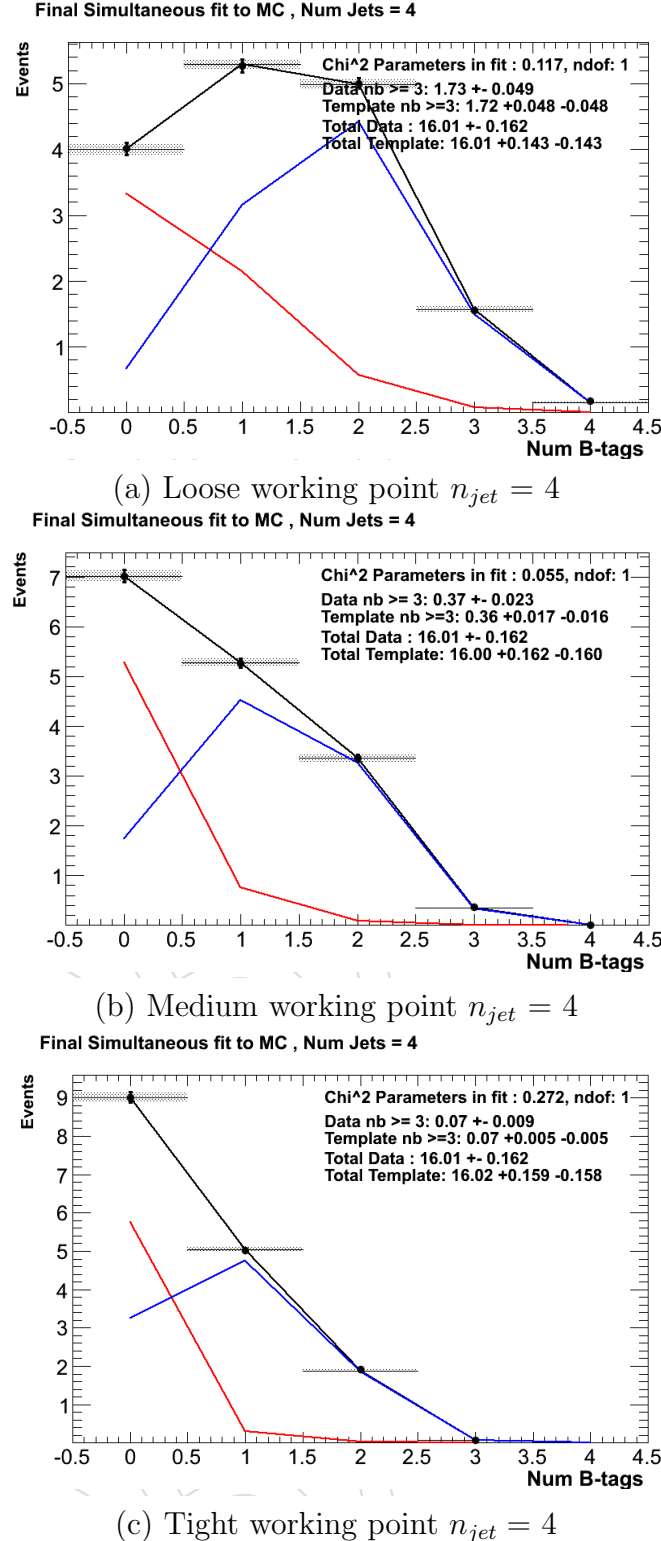


Figure D.2.: The results of fitting the $Z = 0$ and $Z = 2$ templates to the $n_b^{reco} = 0, 1, 2$ bins taken directly from simulation in the region $H_T > 375$ GeV, for the $n_{jet} = 4$ category. The red template represents $Z = 0$, while the blue template represents $Z = 2$. Grey bands represent the statistical uncertainty of the fit. The χ^2 parameter displayed represents the goodness of fit to the low n_b^{reco} (0-2) control region.

2280 **D.2. Pull Distributions for Template Fits**

2281 **D.3. Templates Fits in Data**

2282 Template fits for the loose **CSV** working point :

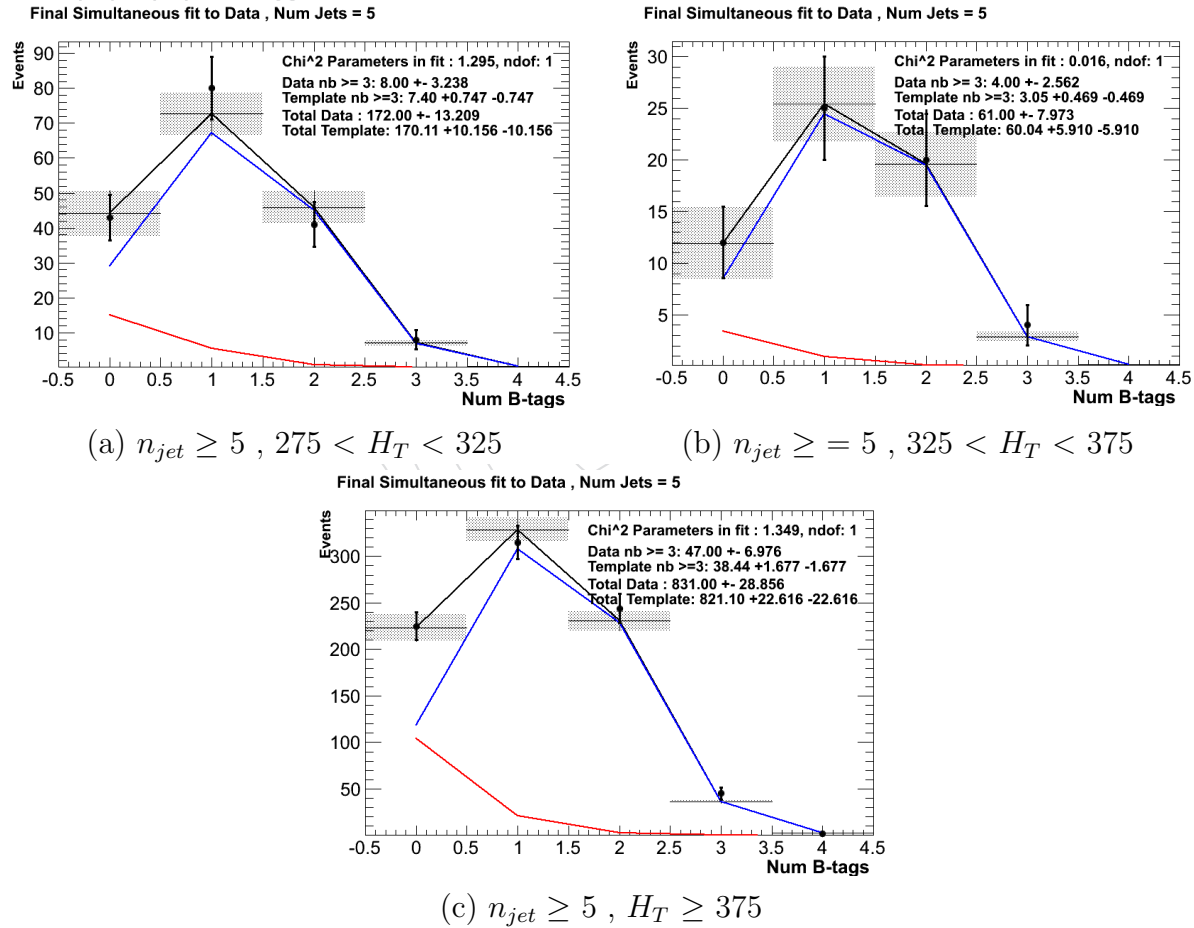


Figure D.3.: The results of fitting the $Z = 0$ and $Z = 2$ templates to the $n_b^{reco} = 0, 1, 2$ bins taken from data, for the $n_{jet} \geq 5$ category and loose **CSV** working point. The red template represents $Z = 0$, while the blue template represents $Z = 2$. The χ^2 parameter displayed represents the goodness of fit to the low n_b^{reco} (0-2) control region.

2283 Template fits for the tight **CSV** working point :

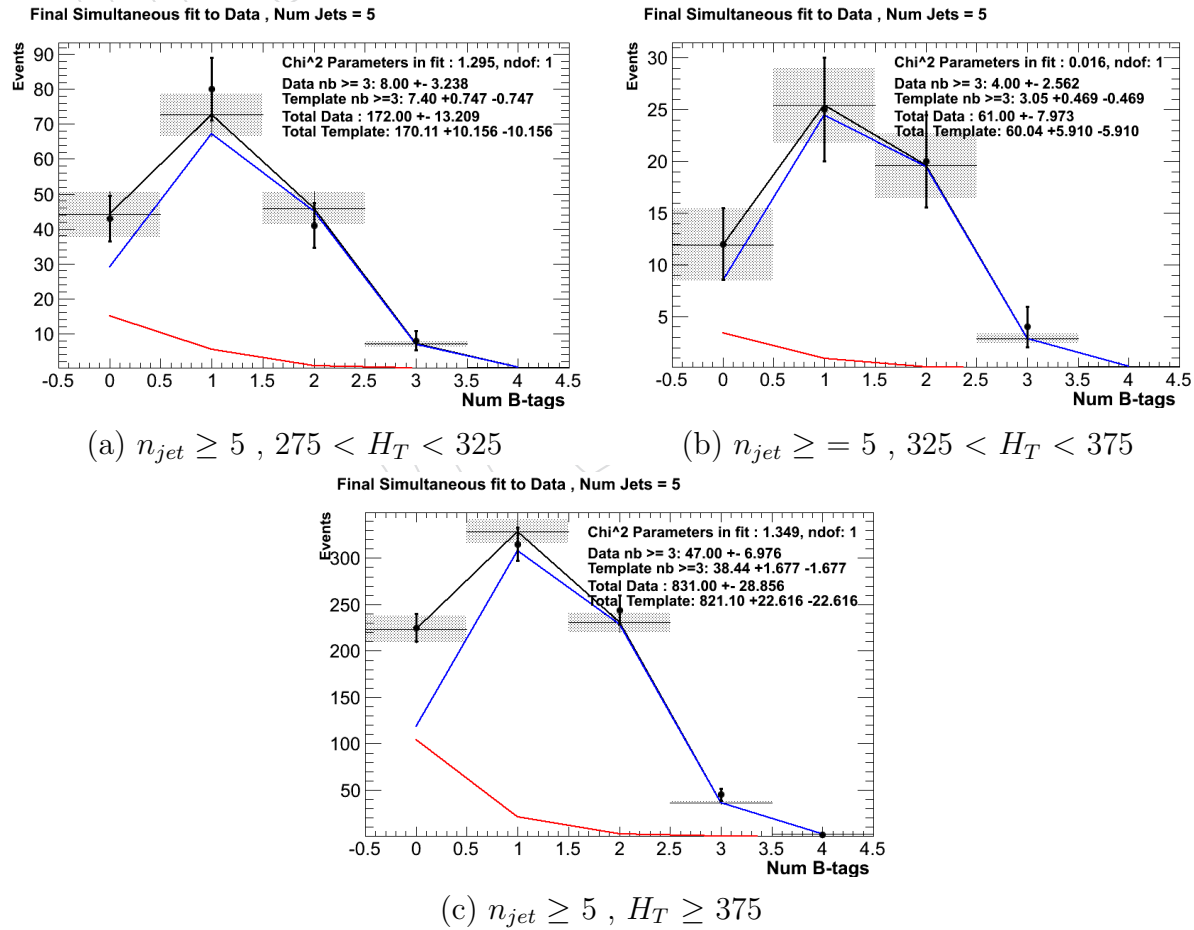


Figure D.4.: The results of fitting the $Z = 0$ and $Z = 2$ templates to the $n_b^{reco} = 0, 1, 2$ bins taken from data, for the $n_{jet} \geq 5$ category and tight CSV working point. The red template represents $Z = 0$, while the blue template represents $Z = 2$. The χ^2 parameter displayed represents the goodness of fit to the low n_b^{reco} (0-2) control region.

²²⁸⁵ Bibliography

- ²²⁸⁶ [1] J. Beringer *et al.*, “Review of Particle Physics (RPP),” *Phys.Rev.*, vol. D86, p. 010001, 2012.
- ²²⁸⁸ [2] G. H. et al., “Nine-year wilkinson microwave anisotropy probe (wmap) observations: ²²⁸⁹ Cosmological parameter results,” *The Astrophysical Journal Supplement Series*, ²²⁹⁰ vol. 208, no. 2, p. 19, 2013.
- ²²⁹¹ [3] G. Aad *et al.*, “Observation of a new particle in the search for the Standard Model ²²⁹² Higgs boson with the ATLAS detector at the LHC,” *Phys.Lett.*, vol. B716, pp. 1–29, ²²⁹³ 2012.
- ²²⁹⁴ [4] S. Chatrchyan *et al.*, “Observation of a new boson at a mass of 125 GeV with the ²²⁹⁵ CMS experiment at the LHC,” *Phys.Lett.*, vol. B716, pp. 30–61, 2012.
- ²²⁹⁶ [5] S. Chatrchyan *et al.*, “Search for supersymmetry in hadronic final states with missing ²²⁹⁷ transverse energy using the variables AlphaT and b-quark multiplicity in pp collisions ²²⁹⁸ at 8 TeV,” *Eur.Phys.J.*, vol. C73, p. 2568, 2013.
- ²²⁹⁹ [6] S. Weinberg, “A model of leptons,” *Phys. Rev. Lett.*, vol. 19, pp. 1264–1266, Nov ²³⁰⁰ 1967.
- ²³⁰¹ [7] S. Glashow, “Partial Symmetries of Weak Interactions,” *Nucl.Phys.*, vol. 22, pp. 579–²³⁰² 588, 1961.
- ²³⁰³ [8] A. Salam, “Weak and Electromagnetic Interactions,” *Conf.Proc.*, vol. C680519, ²³⁰⁴ pp. 367–377, 1968.
- ²³⁰⁵ [9] G. Hooft, “Renormalizable lagrangians for massive yang-mills fields,” *Nuclear Physics B*, ²³⁰⁶ vol. 35, no. 1, pp. 167 – 188, 1971.
- ²³⁰⁷ [10] F. Hasert *et al.*, “Observation of Neutrino Like Interactions Without Muon Or ²³⁰⁸ Electron in the Gargamelle Neutrino Experiment,” *Phys.Lett.*, vol. B46, pp. 138–140, ²³⁰⁹ 1973.

- [11] G. Arnison *et al.*, “Experimental Observation of Lepton Pairs of Invariant Mass Around 95-GeV/c**2 at the CERN SPS Collider,” *Phys.Lett.*, vol. B126, pp. 398–410, 1983.
- [12] M. Banner *et al.*, “Observation of Single Isolated Electrons of High Transverse Momentum in Events with Missing Transverse Energy at the CERN anti-p p Collider,” *Phys.Lett.*, vol. B122, pp. 476–485, 1983.
- [13] E. Noether, “Invariante variationsprobleme,” *Nachrichten von der Gesellschaft der Wissenschaften zu Gttingen, Mathematisch-Physikalische Klasse*, vol. 1918, pp. 235–257, 1918.
- [14] F. Halzen and A. D. Martin, “Quarks and leptons.” Wiley, 1985.
- [15] *Introduction to Elementary Particles*. Wiley-VCH, 2nd ed., Oct. 2008.
- [16] C. S. Wu, E. Ambler, R. W. Hayward, D. D. Hoppes, and R. P. Hudson, “Experimental Test of Parity Conservation in Beta Decay,” *Physical Review*, vol. 105, pp. 1413–1415, Feb. 1957.
- [17] P. Higgs, “Broken symmetries, massless particles and gauge fields,” *Physics Letters*, vol. 12, no. 2, pp. 132 – 133, 1964.
- [18] F. Englert and R. Brout, “Broken symmetry and the mass of gauge vector mesons,” *Phys. Rev. Lett.*, vol. 13, pp. 321–323, Aug 1964.
- [19] P. W. Higgs, “Broken symmetries and the masses of gauge bosons,” *Phys. Rev. Lett.*, vol. 13, pp. 508–509, Oct 1964.
- [20] G. S. Guralnik, C. R. Hagen, and T. W. B. Kibble, “Global conservation laws and massless particles,” *Phys. Rev. Lett.*, vol. 13, pp. 585–587, Nov 1964.
- [21] S. Weinberg, “A model of leptons,” *Phys. Rev. Lett.*, vol. 19, pp. 1264–1266, Nov 1967.
- [22] H. Yukawa, “On the interaction of elementary particles. i,” *Progress of Theoretical Physics Supplement*, vol. 1, pp. 1–10, 1955.
- [23] Y. e. a. Fukuda, “Evidence for oscillation of atmospheric neutrinos,” *Phys. Rev. Lett.*, vol. 81, pp. 1562–1567, Aug 1998.
- [24] R. Becker-Szendy, C. Bratton, D. Casper, S. Dye, W. Gajewski, *et al.*, “A Search for muon-neutrino oscillations with the IMB detector,” *Phys.Rev.Lett.*, vol. 69,

- 2340 pp. 1010–1013, 1992.
- 2341 [25] S. P. Martin, “A Supersymmetry primer,” 1997.
- 2342 [26] H. Nilles, *Supersymmetry, Supergravity and Particle Physics*. Physics reports, North-Holland Physics Publ., 1984.
- 2343
- 2344 [27] H. E. Haber and G. L. Kane, “The Search for Supersymmetry: Probing Physics Beyond the Standard Model,” *Phys.Rept.*, vol. 117, pp. 75–263, 1985.
- 2345
- 2346 [28] E. Witten, “Dynamical Breaking of Supersymmetry,” *Nucl.Phys.*, vol. B188, p. 513, 1981.
- 2347
- 2348 [29] J. Wess and B. Zumino, “Supergauge transformations in four dimensions,” *Nuclear Physics B*, vol. 70, no. 1, pp. 39 – 50, 1974.
- 2349
- 2350 [30] H. Muller-Kirsten and A. Wiedemann, *Introduction to Supersymmetry*. World Scientific lecture notes in physics, World Scientific, 2010.
- 2351
- 2352 [31] I. Aitchison, *Supersymmetry in Particle Physics: An Elementary Introduction*. Cambridge University Press, 2007.
- 2353
- 2354 [32] K. A. Intriligator and N. Seiberg, “Lectures on Supersymmetry Breaking,” *Class.Quant.Grav.*, vol. 24, pp. S741–S772, 2007.
- 2355
- 2356 [33] Y. Shadmi, “Supersymmetry breaking,” pp. 147–180, 2006.
- 2357
- 2358 [34] C. Burgess, P. G. Camara, S. de Alwis, S. Giddings, A. Maharana, *et al.*, “Warped Supersymmetry Breaking,” *JHEP*, vol. 0804, p. 053, 2008.
- 2359
- 2360 [35] H. Murayama, “Supersymmetry breaking made easy, viable, and generic,” 2007.
- 2361
- 2362 [36] H. Baer and X. Tata, *Weak Scale Supersymmetry: From Superfields to Scattering Events*. Cambridge University Press, 2006.
- 2363
- 2364 [37] S. P. Martin, “Implications of supersymmetric models with natural r-parity conservation,” 1996.
- 2365
- 2366 [38] G. L. Kane, C. F. Kolda, L. Roszkowski, and J. D. Wells, “Study of constrained minimal supersymmetry,” *Phys.Rev.*, vol. D49, pp. 6173–6210, 1994.
- 2367
- 2368 [39] C. Stlege, G. Bertone, D. Cerdeno, M. Fornasa, R. Ruiz de Austri, *et al.*, “Updated global fits of the cmSSM including the latest LHC SUSY and Higgs searches and XENON100 data,” *JCAP*, vol. 1203, p. 030, 2012.

- 2369 [40] M. Citron, J. Ellis, F. Luo, J. Marrouche, K. Olive, *et al.*, “The End of the CMSSM
2370 Coannihilation Strip is Nigh,” *Phys.Rev.*, vol. D87, p. 036012, 2013.
- 2371 [41] D. Ghosh, M. Guchait, S. Raychaudhuri, and D. Sengupta, “How Constrained is
2372 the cMSSM?,” *Phys.Rev.*, vol. D86, p. 055007, 2012.
- 2373 [42] D. Alves *et al.*, “Simplified Models for LHC New Physics Searches,” *J.Phys.*, vol. G39,
2374 p. 105005, 2012.
- 2375 [43] J. Alwall, P. Schuster, and N. Toro, “Simplified Models for a First Characterization
2376 of New Physics at the LHC,” *Phys.Rev.*, vol. D79, p. 075020, 2009.
- 2377 [44] S. Chatrchyan *et al.*, “Interpretation of Searches for Supersymmetry with simplified
2378 Models,” *Phys.Rev.*, vol. D88, p. 052017, 2013.
- 2379 [45] J. Hisano, K. Kurosawa, and Y. Nomura, “Natural effective supersymmetry,”
2380 *Nucl.Phys.*, vol. B584, pp. 3–45, 2000.
- 2381 [46] M. Papucci, J. T. Ruderman, and A. Weiler, “Natural SUSY Endures,” *JHEP*,
2382 vol. 1209, p. 035, 2012.
- 2383 [47] B. Allanach and B. Gripaios, “Hide and Seek With Natural Supersymmetry at the
2384 LHC,” *JHEP*, vol. 1205, p. 062, 2012.
- 2385 [48] K. Aamodt *et al.*, “The ALICE experiment at the CERN LHC,” *JINST*, vol. 3,
2386 p. S08002, 2008.
- 2387 [49] G. Aad *et al.*, “The ATLAS Experiment at the CERN Large Hadron Collider,”
2388 *JINST*, vol. 3, 2008.
- 2389 [50] R. Adolphi *et al.*, “The cms experiment at the cern lhc,” *JINST*, vol. 0803, p. S08004,
2390 2008.
- 2391 [51] A. A. Alves *et al.*, “The LHCb Detector at the LHC,” *JINST*, vol. 3, p. S08005,
2392 2008.
- 2393 [52] J.-L. Caron, “Lhc layout.. schema general du lhc..” Sep 1997.
- 2394 [53] C. Collaboration, “Cms luminosity - public results.”
2395 twiki.cern.ch/twiki/bin/view/CMSPublic/LumiPublicResults., 2011.
- 2396 [54] CERN, “Cms compact muon solenoid..” <http://public.web.cern.ch/public/Objects/LHC/CMSnc.jpg>
2397 Feb 2010.

- 2398 [55] *The CMS electromagnetic calorimeter project: Technical Design Report*. Technical
2399 Design Report CMS, Geneva: CERN, 1997.
- 2400 [56] *The CMS muon project: Technical Design Report*. Technical Design Report CMS,
2401 Geneva: CERN, 1997.
- 2402 [57] CMS Collaboration, “The cms physics technical design report, volume 1,”
2403 *CERN/LHCC*, vol. 2006-001, 2006.
- 2404 [58] M. Cacciari, G. P. Salam, and G. Soyez, “The anti- k_t jet clustering algorithm,”
2405 *Journal of High Energy Physics*, vol. 2008, no. 04, p. 063, 2008.
- 2406 [59] “Jet performance in pp collisions at 7 tev,” Tech. Rep. CMS-PAS-JME-10-003,
2407 CERN, Geneva, 2010.
- 2408 [60] X. Janssen, “Underlying event and jet reconstruction in cms,” Tech. Rep. CMS-CR-
2409 2011-012, CERN, Geneva, Jan 2011.
- 2410 [61] T. C. collaboration, “Determination of jet energy calibration and transverse mo-
2411 mentum resolution in cms,” *Journal of Instrumentation*, vol. 6, no. 11, p. P11002,
2412 2011.
- 2413 [62] R. Eusebi and on behalf of the CMS collaboration), “Jet energy corrections and
2414 uncertainties in cms: reducing their impact on physics measurements,” *Journal of
2415 Physics: Conference Series*, vol. 404, no. 1, p. 012014, 2012.
- 2416 [63] “Algorithms for b Jet identification in CMS,” Tech. Rep. CMS-PAS-BTV-09-001,
2417 CERN, 2009. Geneva, Jul 2009.
- 2418 [64] “Performance of b tagging at $\sqrt{s}=8$ tev in multijet, ttbar and boosted topology
2419 events,” no. CMS-PAS-BTV-13-001, 2013.
- 2420 [65] T. C. collaboration, “Identification of b-quark jets with the cms experiment,” *Journal
2421 of Instrumentation*, vol. 8, no. 04, p. P04013, 2013.
- 2422 [66] S. Dasu *et al.*, “CMS. The TriDAS project. Technical design report, vol. 1: The
2423 trigger systems,” 2000.
- 2424 [67] P. Sphicas, “CMS: The TriDAS project. Technical design report, Vol. 2: Data
2425 acquisition and high-level trigger,” 2002.
- 2426 [68] J. B. et al., “Calibration and Performance of the Jets and Energy Sums in the
2427 Level-1 Trigger ,” no. CMS IN 2013/006 (2013), 2013.

- [69] B. et al., “Study of Level-1 Trigger Jet Performance in High Pile-up Running Conditions,” no. CMS IN 2013/007 (2013), 2013.
- [70] J. J. Brooke, “Performance of the cms level-1 trigger,” Tech. Rep. CMS-CR-2012-322. CERN-CMS-CR-2012-322, CERN, Geneva, Nov 2012.
- [71] L. Randall and D. Tucker-Smith, “Dijet searches for supersymmetry at the large hadron collider,” *Phys. Rev. Lett.*, vol. 101, p. 221803, Nov 2008.
- [72] “SUSY searches with dijet events,” 2008.
- [73] “Search strategy for exclusive multi-jet events from supersymmetry at CMS,” Tech. Rep. CMS-PAS-SUS-09-001, CERN, 2009. Geneva, Jul 2009.
- [74] “Calorimeter Jet Quality Criteria for the First CMS Collision Data,” Tech. Rep. CMS-PAS-JME-09-008, CERN, 2010. Geneva, Apr 2010.
- [75] T. C. collaboration, “Performance of cms muon reconstruction in pp collision events at $\sqrt{s} = 7$ tev,” *Journal of Instrumentation*, vol. 7, no. 10, p. P10002, 2012.
- [76] “Search for supersymmetry in events with photons and missing energy,” Tech. Rep. CMS-PAS-SUS-12-018, CERN, Geneva, 2012.
- [77] M. Cacciari and G. P. Salam, “Pileup subtraction using jet areas,” *Phys.Lett.*, vol. B659, pp. 119–126, 2008.
- [78] Z. Bern, G. Diana, L. J. Dixon, F. Febres Cordero, S. Hoche, H. Ita, D. A. Kosower, D. Maitre, and K. J. Ozeren, “Driving missing data at next-to-leading order,” *Phys. Rev. D*, vol. 84, p. 114002, Dec 2011.
- [79] “Data-Driven Estimation of the Invisible Z Background to the SUSY MET Plus Jets Search,” Tech. Rep. CMS-PAS-SUS-08-002, CERN, 2009. Geneva, Jan 2009.
- [80] Z. Bern, G. Diana, L. Dixon, F. Febres Cordero, S. Hoche, *et al.*, “Driving Missing Data at Next-to-Leading Order,” *Phys.Rev.*, vol. D84, p. 114002, 2011.
- [81] W. Beenakker, R. Hopker, M. Spira, and P. Zerwas, “Squark and gluino production at hadron colliders,” *Nucl.Phys.*, vol. B492, pp. 51–103, 1997.
- [82] S. Abdullin, P. Azzi, F. Beaudette, P. Janot, A. Perrotta, and the CMS Collaboration, “The fast simulation of the cms detector at lhc,” *Journal of Physics: Conference Series*, vol. 331, no. 3, p. 032049, 2011.

- [83] S. Banerjee, M. D. Hildreth, and the CMS Collaboration, “Validation and tuning of the cms full simulation,” *Journal of Physics: Conference Series*, vol. 331, no. 3, p. 032015, 2011.
- [84] C. Collaboration, “Cms btag pog : Cms b-tagging performance database.” <https://twiki.cern.ch/twiki/bin/viewauth/CMS/BtagPOG>, 2013.
- [85] “CMS Luminosity Based on Pixel Cluster Counting - Summer 2012 Update,” Tech. Rep. CMS-PAS-LUM-12-001, CERN, Geneva, 2012.
- [86] R. Cousins, “Probability density functions for positive nuisance parameters.” <http://www.physics.ucla.edu/cousins/stats/cousinslognormalprior.pdf>, 2012.
- [87] L. Moneta, K. Cranmer, G. Schott, and W. Verkerke, “The RooStats project,” 2010.
- [88] F. James and M. Roos, “Minuit: A System for Function Minimization and Analysis of the Parameter Errors and Correlations,” *Comput.Phys.Commun.*, vol. 10, pp. 343–367, 1975.
- [89] A. L. Read, “Presentation of search results: the CL_s technique,” *Journal of Physics G: Nuclear and Particle Physics*, vol. 28, no. 10, p. 2693, 2002.
- [90] T. Junk, “Confidence level computation for combining searches with small statistics,” *Nuclear Instruments and Methods in Physics Research Section A: Accelerators, Spectrometers, Detectors and Associated Equipment*, vol. 434, no. 23, pp. 435 – 443, 1999.
- [91] A. L. Read, “Modified frequentist analysis of search results (the CL_s method),” no. CERN-OPEN-2000-205, 2000.
- [92] G. Cowan, K. Cranmer, E. Gross, and O. Vitells, “Asymptotic formulae for likelihood-based tests of new physics,” *The European Physical Journal C*, vol. 71, no. 2, pp. 1–19, 2011.
- [93] G. Cowan, K. Cranmer, E. Gross, and O. Vitells, “Asymptotic formulae for likelihood-based tests of new physics,” *European Physical Journal C*, vol. 71, p. 1554, Feb. 2011.